Controlling Liquid Atomization using Dilute Emulsions: Mitigation of Pesticide Spray Drift

Vom Fachbereich Maschinenbau
an der Technischen Universität Darmstadt
zur
Erlangung des Grades eines Doktor-Ingenieurs (Dr.-Ing.)
genehmigte

D i s s e r t a t i o n

vorgelegt von

Dipl.-Ing. Lars Niclas Opfer

aus Wiesbaden

Berichterstatter:	Prof. Dr.-Ing. C. Tropea
1. Mitberichterstatter:	PD Dr.-Ing. I.V. Roisman
2. Mitberichterstatter:	Prof. Dr.-Ing. G. Brenn
Tag der Einreichung:	30. April 2014
Tag der mündlichen Prüfung:	20. Juni 2014

Darmstadt 2014
D17 (Diss. Darmstadt)

Hiermit versichere ich, die vorliegende Doktorarbeit unter der Betreuung von Prof. Dr.-Ing. C. Tropea und PD Dr.-Ing. I.V. Roisman nur mit den angegebenen Hilfsmitteln selbständig angefertigt zu haben.

Darmstadt, 28. April 2014.

Abstract

Spray transport is mainly influenced by the velocity of the surrounding gas flow and by the distribution of drop sizes. In many applications, like spray painting, coating and crop protection, the exact location of spray deposition plays a very important role. In modern agriculture, misdirected pesticide spray is a major problem, which causes severe damages to surrounding ecosystems. This phenomenon is called spray drift. The susceptibility of a spray to drift is mainly influenced by its drop size distribution, since the trajectories of smaller drops can heavily be affected by the airflow. On the other hand, large drops have a negative effect on the coverage with pesticide. The present work aims towards controlling drop sizes during atomization with dilute emulsions.

Aerodynamic fragmentation of a single drop at relatively low Weber numbers, corresponding to the drop bag breakup, is employed as a model system to evaluate the ability of various adjuvants to control the atomization process. For this purpose, a compact, open-circuit wind-tunnel is designed. The process of aerodynamic fragmentation is then recorded by a high-speed video system. It is observed that drop breakup is heavily promoted even at very small quantities of emulsion. A theoretical model is presented which describes the film thickness evolution during the aerodynamic fragmentation process. It is shown that a polyethersiloxane emulsion can considerably increase the film thickness at the instant of rupture as well as the mean child drop sizes. Next, the breakup morphology of liquid sheets originating from agricultural flat fan nozzles is analyzed and discussed qualitatively and quantitatively using a high-speed video system and appropriate image processing algorithms. It is demonstrated that the polyethersiloxane drops cause the nucleation of a large number of holes in the liquid films. This effect leads to a much more regular breakup and reduces the length of the intact sheet. It is shown that the additives influence the breakup of a single drop and the atomization in agricultural sprays in the same manner.

Then, the effect of emulsion particles on final spray characteristics is

quantified by image based drop size measurements. Compared to pure water, the volume fraction contained in drift-prone drops can be reduced substantially by the addition of small amounts of polyethersiloxane. Additionally, the more regular breakup induced by the emulsion decreases the polydispersity of drop sizes and thereby improves the coverage characteristics of the spray.

Finally, it is shown that the addition of certain additives is very beneficial to the overall pesticide spray quality. The reduction of liquid contained in small and in large drops decreases the hazards caused by off-target pesticide deposition and improves the coverage characteristics. The crop protection process can thus be made more efficient and less precarious.

Kurzzusammenfassung

Der Transport von Sprays wird hauptsächlich durch die Bewegung des umgebenden Gases und die Verteilung von Tropfengrößen beeinflusst. In vielen Anwendungen, wie beispielsweise der Sprühlackierung, der Beschichtung von Oberflächen und dem Pflanzenschutz, spielt der zielgerichtete Auftrag des Sprays eine sehr wichtige Rolle. In der modernen Landwirtschaft rufen fehlgeleitete Pestizide schwere Schäden an umliegenden Ökosystemen hervor und stellen daher ein großes Problem dar. Dieses Phänomen wird als Spray Drift bezeichnet. Die Anfälligkeit eines Sprays für diesen Prozess wird hauptsächlich durch seine Tropfengrößenverteilung beeinflusst, da die Trajektorien kleinerer Tropfen stark durch den Wind bestimmt werden. Andererseits haben größere Tropfen eine negative Auswirkung auf die Bedeckungseigenschaften. Das Hauptziel der vorliegenden Arbeit ist die Kontrolle von Tropfengrößen während der Zerstäubung mit wässrigen Emulsionen.

Der aerodynamische Zerfall einzelner Tropfen bei kleinen Weber Zahlen wird auch als Taschenzerfall bezeichnet. Dieses Phänomen wird als Modellsystem verwendet um die Wirksamkeit verschiedener Additive zur Kontrolle des Zerstäubungsprozesses zu evaluieren. Hierfür wurde ein kompakter Windkanal entwickelt. Der Tropfenzerfall wurde mit Hilfe einer Hochgeschwindigkeitskamera aufgenommen. Es wurde beobachtet, dass der Zerfall selbst bei geringen Emulsionsmengen sehr viel früher auftritt als bei reinem Wasser. Ein theoretisches Modell für die Entwicklung der Filmdicke während des aerodynamischen Tropfenzerfalls wird präsentiert. Weiterhin wird gezeigt, dass eine Polyethersiloxan-Emulsion die Filmdicke im Moment des Aufbruchs und die typische Größe der entstehenden Fragmente deutlich erhöht. Daraufhin wird die Zerfallsmorphologie von flüssigen Schichten in landwirtschaftlichen Sprays qualitativ und quantitativ untersucht und diskutiert. Hierfür wird wieder eine Hochgeschwindigkeitskamera sowie geeignete Bildverabeitungsalgorithmen verwendet. Es wird demonstriert, dass das Polyethersiloxan die Nukleation einer großen Zahl von Löchern in den Filmen hervorruft. Dieser Effekt führt zu einem gleich-

mäßigeren Aufbruchsverhalten und reduziert die Länge des flüssigen Filmes deutlich. Es wird weiterhin gezeigt, dass der Einzeltropfenzerfall und die Zerstäubung in landwirtschaftlichen Sprays auf die gleiche Art und Weise beeinflusst wird.

Der durch die Emulsion hervorgerufene Effekt auf die Eigenschaften des entstehenden Sprays wird durch bildbasierte Tropfengrößenmessungen quantifiziert. Im Vergleich zu reinem Wasser kann der Anteil der driftanfälligen Tropfen durch die Zugabe von Polyethersiloxan deutlich reduziert werden. Zusätzlich wird die Polydispersität des Sprays durch den gleichmäßigeren Aufbruch verringert und die Benetzungseigenschaften des Sprays damit verbessert.

Schließlich wird gezeigt, dass sich die Zugabe bestimmter Additive sehr positiv auf die Gesamtqualität des Sprays auswirkt. Die Verminderung des Flüssigkeitsanteils in kleinen sowie in großen Tropfen verringert die Gefahren durch fehlgeleitete Pestizide und verbessert gleichzeitig die Benetzungseigenschaften. Die Ausbringung von Pflanzenschutzmitteln kann somit effektiver und weniger gefährdend für die Umgebung erfolgen.

Acknowledgements

First and foremost, I would like to thank my doctoral advisors PD Dr.-Ing. Ilia Roisman and Prof. Dr.-Ing. Cameron Tropea for their ongoing support and encouragement over the last years. I am truly thankful for having had the chance to conduct this study at the Institute of Fluid Mechanics and Aerodynamics of the TU Darmstadt. Working there has always been a great pleasure.

A special thank goes to Prof. Dr.-Ing. Günter Brenn from the TU Graz for co-refereeing this thesis. I appreciate the support from Evonik Industries AG, which made this investigation possible. Particularly, I would like to thank Dr. Joachim Venzmer and Dr. Michael Klostermann. Our regular meetings and fruitful discussions have essentially improved the outcome of this study.

I'm particularly grateful to my colleagues Andreas Güttler, Jochen Kriegseis and Andreas Reeh. They have become good friends and our periodic excursions to the Alps have been a great source of motivation. I would also like to express my gratitude to my co-worker and friend Christina Weickgenannt, as well as to Walter Schäfer and Hubert Marschall for their help and for always having an open ear for me.

The excellent atmosphere at the campus in Griesheim has provided a great working environment. I am thankful to Ulrike Cordes, Alexander Duchmann, Daniel Freudenhammer, Imdat Maden, Florian Wassermann, Michael Weismüller and Alexander Widmann for being or having been such great colleagues.

Sincere thanks go to Ilona Kaufhold, Martin Weiß and their workshop teams. The experimental investigations could not have been successfully performed without their support. Additionally, I am grateful to Stephanie Lath, Petra Fuhrmann and Birgit Neuthe for the administrative help. A substantial part of the laboratory work during this study has been conducted by Martin Smuda and Julian Donges, who did an excellent job. Thank you.

Contents

1 Introduction

1.1 Motivation

Today, the efficient production of foods is of particular importance since the worldwide population is rapidly growing, whereas the available area of arable land is limited. Additionally, the increasing production of biofuels is further limiting this area.

Modern agriculture is heavily dependent on pesticides and herbicides to maximize the crop yield. The development and use of highly effective and nonselective plant protection agents, such as glyphosate, requires a strict control of the affected area. This is of particular importance since even very small amounts of misdirected herbicide can cause severe damages to surrounding ecosystems. Furthermore, humans can also directly or indirectly be affected by the exposition to off-target pesticides.

Additionally, the deposition of pesticides in rivers and streams from which drinking water is withdrawn has to be avoided. In Germany, a strict limit of pesticides within the drinking water is provided by the drinking water ordinance. This limit is defined as 0.1 micrograms pesticide per liter water.

The well-directed application of pesticides is only possible under low-wind conditions and when proper dispersing systems are used. However, even under such conditions a certain amount of the dispersed liquid can easily be transported along with the wind before reaching the target. This phenomenon of drops being misdirected by the airflow is denoted as *spray drift*.

The sensitivity of a drop's trajectory to be influenced by the surrounding airflow is primarily dependent on its diameter. Large drops with high momentum follow a straight trajectory and reach the ground within a small horizontal distance from the nozzle. Once being ejected from the nozzle, small drops are rapidly decelerated by the drag force and follow the ambient airflow. The typical timescale of a drop to react to the velocity of the

ambient air is given by its relaxation time [1]

$$t_r^* = \frac{\rho_l D^2}{18\mu_a}, \tag{1.1}$$

where D is the drop diameter, ρ_l is the liquid density and μ_a is the viscosity of air. The characteristic relaxation time t_r^* increases proportionally to the square of the drop diameter. The susceptibility of a spray to drift is thus primarily affected by its drop size distribution.

Trajectories of drops after nozzle exit at half a meter above the ground, which is typical for agricultural applications, are depicted in Figure 1.1. The example demonstrates how the initial velocity of small drops rapidly decreases so that their motion is almost completely governed by the airflow.

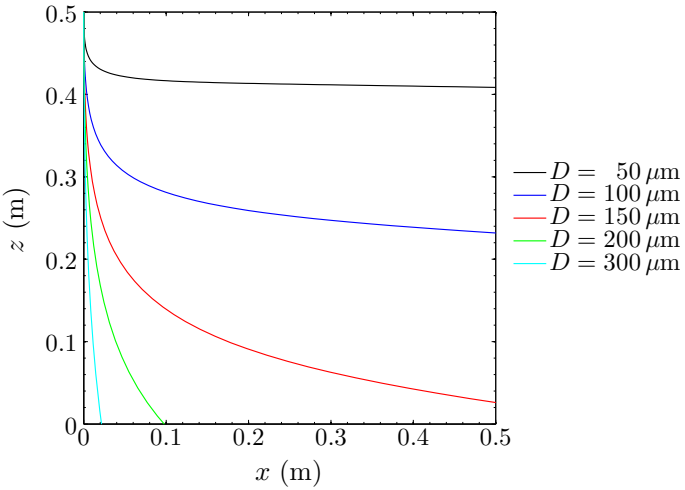

Figure 1.1: Typical drop trajectories after nozzle exit. The wind speed is 5 m/s in x-direction, the initial velocity of all drops is 25 m/s in negative z-direction. Drag forces are computed using the correlation $c_d = 24Re^{-1}(1+0.15Re^{0.687})+0.42(1+42500Re^{-1.16})^{-1}$ [2]. Evaporation is not considered.

However, a clear boundary between drift-prone and drift-resistant drops cannot be drawn. The real trajectories of drops are influenced by a variety

of parameters specific to the application site, such as spatial and temporal distribution of wind speeds, humidity and temperature. In the existing literature, the drift-prone content of a spray is therefore commonly defined as the liquid fraction being contained in drops smaller than 100 µm [3–5], whereas the corresponding ASTM Standard defines a boundary value of 105 µm [6].

1.2 Mitigation of spray drift

A variety of approaches for drift mitigation have been proposed due to the severe dangers and damages caused by off-target pesticide deposition. Wind shields and spray enclosures have been used to protect the pesticide spray from the airflow [7]. Electrostatic spray charging can be employed to control the trajectories of pesticide drops [8]. However, such methods require complex or expensive apparatus and haven't become accepted for field use. Presently, spray drift mitigation is almost exclusively achieved by operator controlled parameters and control of the spray characteristics.

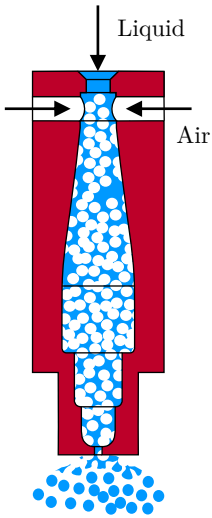

Figure 1.2: Air-induction nozzle

Crop protection agents are commonly dispersed by fan spray nozzles, which are also denoted as flat fan nozzles. Here, a thin liquid sheet is ejected from the nozzle, which breaks up in single fragments. Characteristics of the final spray can be controlled by altering the breakup morphology of the liquid film. For this purpose, two methods are generally employed. First, drop size distributions can be shifted towards larger drops by air-induction fan spray nozzles. Secondly, the size distributions can be influenced by the use of additives, which are added to the pesticide water mixture.

In air-induction nozzles, the liquid is accelerated before exiting the orifice. The liquid pressure is thereby decreased below the ambient pressure and air is sucked into the liquid flow through gas inlets. Liquid and gas

phases mix inside the nozzle and air bubbles are ejected with the expanding liquid sheet, which results in larger mean drop diameters. This shift in mean diameters is accompanied by a reduction of drift-prone drops. The mechanisms of this drop size modification are discussed in chapters 5 and 6 of this thesis. A sketch of such an air-induction fan spray nozzle is shown in Figure 1.2.

Air-induction nozzles reduce the amount of drift-prone liquid considerably by shifting the drop size distribution towards larger diameters. However, larger drops inherently lead to a reduced plant coverage quality, so that the pesticide efficiency can be considerably decreased. The two main requirements on agricultural spray characteristics, which are to be drift-resistant and to generate good coverage, are thus contradictory. Hence, desired drop size distributions are rather monodisperse and are concentrated around characteristic diameters of about 200 - 400 µm.

1.3 Aims & organization of the present thesis

The present study is focused on controlling agricultural spray characteristics by additive and has been conducted in close collaboration with Evonik Industries AG. It is known that dilute emulsions can be employed for such purposes, as reported in section 6.1. On the other hand, very little information about the emulsions' mechanisms of action in agricultural sprays can be found in the literature. Additionally, the influence of emulsion characteristics on breakup morphology and resulting drop size distributions of such sprays are not well understood.

Three major aims are addressed by this investigation:

1. A substance being effective in controlling spray characteristics is identified.

2. Light is shed on the mechanism of action of dilute emulsions when dispersed by agricultural nozzles.

3. The effect of the identified substance on final drop size distributions is revealed.

Besides these main topics, particular effort is made to reliably characterize agricultural sprays. It is further shown that the phase Doppler

technique, currently state-of-the-art for measuring drop sizes in agricultural sprays, can yield significantly biased results when its limitations are not carefully considered.

A novel approach for the evaluation of additive efficiency concerning drop size control is presented. The aerodynamic fragmentation of single drops at low Weber numbers is employed as a model system. Here, a liquid sheet is formed as a result of the drop deformation process. Characteristic length scales and time scales of this sheet are very similar to the ones observed at agricultural fan spray nozzles. The major advantage of this method is the complete prevention of contamination effects when several additives are sequentially tested.

The organization of this thesis is as follows. A description of the developed and employed measurement techniques and their fundamentals is given in chapter 2. Chapters 3 and 4 address the aerodynamic fragmentation of single drops at low Weber numbers, which is used to observe the effects of dilute emulsions and to evaluate their effectiveness. The findings and insights from this study are then applied to investigate the effect of dilute emulsions on agricultural sprays. Chapter 5 presents a description and discussion of the effect of additives on the breakup morphology of liquid sheets being produced by agricultural nozzles. The influence of the additives on the final outcome of the fragmentation process, the resulting drop size distributions is demonstrated and discussed in chapter 6. An overview of the existing literature and the current state-of-the-art is provided within each chapter.

2 Measurement techniques for spray characterization

A polydisperse distribution of drops or particles can be found in a variety of industrial applications and everyday phenomena. In most cases the particle size distribution plays an important role for the overall process and can strongly influence its quality and efficiency. This is particularly the case for fuel injection processes in internal combustion engines and gas turbines. Another example in which the process quality is strongly affected by the spray characteristics is the deposition of paint. In the case of agricultural sprays, the importance of controlling drop sizes has already been emphasized in chapter 1.

Considering the importance of drop or particle size distributions for the applications described above, as well as for many others, there is strong need for systems and techniques that are able to measure particle sizes and their distributions in a spray. Hence, a diversity of such systems were developed over the last decades.

These can generally be classified into two groups, particle counting techniques and integral methods. Counting techniques subsequently measure the diameters of single particles passing the detection volume. Measuring a large number of particles, typically several ten thousands, yields the drop size distribution and spray characteristics, such as mean diameters (see section 6.3). In the case of integral methods the detected signals are averaged over a specific amount of time. All particles passing the detection volume during that time contribute to the obtained signal. However, the contribution of a single particle to the averaged signal cannot be identified.

Presently, the most commonly used counting techniques are the phase-Doppler technique and the particle imaging method, which is also referred to as particle/droplet image analysis (PDIA). Prominent integral methods are the laser diffraction technique [9] and the combination of Laser induced fluorescence and Mie scattering [10]. A comparison between laser diffraction and the phase Doppler technique, that also sheds light on the measured quantities, is provided in [11].

The following sections provide a description of the drop size measurement techniques that have been employed and developed for the present study.

2.1 Image based drop sizing

The basic principle of image based drop sizing is rather straightforward. A photograph of a particular region in the spray is taken. The light source is usually placed on the optical axis that is defined by the line of sight of the camera so that the drops are illuminated from behind. This results in a bright image background, shadows of the drops appear as darker areas. Compared to a configuration where the reflected light is captured by the camera, background illumination results in a larger contrast between particles and background as well as rather sharp particle boundaries, at least when considering in-focus drops. The dimensions of particles captured by the camera can then be measured from the image.

Manual size measurements from analog images are quite laborious and are only feasible for a very limited number of particles. However, nowadays with the rapid evolution of digital cameras, digital image processing algorithms and computing power, the automatic processing of large numbers of images in an acceptable amount of time is possible.

In the present study, a digital image processing algorithm capable of automatically measuring particle sizes from images is developed and implemented. Fundamentals of image based techniques and a detailed description of the sizing algorithm is presented in the following sections.

2.1.1 Motion blur

One usually tries to freeze the motion of a flow when capturing a spray image. An exception would be the visualization of pathlines. This freezing can either be achieved by a sufficiently small exposure time of the camera or by a short illumination time, such as a flash light or a pulsed laser. The time during which light falls on the sensor will simply be referred to as exposure time Δt_e for the following discussion, regardless whether it is limited by the light source or the camera shutter.

In order to avoid motion blur in the image, the exposure time has to be smaller than a certain value $\Delta t_{e,max}$. This value can be estimated by defining that the maximum displacement of an imaged flow structure

during the time Δt_e should not exceed the size of K pixels on the camera sensor,

$$\Delta t_{e,max} = \frac{K\sqrt{A_{px}}}{MU}. \tag{2.1}$$

Here, A_{px} is the physical surface area of one pixel of the camera sensor, M is the magnification factor of the optical system and U is a typical velocity of the considered scattering centers.

2.1.2 Depth of field

Light rays emitted from one point in the focal plane of the lens are imaged onto one point of camera sensor, at least when lens aberrations and diffraction are neglected. However, rays emitted from a point outside the focal plane will not be imaged onto a single point of the sensor. Hence, a sharp image from objects that are not located in the focal plane cannot be expected, and the image of the object is blurred. If a certain amount of blur is accepted, the focal plane is extended to a focal volume with a certain depth along the optical axis. This depth is known as the depth of field (DOF).

The amount of accepted blur can be expressed as a length scale, which is the diameter of the circle of confusion c, as defined in Figure 2.1. Points inside the depth of field are imaged as disks with a diameter smaller than c, points outside the depth of field are imaged as larger disks. The acceptable diameter ϵ depends on the size of the sensor, the size of a single pixel and the magnification of the final image. For practical purposes ϵ is commonly defined as the diagonal length of the camera sensor divided by 1500.

The depth of field and its boundaries d_n and d_f can be obtained from geometrical optics [12] as

$$d_n = \frac{sf^2}{f^2 + N\epsilon(s-f)}, \tag{2.2}$$

$$d_f = \frac{sf^2}{f^2 - N\epsilon(s-f)}. \tag{2.3}$$

Here, N is the f-number and f is the focal length. Together with the magnification

$$M = \frac{f}{s-f}, \tag{2.4}$$

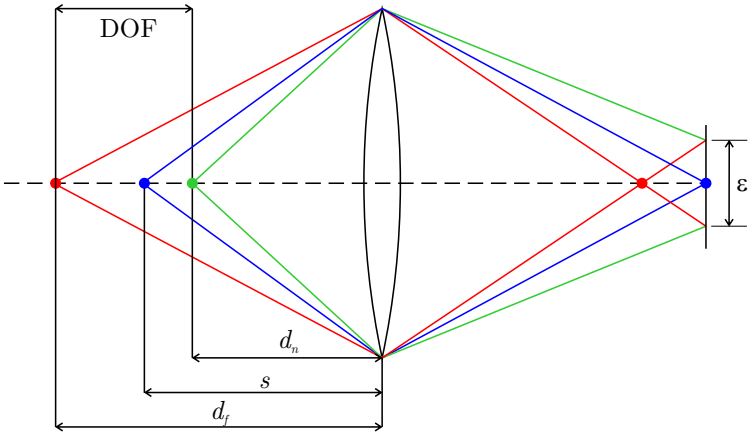

Figure 2.1: Ray paths for visualization of the depth of field (DOF). The closest point from the lens that yields a sharp image is defined by the distance d_n, the furthest point by d_f. The focal plane is located at the distance s from the lens. The value ϵ indicates the diameter of the largest acceptable circle of confusion.

the depth of field can be derived as

$$DOF = d_f - d_n = \frac{2f(M+1)/M}{(fM)/(N\epsilon) - (N\epsilon)/(fM)}. \tag{2.5}$$

The multiplication of numerator and denominator of equation (2.5) with $N\epsilon M/f$ gives

$$DOF = \frac{2N\epsilon(M+1)}{M^2 - (N\epsilon/f)^2}. \tag{2.6}$$

At rather small subject distances s and large magnifications M, the right hand term in the denominator of equation (2.6) can be neglected and a simple formula for the depth of field is obtained

$$DOF \approx 2N\epsilon\frac{M+1}{M^2}. \tag{2.7}$$

In this case, the depth of field depends only on the f-number of the lens, the diameter of the circle of confusion and the magnification. It becomes obvious that higher magnifications necessarily lead to a smaller depth of field. The depth of field can be increased by smaller apertures and hence larger f-Numbers N.

In many practical cases it is more convenient to determine the DOF of a given optical system empirically. This can be done by capturing an image of a line pattern under an angle of 45 degrees, as shown in Figure 2.2. The beginning of the line pattern is located at a distance d_n from the lens, so that it covers the complete depth of field. In the example shown here, it can be observed how the resolution of single lines is lost at about 10 mm, which indicates that the distance d_f from the lens is reached.

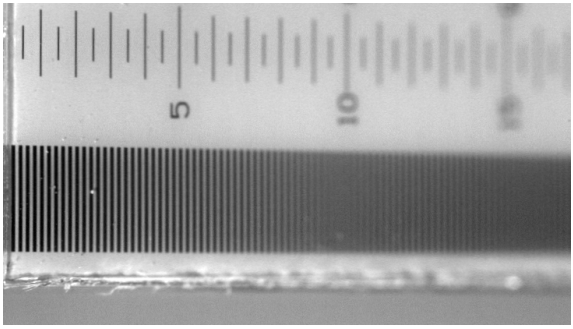

Figure 2.2: Line pairs used for the experimental estimation of depth of field.

The intensity profile along the line pattern shown in Figure 2.2 is presented in Figure 2.3. It can be observed how the amplitude of the intensity decreases since the black and white lines fade into one another with increasing distance from the focal plane. The depth of field can be found at the position where the amplitude of the intensity fluctuation can no longer be distinguished from the noise level.

2.1.3 Resolution limits

The resolving capacity of a simple objective lens is limited by aberrations, such as spherical aberration and chromatic aberration. While these shortcomings can be overcome by a more sophisticated lens design, the physical

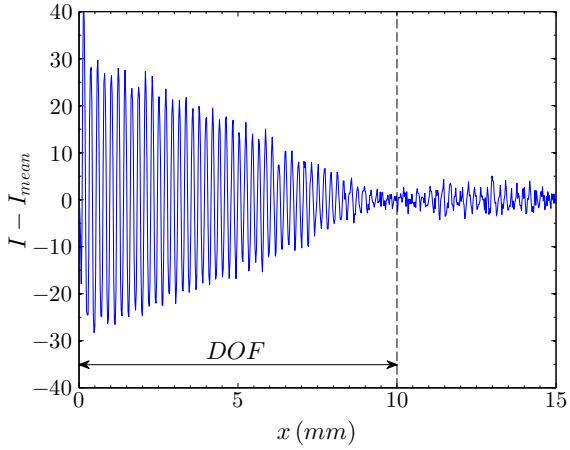

Figure 2.3: Intensity profile along the line pattern shown in Figure 2.2.

resolution limit for any objective lens is imposed by light diffraction at the lens aperture.

The resolution limit of a high-grade objective lens can be obtained by considering the Fraunhofer diffraction pattern of a circular aperture [12, 13], which can be described as

$$I(R) = I_0 \left(\frac{2J_1(kD/2 \sin\theta)}{kD/2 \sin\theta} \right)^2 . \tag{2.8}$$

Here, $I(R)$ is the light intensity with respect to the distance from the optical axis R. I_0 is the maximum light intensity, J_1 is the Bessel function of the first kind, k is the wavenumber and θ is the deviation angle from the optical axis. Figure 2.4 shows a plot of the intensity distribution of the Fraunhofer diffraction pattern as defined by equation (2.8).

The angle θ at which the first minimum of such a diffraction pattern can be found is

$$\sin\theta \approx 1.22 \frac{\lambda}{D}, \tag{2.9}$$

where λ is the wavelength of the incident light and D is the diameter of

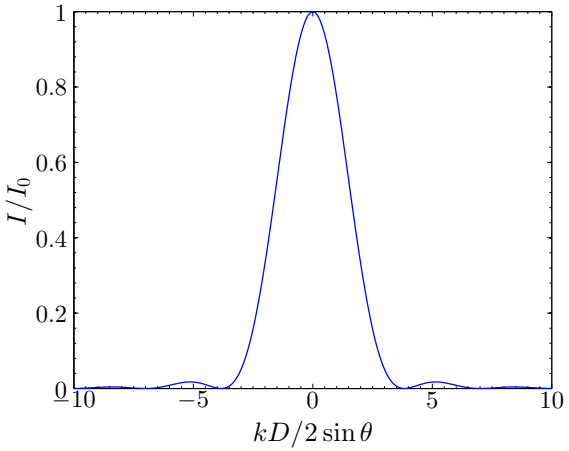

Figure 2.4: Fraunhofer diffraction pattern

the aperture. For small angles θ, equation (2.9) can be approximated by

$$\frac{R}{f} = 1.22\frac{\lambda}{D}. \tag{2.10}$$

with good accuracy. Rearranging equation (2.10) yields

$$R_{Airy} = 1.22\frac{\lambda f}{D}, \tag{2.11}$$

where R_{Airy} is the radius of the first intensity maximum of the Airy diffraction pattern. Two points can be resolved by the optical system only if the maxima of their images are separated by a distance larger than R_{Airy}, which is known as the Rayleigh criterion. Images with a distance smaller than the radius of first maximum of the Airy diffraction pattern appear as a single structure and can not be identified as two distinct features. The diffraction limit also implies that pixel sizes smaller than R_{Airy} no longer result in a better spatial resolution.

2.1.4 Image preparation

Before the actual particle detection and sizing procedure is executed the image is prepared to ensure that the intensity level of the background of the

complete image is uniform. This is usually done by subtracting a reference background image without particles present, recorded before or after the spray measurements. However, the intensity of the background changes from image to image due to fluctuations of the background illumination.

In order to avoid this problem, the background is first estimated from every image. This is done by applying a two dimensional median filter that covers a large, square neighbourhood (100×100 pixels) to the original image, as exemplarily shown in Figure 2.5(a). The median filter belongs to the group of nonlinear rank value filters [14]. It sorts the intensities of all pixels in its neighbourhood in ascending order. The center pixel of that neighbourhood is then replaced with the middle element of the sorted list. The result of a median filtering process is only very weakly influenced by outliers.

The outcome of this median filter is a low-pass filtered image, that is an estimate of the background intensity, Figure 2.5(b). The difference between the background image and the original image is then computed. This difference image has a much more uniform background than the original image and intensities are inverted, Figure 2.5(c). The drops now appear as bright spots on dark background, which simplifies further image processing.

The intensity distributions along a horizontal line of the images shown in figure 2.5 are depicted in Figure 2.6. Figure 2.6(a) shows the intensity distribution of the original image and the background estimation. The corresponding intensity distribution of the difference image is then presented in Figure 2.6(b).

2.1.5 Detection of individual particles

Two concepts of image segmentation are commonly employed for particle detection. The first method directly considers pixel intensities in the image. Since the drop surface exhibits strong curvature, incident light is either reflected or refracted and the drop appears as a dark contour on the bright background. The contrast between drop contour and background can then directly be used to identify and separate the individual drops by choosing an appropriate threshold level [15]. Alternatively, the boundary can be defined as the largest gray-level gradient between background and drop [16].

In the present study, the images are segmented by applying an intensity threshold to the difference images as shown in Figure 2.5(c). All pixels

(a) Raw image

(b) Background estimation. Contrast is enhanced for a better visualization of the intensity gradient

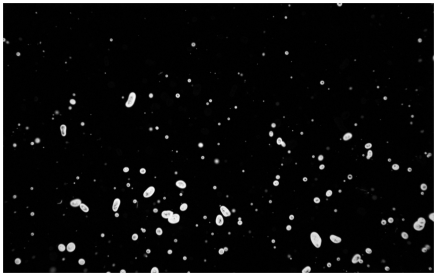

(c) Difference image used for further image processing

Figure 2.5: Typical example of the background estimation and subtraction process.

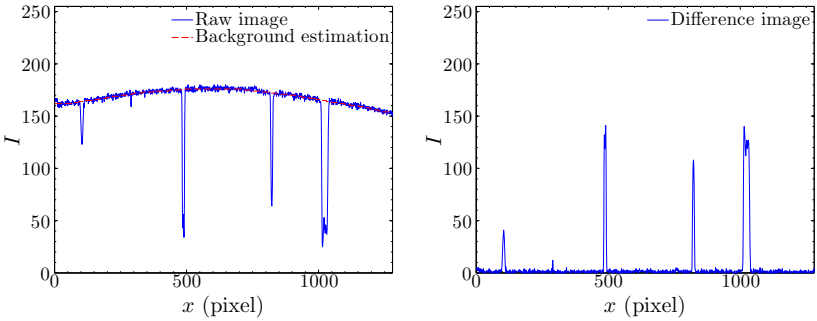

(a) Intensity profiles along the horizontal centerlines of Figures 2.5(a),(b)

(b) Intensity profile along the horizontal centerline of Figure 2.5(c)

Figure 2.6: Typical expample of the background estimation and substraction process.

below that threshold are set to zero, whereas pixels above the threshold are set to 1. This results in black and white images where drops appear as distinct, white areas with sharp boundaries. These regions of connected white pixels are then recognized by the image processing algorithm and their bounding boxes are computed. A bounding box is defined as the smallest rectangle encompassing a particle.

In the next step, the position of all bounding boxes are transferred to the gray-level difference image, so that particle positions are clearly known. A contour line around each particle is now computed. The intensity level of the contour is defined as $I_{contour} = c\, I_{max}$, where I_{max} is the maximum gray-level intensity of the considered particle and c is any value between 0 and 1. In the case of $c = 1/2$ this corresponds to the well-known *Full width at half maximum* method. The enclosed area of each contour A is then measured and the equivalent diameter D_e is computed as

$$D_e = \sqrt{\frac{4A}{\pi}}. \tag{2.12}$$

An exemplary visualization of the particle detection is shown in Figure 2.7.

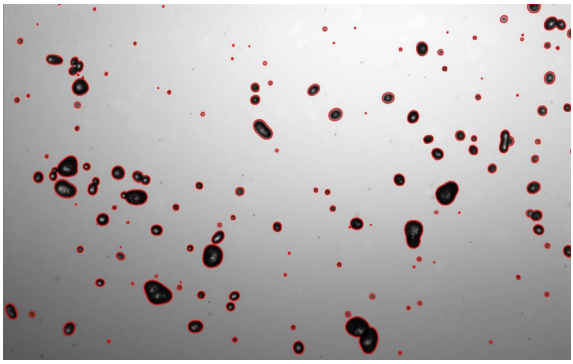

Figure 2.7: Visualization of the particle detection.

Out-of-focus particles

In most cases, the spatial dimensions of the overall spray are much larger than the depth of field of the optical system. Particles outside the depth of field are imaged as blurred spots on the camera sensor. This introduces complications for image based sizing algorithms:

Sizing uncertainty Since blurred particles don't exhibit a sharp boundary but a rather smooth transition from particle to background intensities, the equivalent diameter of such a blurred particle can no longer be measured easily.

Bias towards large particles When the width of the blurred region is comparable to the particle radius, the blur is not only noticeable at the particles edge but also in the central region. Hence, the contrast between background and particle, and thereby the signal-to-noise ratio, is reduced for smaller objects. This becomes apparent by considering the three smallest dots in Figure 2.8(b). At some distance from the focal plane, small particles can no longer be reliably distinguished from the background. Bigger particles however, can still clearly be recognized even if their edge is blurred. Effectively, this implies that the size of the detection volume is a function of the particle diameter. A very similar effect can be observed with the phase-Doppler technique.

Reduction of the overall image quality In dense sprays, out of focus particles are likely to overlap and form a diffuse layer on the background. In such cases, the typical signal-to-noise ratio is reduced and the reliable detection of particles in front of the diffuse layer is difficult.

The sizing uncertainty and the bias towards large particles are addressed by the image processing algorithm, as described in the following section. Reduction of the overall image quality is only a minor problem, since agricultural sprays are rather sparse.

Drop sizing errors

A photo-mask is employed for determining the relative contour level c and for estimating the sizing errors. The mask has been specifically designed and manufactured using laser lithography. Dots consist of a very thin chrome layer that is applied on glass. The diameters of these dots have an accuracy of 300 nm or better. A sample image of this calibration plate is shown in Figure 2.8(a).

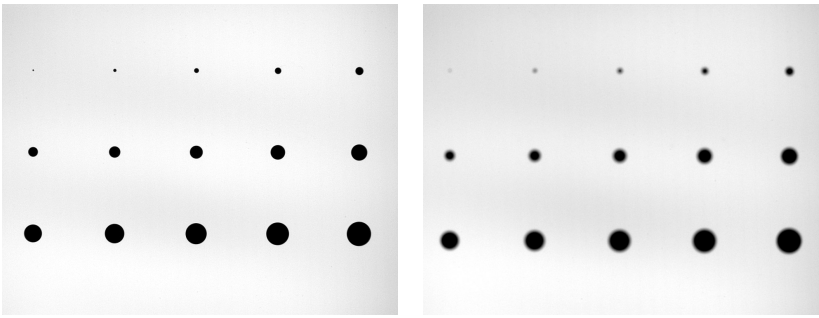

(a) (b)

Figure 2.8: Calibration plate with dots. The diameters range from 100 µm to 1500 µm. The left image shows the a focused image of the plate, in the right image the plate has been moved out of the focal plane.

The effect of the contour level on the accuracy of the sizing algorithm has been evaluated by traversing the calibration plate in z-direction which

is perpendicular to the focal plane. The dot sizes have then been measured for various contour levels c. Since the correct diameter of each dot is known, errors can easily be determined by comparing the measured diameters to the true ones. Figure 2.9 shows the outcome of this error evaluation.

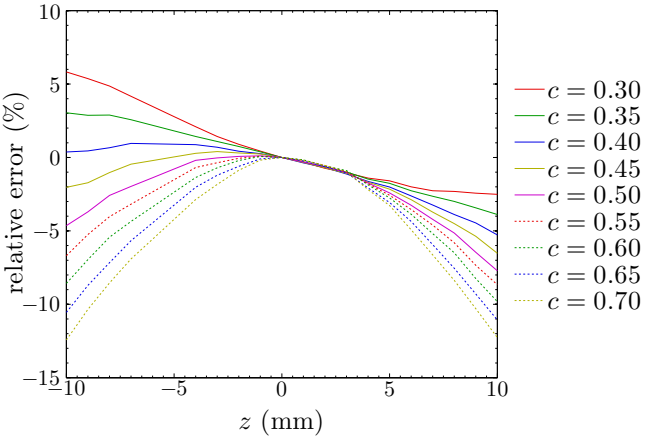

Figure 2.9: Influence of the contour level c on the sizing error at various distances from the focal plane. Results are presented for the $D = 1000$ µm point on the calibration plate.

The contour level $c = 0.35$ is now chosen in such a way that errors induced by out of focus particles are minimized. The error for various drop sizes is depicted in Figure 2.10. The systematic error for in-focus particles is shown in Figure 2.11.

Finally, the calibration plate is again used to address the bias towards larger particles. As explained above, this bias is induced by heavily blurred small particles that can no longer be reliably detected due to low signal-to-noise ratios. However, larger particles at the same distance from the focal plane can still be recognized by the algorithm.

The gray level gradients along the edges of the calibration plate edges are now considered and a correlation between drop diameter, distance to the focal plane and gray level gradient is obtained. During the analysis of spray images, this correlation is employed to estimate the distance from the focal plane of each detected drop. The measurement volume is now

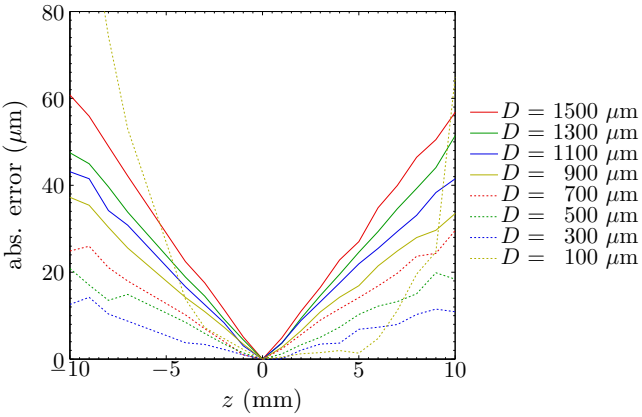

Figure 2.10: Influence of the drop diameter on the sizing error at various distances from the focal plane.

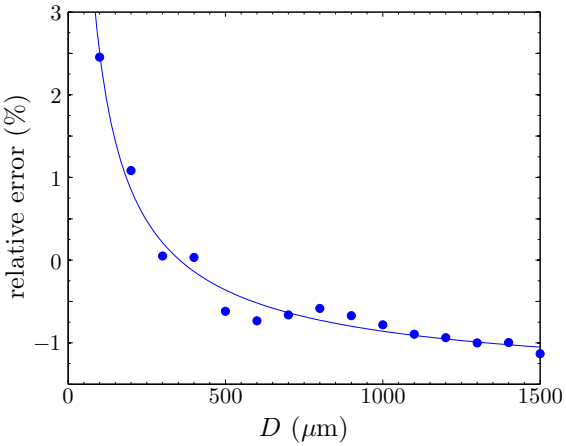

Figure 2.11: Influence of the drop diameter on the sizing uncertainty for in-focus drops.

restricted to positions where even the smallest drops can still be detected. For the optical setup used here, this corresponds to positions with $-6\,\mathrm{mm} < z < 6\,\mathrm{mm}$. Larger particles outside that volume are rejected and excluded from the final drop size distribution. The drawback of this method is that a certain amount of reliably detected particles is excluded from the statistics, which theoretically decreases the confidence level.

Overlapping particles

Overlapping particles are detected by considering their solidity values $\mathfrak{S}$. The solidity is defined as the ratio between the area of the particle and the area of a convex hull around the particle. Single drops usually exhibit a purely convex outline, whereas the outline of two overlapping drops has concave regions. This yields lower solidity values for overlapping drops, as exemplarily shown in Figure 2.12. A solidity threshold of $\mathfrak{S} = 0.93$ has been determined empirically. Particles with solidity values below that threshold are rejected from further processing.

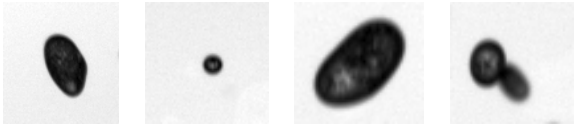

(a) $\mathfrak{S} = 0.98$ (b) $\mathfrak{S} = 0.98$ (c) $\mathfrak{S} = 0.97$ (d) $\mathfrak{S} = 0.88$

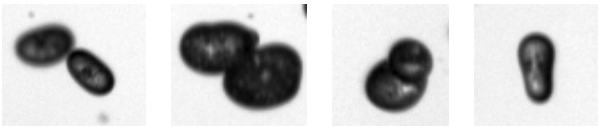

(e) $\mathfrak{S} = 0.83$ (f) $\mathfrak{S} = 0.87$ (g) $\mathfrak{S} = 0.96$ (h) $\mathfrak{S} = 0.96$

Figure 2.12: Solidity values $\mathfrak{S}$ of some exemplary drops.

It should be noted that this rejection algorithm works reliably for overlaps being small compared to the dimensions of the particles. This is the case in Figure 2.12(d)-(f). In Figure 2.12(g), the smaller particle in the foreground almost completely overlaps with the larger particle in the background. In this case, the algorithm is no longer able to automatically

detect the overlap. However, the area of the larger drop is only slightly overestimated in such a situation and the resulting sizing error is tolerable.

2.2 Laser Doppler & Phase Doppler Techniques

The following sections provide a short overview over the basic principles of the laser Doppler and phase Doppler techniques. A comprehensive description of these measurement techniques and the underlying physics is given in [17] and [18]. An even more detailed explanation of the interaction between light waves and particles can be found in [19].

2.2.1 Laser Doppler Technique

The Doppler effect describes the phenomenon of a frequency shift of waves when either the transmitter or receiver moves with a relative velocity. The frequency emitted by a stationary laser and observed by a moving particle is

$$f_p = f_l \left(1 - \frac{\vec{v}_p \cdot \vec{e}_{lp}}{c}\right), \tag{2.13}$$

where f_l is the frequency emitted by the laser, $\vec{v}_p$ is the particle velocity, $\vec{e}_{lp}$ is the unit vector from laser to particle and c is the speed of light. The frequency emitted by a moving particle and observed by a stationary receiver can be expressed as

$$f_r = \frac{f_p}{1 - (\vec{v}_p \cdot \vec{e}_{pr})/c}. \tag{2.14}$$

Here, f_p is the frequency as emitted by the particle and $\vec{e}_{pr}$ is the unit vector from particle to receiver. The index p refers to the particle, indices l and r denote laser and receiver, respectively.

When light is scattered from a moving particle or drop, the Doppler effect is invoked twice. The first frequency shift can be observed when incident light falls on the drop, which acts like a receiver in this case. When the light is emitted from the drop, its frequency is shifted again. In such a case, the frequency registered by a stationary receiver can be written as

$$f_r = f_l \frac{1 - (\vec{e}_l \cdot \vec{v}_p)/c}{1 - (\vec{e}_{pr} \cdot \vec{v}_p)/c}. \tag{2.15}$$

For $v \ll c$ this can be approximated by

$$f_r \approx f_l \left(1 + \frac{\vec{v}_p \cdot (\vec{e}_{pr} - \vec{e}_l)}{c}\right) = f_l + \frac{\vec{v}_p \cdot (\vec{e}_{pr} - \vec{e}_l)}{\lambda_l}. \tag{2.16}$$

The Doppler shift of the incident frequency is a linear function of the particle velocity, as described by the last term in equation (2.16). For typical applications in fluid mechanics, the Doppler shift is of the order of 10^7 Hz whereas the incident light has a frequencies around 10^{14} Hz. The ratio of incident frequency and Doppler shift is thus about 10^7, which makes the direct measurement of the Doppler frequencies almost impossible.

To overcome this problem, a dual beam configuration is commonly used to measure particle velocities. In this case, the measurement volume is formed by intersecting laser beams. Each of the laser beams is subject to the Doppler shift when scattered by a particle, as described in equation (2.16).

$$f_1 = f_l + \frac{\vec{v}_p \cdot (\vec{e}_{pr} - \vec{e}_{p1})}{\lambda_l}, \quad f_2 = f_l + \frac{\vec{v}_p \cdot (\vec{e}_{pr} - \vec{e}_{p2})}{\lambda_l}. \tag{2.17}$$

However, the obtained signal is now a result of optical mixing on the detector and can be written as the difference between the two frequencies f_1 and f_2:

$$f_D = f_2 - f_1 = \frac{\vec{v}_p \cdot (\vec{e}_1 - \vec{e}_2)}{\lambda_l} = 2\frac{\sin(\theta/2)}{\lambda_l} v_{p\perp}, \tag{2.18}$$

where θ is the intersection angle between the two laser beams. There are a two major benefits of equation (2.18) over equation (2.16). First of all, the beat frequency f_D is much lower than the frequency of the incident light f_l and can be resolved with sufficient accuracy so that the particle velocity $\vec{v}_p$ can directly be obtained from equation (2.18). Secondly, the detected frequency no longer depends on the detector position, which eliminates a source of error or inaccuracy.

2.2.2 Phase Doppler Technique

The Phase Doppler technique is a direct extension of the Laser Doppler technique which allows the simultaneous measurement of particle velocity and diameter. The optical setup of both techniques are almost identical and

a second photodetector is added to the system. Hence, the scattered light is recorded by two detectors, each of them generating a signal. The basic configuration of a phase Doppler system is shown in Figure 2.13. The two detectors are placed at a scattering angle ϕ for which one scattering order is dominant to avoid interference effects induced by multiple scattering orders.

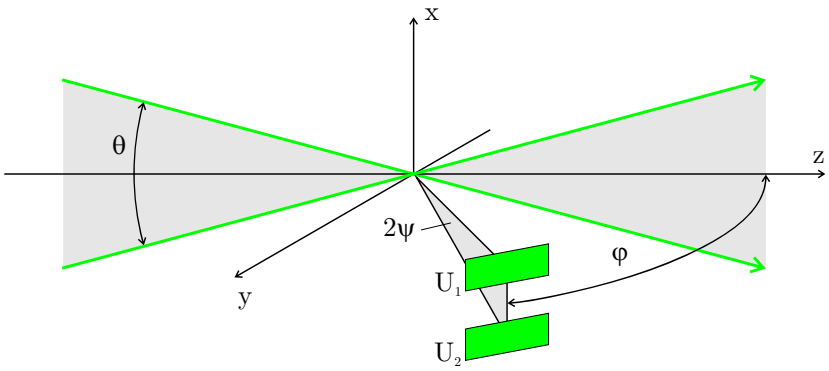

Figure 2.13: Principle configuration of the standard phase Doppler technique. Adapted from [18].

In the case of a homogeneous, spherical and transparent particle the phase difference between the two detectors $\Delta\Phi_{12}$ can be expressed as

$$\Delta\Phi_{12} = \frac{4\pi}{\lambda_0} D_p \left(\sqrt{1 + m^2 - m\sqrt{2}\sqrt{1 + A + B}} - \sqrt{1 + m^2 - m\sqrt{2}\sqrt{1 - A + B}} \right) \tag{2.19}$$

with

$$\begin{aligned} A &= \sin(\psi_r)\sin(\theta/2), \\ B &= \cos(\psi_r)\cos(\phi_r)\cos(\theta/2). \end{aligned} \tag{2.20}$$

Here, m is the ratio of refractive indexes, ϕ_r is the off-axis angle of the receivers, ψ_r are the elevation angles and θ is the beam intersection angle.

Equation (2.19) is valid for first order refraction, which is the most commonly used scattering order for phase Doppler measurements. It can be rearranged into

$$D_p = F_\Phi \Delta\Phi_{12}, \quad \text{with} \quad F_\Phi = f(\psi_r, \phi_r, \theta, m, \lambda_0), \tag{2.21}$$

where F_Φ is the phase conversion factor. Considering a particular given scattering order, the phase conversion factor depends only on the optical setup and the refractive indexes of medium and particle. For a given setup it can hence be calculated once and the particle diameters are obtained from multiplying the measured phase difference with the phase conversion factor. Furthermore, the phase Doppler technique is calibration free since no additional constants are present in equation (2.21).

The most severe drawback of the phase Doppler technique is its sensitivity to non-spherical particles. In [20] the response of a phase Doppler system to particles with various aspect ratios is studied and discussed. It is shown that rather small deviations from a spherical shape can lead to large sizing errors which can strongly reduce the the overall reliability of the measurement.

A possibility to validate the sphericity of particles is given when the phase Doppler technique is used in dual mode configuration [18]. Here, a second set of detectors is placed in the plane of the intersecting incident beams. These detectors have different scattering angles while their elevation angle is the same. This second optical configuration is known as a planar phase Doppler. When a standard and a planar configuration are used simultaneously (dual mode) the diameter of each particle can be measured on two orthogonal planes, the meridional and equatorial. The comparison of the two diameter measurements allows a validation of particle sphericity, as depicted in Figure 2.14. Particles with disagreeing diameters from the equatorial and meridional measurement are assumed to be non-spherical and are excluded from the measurement. A certain level of disagreement is tolerated to account for noise and slight particle deformations which do not lead to erroneous results.

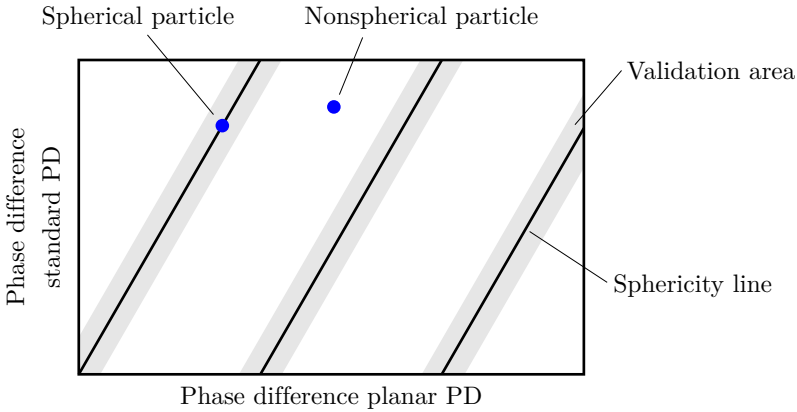

Figure 2.14: Sphericity detection of the dual mode phase Doppler configuration. Adapted from [18].

3 Aerodynamic fragmentation of pure liquids

3.1 Literature Review

The fragmentation of bulk liquid in small drops is of great importance for a wide range of applications, such as fuel injection in internal combustion engines and gas turbines, surface coatings and the application of pesticides in agriculture. The characteristics of the spray are crucial for the quality and efficiency of the overall process. For situations in which the relative velocity between the drops and the air is high, the outcome of aerodynamic drop breakup determines the size distribution of the atomized spray, e.g. in air-blast atomization.

For low viscosity liquids, the outcome of the liquid-gas interaction is determined mainly by the Weber number, which defines the ratio of aerodynamic forces and surface tension, $We = \rho_a D_0 U_a^2/\sigma$, where ρ_a is the gas density, D_0 is the initial drop diameter, U_a is the relative velocity between liquid drop and gas flow, and σ is the surface tension coefficient. The influence of viscosity on the liquid-gas interaction can be expressed by the Ohnesorge number $Oh = \mu_l/\sqrt{D_0 \rho_l \sigma}$, where μ_l and ρ_l are the dynamic viscosity and density of the liquid.

Early investigations of bag breakup that revealed the morphology of drops during the fragmentation process can be found in [21] and [22]. Depending on the Weber and the Ohnesorge numbers, different deformation and breakup modes have been identified in the literature [23, 24]: vibrational deformation (and breakup), bag breakup, multimode breakup and shear breakup. Recent comprehensive reviews on aerodynamic fragmentation of drops can be found in [25] and [26].

Among the fragmentation regimes described above, bag breakup occurs in a widest range of applications, since it occurs at relatively low Weber numbers. In [35] bag breakup is shown to be responsible for distinct peaks in the drop size distributions of high flow-rate industrial sprays. The drop

size distribution of rain close to the ground can also be related to the occurrence of bag breakup events during the free fall of drops [36]. The bag breakup process is not only observed during the fragmentation of drops, it is also responsible for the breakup of liquid jets injected into a crossflow [37]. The effect of Rayleigh-Taylor-instabilities on the breakup morphology is studied in [32].

Two experimental approaches for investigating such breakup processes have been used: drop breakup by a steady uniform air flow [27, 28] in a wind tunnel and by the propagation of a shock wave [29–31] in a shock tube. While shock tube experiments require more extensive apparatus, the use of such a device avoids the problem that the drop first has to pass through a boundary layer before it enters the homogeneous flow field.

The availability of digital high-speed cameras during the last decade revealed quantitative, time-resolved information about the breakup processes. In [33] Laser Induced Fluorescence is used to visualize not only the contour of the drop, but the structure of the liquid surface during the fragmentation. The authors conclude that pure shadowgraph visualizations might lead to misinterpretations concerning the physics of high We breakup events.

Flock et al. [34] successfully used Particle Image Velocimetry in order to measure velocity fields in the gas phase around the fragmenting drop in the bag and shear breakup regime. Their results also reveal quantitative information about the backflow in the wake of the drop.

It is interesting to note that the morphology of drop impact onto a deep pool surface is very similar to that of a bag breakup. However, in this case the liquid and gas phases are inverted and the expanding film consists of the gas entrained by the drop impact. This phenomenon is visualized and studied in [38].

The present study is focused on measuring and modeling the main morphological parameters of drops deformed by a continuous air flow in a wind tunnel. The aim is to estimate the film thickness in the bag prior to breakup. This thickness determines the outcome of the breakup, i.e. final drop size, but as yet has never been directly measured.

3.2 Experimental setup & methods

A horizontal, open-circuit wind tunnel has been designed and built for the experimental investigation of drop deformation and breakup due to aerodynamic forces. A sketch of this windtunnel is given in Fig. 3.1.

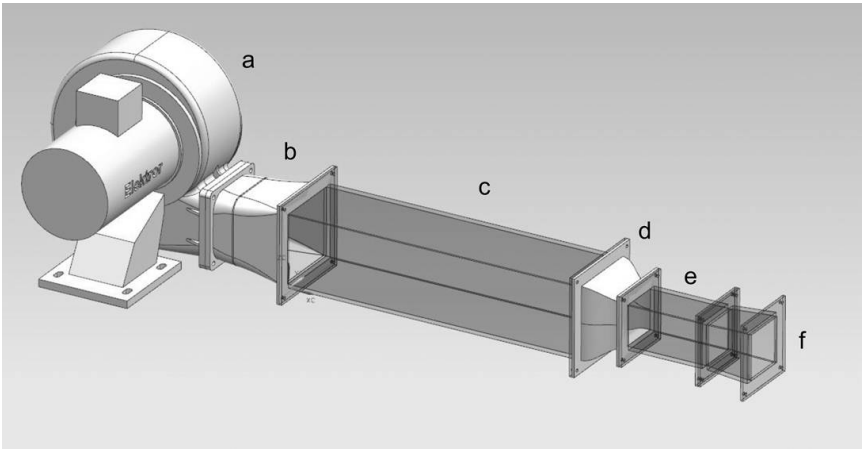

Figure 3.1: Windtunnel used for the experiments.

A radial blower (a) generates the pressure gradient necessary to accelerate the air. The blower is connected to the settling chamber (c) by an adapter (b), which transforms the cross-section of the blower to the square cross-section of the windtunnel. The cross-sectional area of the settling chamber is 150×150 mm^2. The air is led through a honeycomb structure and a cascade of wire meshes (not shown in Fig. 3.1) in order to homogenize and straighten the flow and to suppress vortices above a certain size. The airflow is then accelerated into the test section (e) by a nozzle (d). The cross-sectional dimensions of the test section are 80×80 mm^2. This gives a nozzle contraction ratio of 3.5. The air is then decelerated in a diffuser (f) to reduce the pressure loss at the outlet into the ambient air.

The settling chamber, test section and the diffusor are manufactured from transparent acrylic glass. This provides excellent optical access into the complete test section, so that no additional windows are necessary. The more complex geometries of the adapter and the nozzle are manufactured

in a rapid prototyping machine from polyamide.

An electronic frequency converter is employed to control the rotational velocity of the blower and thereby the air volume flux through the windtunnel. Air velocities can be adjusted continuously between 5 and 60 m/s. A Prandtl tube and a *Setra 239* differential pressure sensor are used to determine the air velocity by the well known relation $u_a = k_p\sqrt{2\Delta p/\rho_a}$. Here, k_p is the calibration factor of the Prandtl tube, u_a is the air velocity, Δp the pressure difference, ρ_a the air density. All experiments are conducted in turbulent airflow $Re >> 2300$ so that the air velocity outside the boundary layer can be assumed as constant. This assumption is verified by measuring velocity profiles in the central plane of the test section at various mean air velocities. Results of this measurement are depicted in Figure 3.2

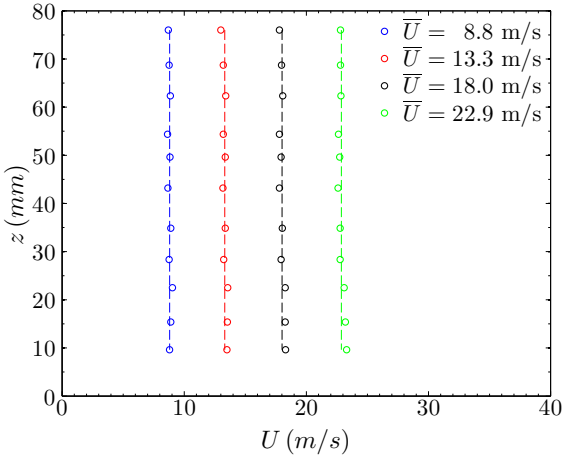

Figure 3.2: Velocity distributions in the test section of the windtunnel. Circles represent measurement values, dashed lines show respective mean velocity values.

A syringe is used to generate millimetric drops, which detach from the needle once gravitational forces overcome capillary forces. The drops are then accelerated by gravity and fall into the test section through a small opening in the top wall.

Liquid	density, ρ_l kg/m^3	viscosity, μ_l mPa s	surface tension, σ mN/m
water	1000	1.0	72.7
ethylene glycol	1110	16.1	48.3
isopropanol	785	2.1	21.2

Table 3.1: Properties of the liquids used in the experiments

3.3 Observations

The typical evolution of a single bag breakup event is shown in Fig. 3.3. Once the spherical drop is exposed to the airflow (Fig. 3.3a), it is deformed until it takes the shape of a disc, Fig. 3.3b-c. After that, the first occurrence of the liquid bag can be observed, Fig. 3.3d. The liquid bag then grows due to the elevated (stagnation) pressure inside, Fig. 3.3e-f. This growth continues until the liquid film suddenly bursts, Fig. 3.3g. The rupture of the liquid film initiates the expansion of holes and the generation of a high number of relatively small child drops, Fig. 3.3h-i. As soon as the thin film of the bag disintegrates completely, only a rim remains in the form of a torus, Fig. 3.3j. This rim itself is not stable and is fragmented as a result of the capillary instability, Fig. 3.3k.

In order to vary the parameters of the experiments three different liquids have been used: distilled water, ethylene glycol and isopropanol. This choice allows to identify the influence of viscosity and surface tension of the liquids on drop deformation and breakup.

The properties of the liquids used in this study are given in Table 3.1.

Some of the experimental conditions discussed in this study are listed in Table 3.2.

In our case, bag breakup is observed in the range $10 \lesssim We \lesssim 16$ which is consistent with the values reported in [27] and [39]. For all experiments, $Oh < 0.1$ so that the effect of viscosity can be neglected.

The parameters used for description of the liquid bag dynamics are illustrated in Figure 3.3(f). The temporal evolution of these parameters is evaluated employing a digital image processing algorithm that has been developed. First, the drop is segmented from the background, then its in-

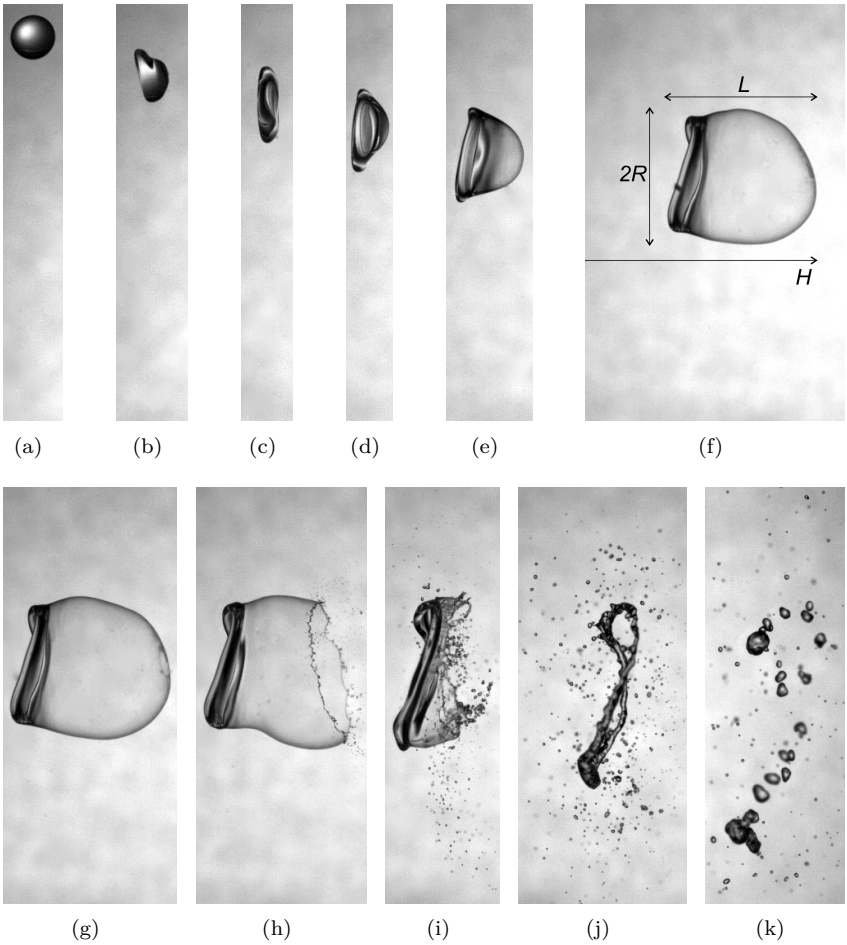

Figure 3.3: Typical evolution of a single bag breakup (water, We = 10.5, total duration: 14.3 ms). Airflow is from left to right. The images shown here correspond to times t [ms] = 0 (a), 3.5 (b), 6.1 (c), 7.3 (d), 8.6 (e), 9.7 (f), 9.9 (g), 10.1 (h), 11 (i), 12.1 (j) and 14.3 (k).

Exp.	Liquid	D_0, mm	U_a, m/s	We	Re
w-1	water	3.2	14.0	10.4	1552
w-2	water	3.3	15.0	12.1	1663
w-3	water	3.2	16.0	13.7	1720
i-1	isopropanol	2.4	8.5	9.8	297
i-2	isopropanol	2.4	9.5	12.3	332
i-3	isopropanol	2.3	10.5	14.4	352
e-1	ethylene glycol	2.7	13	11.3	80
e-2	ethylene glycol	2.7	14	13.1	86
e-3	ethylene glycol	2.7	15	15.1	92

Table 3.2: Exemplary list of the single drop experiments, showing the liquid, the initial drop diameter, D_0, air velocity, U_a, the Weber number, $We = \rho_a U_a^2 D_0/\sigma$, and the Reynolds number, $Re = \sqrt{\rho_l \rho_a} U_a D_0/\mu_l$

stantaneous position and dimensions are analyzed for each single frame of the high-speed visualization.

The dimensions of the rim as well as the film thickness of the bag are strongly changing with time. The final outcome of a single breakup event is thus dominated by the dynamics of the bag and the rim.

Each experiment is repeated ten times. Figure 3.4 shows the temporal evolution of the bag length for all runs, the median results are then taken for further data analysis and presentation.

Figures 3.5 - 3.7 depict the temporal evolution of the drop diameter, $2R$, bag length, L, and the tip position H for various liquids and air velocities. The length L first decreases until it reaches a minimum. In this initial stage, the drop is deformed by the airflow and the spherical shape of the undisturbed drop is transformed to the apparent disc shape.

The pressure difference between the front and the rear side of the drop causes the middle of the disc to bulge. The length of the drop increases again with the growing bag. The growth rate of the liquid bag increases with increasing the air velocity.

It is interesting that the drop diameter $2R$ increases first almost linearly up to the diameter of 5 - 6 mm. At this stage it corresponds to the rim diameter. At later stages the drop diameter corresponds to the bag diam-

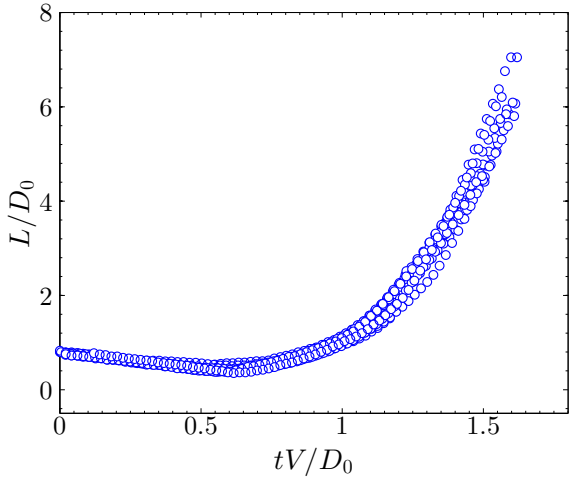

Figure 3.4: Evolution of the non-dimensional bag length L/D_0 for ten runs at $We \approx 15$

eter, which expands, also almost linearly, but with higher velocity. Similar behaviour of the drop diameter has been obtained in direct numerical simulations [40].

At later stages the bag evolution is dominated by the aerodynamic (stagnation) pressure, and surface tension only plays a minor role. The bag tip position H is decoupled from the motion of the rim and is determined only by the motion of the liquid film in the laboratory frame. However, the bag length L is additionally influenced by the rim dynamics.

3.4 Initial drop deformation

Consider first the initial drop deformation. At this stage, the geometry of the deforming drop is analogous to the drop impact onto a flat rigid substrate or to the case of axisymmetric binary drop collisions. Denote V as a velocity scale for the drop initial deformation. This velocity can be estimated using the pressure balance at the stagnation point. This pressure, however, cannot be estimated simply from the stationary Bernoulli

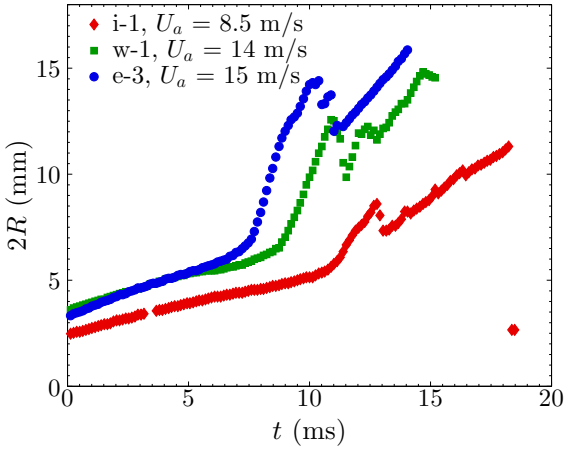

Figure 3.5: Evolution of the bag diameter $2R$, defined in Fig. 3.3f, for various liquids and air velocities. The experiments are defined in Table 3.2.

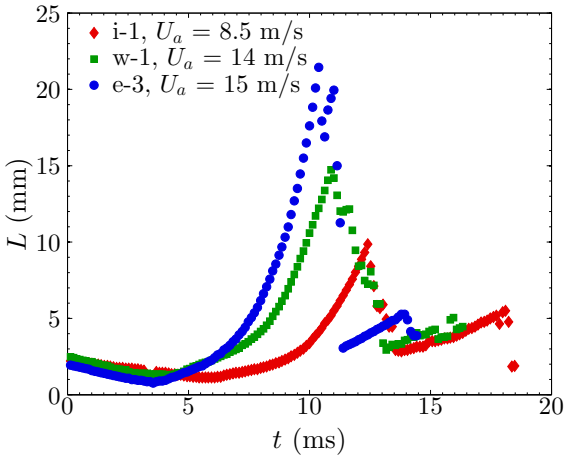

Figure 3.6: Evolution of the bag length L, defined in Fig. 3.3f, for various liquids and air velocities. The experiments are defined in Table 3.2.

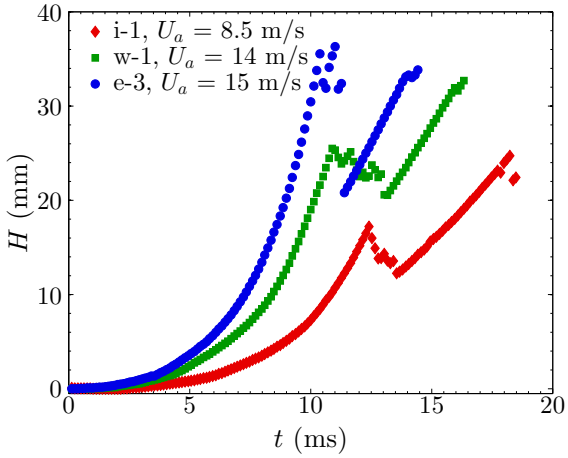

Figure 3.7: Evolution of the bag tip position H, defined in Fig. 3.3f, for various liquids and air velocities. The experiments are defined in Table 3.2.

equation, since the flow in the deforming drop is highly unsteady. In [41] the pressure has been obtained using numerical simulations of drop impact and binary drop collisions. The same result has been later obtained in [42]. It was shown, that the pressure scales well by $\rho_l V^2$, (here V is the impact velocity), but it is not constant. In fact, the pressure in the air and in the liquid regions can be estimated well from the potential flow over a thin disc of increasing diameter (which represents the frontal air-liquid impact interface) [43]

$$\frac{p}{\rho_l V^2} \approx \frac{1}{2} + \frac{1-2\bar{t}}{\pi\sqrt{\bar{t}-\bar{t}^2}}, \quad \bar{t} \equiv \frac{Vt}{D_0}, \quad \text{at} \quad \bar{t} < \frac{1}{2}, \tag{3.1}$$

which is at the initial stages of collision much larger than the capillary pressure in the drop for high Weber number impacts.

Since the air flow near the drop is analogous to the flow caused by drop deformation, the stagnation pressure in the air is scaled by $\rho_a(U_a - V)^2$. The deformation velocity can therefore be obtained from the pressure balance in the form $V = U_a\sqrt{\rho_a}/(\sqrt{\rho_l} + \sqrt{\rho_a})$. This relation yields $V = U_a/2$

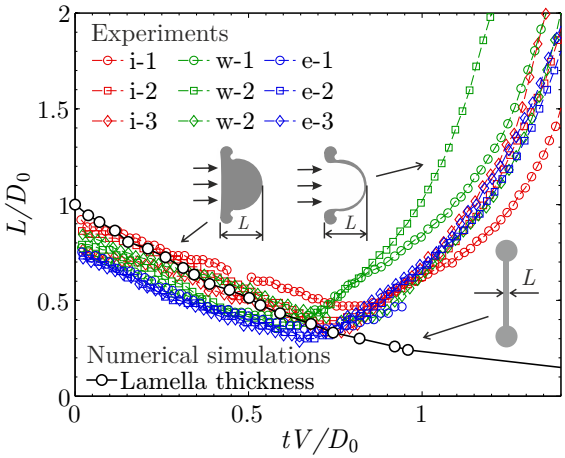

Figure 3.8: Evolution of the dimensionless drop thickness as a function of the dimensionless time for various liquids and air velocities, in comparison with the universal evolution of the lamella thickness produced by binary drop collision and drop impact on a rigid wall [45]. The experiments are defined in Table 3.2.

in the case of equal densities $\rho_a = \rho_l$. This case corresponds to the impact of a liquid drop into a deep pool of the same liquid [44].

Since the air density is much smaller than the liquid density, the expression for the deformation velocity can be simplified to

$$V \approx \frac{\sqrt{\rho_a}}{\sqrt{\rho_l}} U_a. \tag{3.2}$$

The hypothesis that the deformation velocity V defined in (3.2) can be used as a velocity scale at the initial stages of drop deformation by an air flow is confirmed in Figs. 3.8 and 3.9. In Fig. 3.8 the drop thickness L, scaled by the initial drop diameter measured for various experimental conditions is compared with the corresponding thickness of the lamella created by drop interaction with a rigid wall, and predicted by direct numerical simulations [45]. At early times of drop deformation ($tV/D_0 < 0.6$) the value of L represents the lamella thickness. It can be clearly seen in

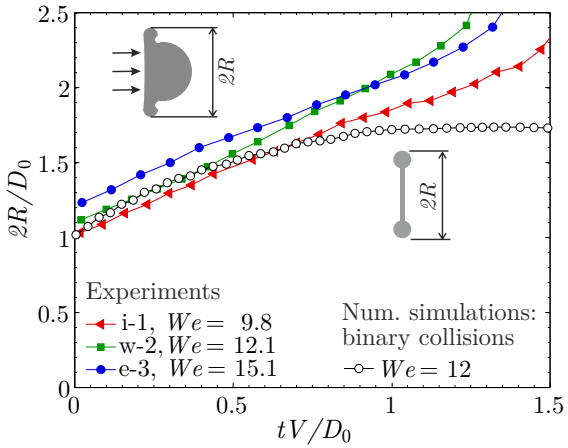

Figure 3.9: Evolution of the dimensionless drop diameter as a function of the dimensionless time for various liquids and air velocities, in comparison with the drop diameters by binary drop collisions obtained by the numerical model presented in [46]. The experiments are defined in Table 3.2.

Fig. 3.8, that at these early stages the measured lamella thickness for all the Weber numbers agrees well with the corresponding data for binary drop diameter. However, at larger times ($tV/D_0 > 0.6$) the value of L starts to increase since at this stage it describes the formation of the bag in which the lamella thickness is no longer directly accessible. This stage of bag formation is not scaled well using velocity V defined in equation (3.2), therefore the evolution of L at larger times depends significantly on the Weber number.

The dimensionless drop diameter $2R$ shown in Fig. 3.9 increases in time almost linearly for all experiments. These values are also compared with the diameter evolutions of drops after axisymmetric binary collisions [46] at similar values of the Weber number. The agreement at the early times is good, which again indicates the similarity between the phenomena of drop deformation by a fast air flow and drops binary collisions. At larger times the expansion rate of the drop diameter after a binary collision decelerates due to the capillary forces arising from the planar lamella. These forces

lead to the further rim merging. This phenomenon does not occur in the case of aerodynamic drop deformation, since the lamella at these times is deflected and the corresponding capillary force applied to the rim does not act in the radial, but in the axial direction, leading to the rim acceleration in the air flow direction.

It is clear that the phenomenon of initial drop deformation by aerodynamic pressure is similar to the corresponding phenomena of drop collision with the wall or binary collision of two drops. We can assume also that initially, before strong deflection and bag formation, the lamella thickness follows the analytical solution obtained in [47] for drop impact onto a rigid wall. For high Weber numbers and Reynolds numbers, the lamella thickness [45] at the axis is

$$\frac{h}{D_0} \approx \frac{\eta}{(\tau + \bar{t})^2}, \quad \eta = 0.39, \quad \tau = 0.25. \tag{3.3}$$

Equation (3.3) is developed for a planar, radially expanding flow, but is not valid for large times of bag expansion due to the strong film deflection, which causes an additional film stretching and thus the reduction of the film thickness.

3.5 Kinematics of the free liquid film flow

Let us describe now the motion of an axisymmetric liquid film in the Lagrangian form using the cylindrical coordinate system $\{r, z, \phi\}$. A motion of the material point in the axisymmetric case is determined by $r = X(\xi, t)$, $z = Z(\xi, t)$, where $\xi \equiv X(\xi, 0)$ is the initial radial coordinate of the point. The shape of the free thin liquid film is thus given in parametric form, ξ being the parameter. The evolution of the thickness $h(\xi, t)$ of the liquid film can be determined from the mass balance. In the cylindrical coordinate system the element of the liquid volume in an axisymmetric film can be expressed in the form $\mathrm{d}V(\xi) = X(\xi, t)h(\xi, t)\sqrt{\mathrm{d}X^2 + \mathrm{d}Z^2}$. The film thickness is then obtained from the mass balance as

$$h = \frac{\xi}{X} \frac{\sqrt{\mathrm{d}\xi^2 + \mathrm{d}Z_0^2}}{\sqrt{\mathrm{d}X^2 + \mathrm{d}Z^2}} h_0, \tag{3.4}$$

where $h_0(\xi)$ is the initial film thickness. Near the axis, at $r \to 0$, the expression (3.4) for h reduces to $h = h_0 / X_{,\xi}^2$.

If the gradient of the pressure applied to the film is negligibly small (which is true at large drop deformations) the component of the material acceleration in the tangential direction to the film vanishes, thus $X_{,tt}X_{,\xi} + Z_{,tt}Z_{,\xi} = 0$. If we denote $\lambda \equiv X_{,\xi}$ as the liquid film stretching in the radial directions, the evolution for λ can be obtained in the form $\lambda_{tt} = -\left(\lambda^{-1}Z_{,tt}Z_{,\xi}\right)_{\xi}$.

Now the film thickness near the axis ($X \to 0$, $Z_{\xi} \to 0$, $Z \to H$) can be described by the following system of equations

$$h = \frac{h_0}{\lambda^2}, \quad \lambda_{,tt} = \frac{\kappa}{2}\lambda\ddot{H}, \quad \text{at} \quad X \to 0, \tag{3.5}$$

where κ is the curvature of the film near the axis.

For a flat film, $\kappa = 0$, the solution of (3.5) yields the linear dependence of λ on t, leading to the expression for the lamella thickness in the form (3.3). The initial conditions for (3.5) can thus be directly obtained by matching the solution with the expression (3.3):

$$h_0 = \frac{D_0\eta}{\tau^2}, \quad \lambda = 1, \quad \lambda_t = \frac{V}{D_0\tau}, \quad \text{at} \quad t \to 0. \tag{3.6}$$

The evolution of the film thickness in the bag near the tip can then be obtained by numerical integration of (3.5), subject to the initial conditions (3.6), since the values of $H(t)$ and $\kappa(t)$ are known from the experiments. While the use of the parameters τ and η in (3.6) is not straightforward, it can be justified by the good agreement between drop-air and drop-wall interaction for early times as shown in Figs. 3.8 and 3.9.

Alternatively, the thickness of the liquid film can be estimated from the velocity of the expansion of the holes, which initiate the bag bursting (see Fig. 3.3(g)). The radius expands due to the motion of the hole rim, formed by capillary forces. The expansion velocity V_r of the hole rim is determined from subsequent image analysis of frames captured by the high-speed video system. The film thickness is then calculated using the well-known Taylor relation [48]

$$h = \frac{2\sigma}{\rho V_r^2}. \tag{3.7}$$

For all experiments, the results of the measurements of the bag film thickness, obtained using Eqs. (3.5) and (3.7), are shown in Fig. 3.10. The measurements performed using these two methods agree rather well. It

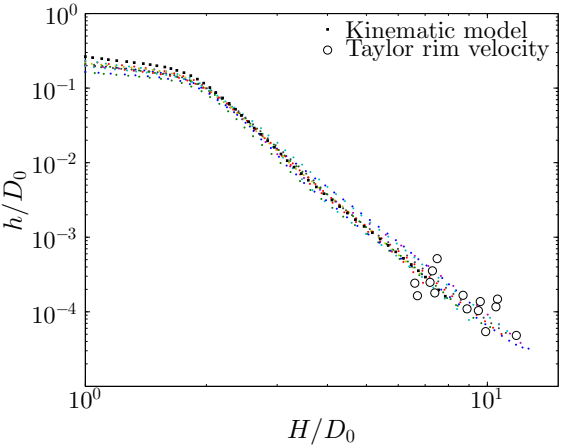

Figure 3.10: Evolution of the dimensionless film thickness h/D_0 as a function of H/D_0. Comparison of the measurements using Eqs. (3.5) and (3.7).

is interesting to note, that the evolution of the film thickness of bags on the dimensionless tip displacement H/D_0 is almost identical for various experimental conditions. This means that at large times the film thickness change is governed mainly by the bag geometry, and that the effect of the initial radial spreading is negligibly small. The location of the holes on the bag film is random. This can explain some scatter of the film thickness, estimated by (7), since this thickness is not uniform along the bag. Surprisingly, all of the results collapse onto one line. The best fit for the evolution of the film thickness in our experiments is

$$\frac{h}{D_0} \approx 2.5 \left(\frac{H}{D_0}\right)^{-4.62} \quad \text{at} \quad \frac{H}{D_0} > 2. \tag{3.8}$$

This correlation can be used for the estimation of the film thickness h_{burst} at the instant of the bag burst, since the tip displacement H at this instant can be determined from the images.

In Fig. 3.11 the obtained dependence of the dimensionless values of h_{burst} is shown as a function of the Weber number. While the evolutions of L, T and R in all the experiments are rather repeatable for the same

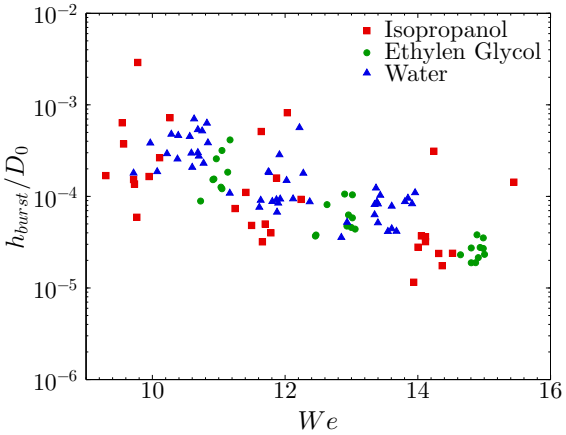

Figure 3.11: The burst thickness h_{burst}/D_0 of the bag as a function of the Weber number.

experimental conditions, there is an uncertainty of the instant of the burst and of the locations of the holes. This uncertainty explains the scatter in Fig. 6. However, a dependance of the average film thickness on the Weber number is indicated by the data. In the case of a millimetric drop, the average burst thickness h_{burst} near the tip ranges from about 1 µm at We = 10 to approximately 100 nm at We = 15.

It should be noted that both methods, the kinematics of the axisymmetric film deformation (3.5) and the velocity of the Taylor rim propagation (3.7), can be used for the measurement of free liquid sheets appearing in other applications. A well-known everyday example would be the film thickness evolution during the generation of soap bubbles.

4 Aerodynamic fragmentation of dilute emulsions

4.1 Literature Review

The aerodynamic fragmentation of Newtonian, low viscous liquids is of great importance for a wide range of applications and a large number of studies have addressed this topic over the last decades, see section 3.1. The effect of viscosity is often discussed in the form of a Weber-Ohnesorge map [23]. The observed regimes and breakup morphologies remain unchanged by viscous effects, while the regime transition Weber numbers increase for more viscous liquids. For $Oh < 0.1$, the effect of viscosity can completely be neglected. It is further reported that the influence of surface tension vanishes for $Oh > 2$ [49].

On the other hand, studies about aerodynamic fragmentation of complex liquids are very rare. It has been shown that the liquid sheet of viscoelastic drops in the bag breakup regime is much more stable than for Newtonian liquids [50]. The expansion of the liquid film at the instant of rupture is thus greatly increased. Thinner liquid sheets are generated during the film stretching process. After rupture, the film rebounds without disintegrating into a large number of single fragments.

Compared to water, the behaviour of coal water slurry drops is rather different when exposed to an air stream above the critical Weber number [51]. The initial drop deformation of water and coal slurry is similar, but in the case of coal slurry rupture of the liquid bag is induced very quickly after its formation. While drop size measurements were not within the focus of that study, it seems that fragments originating from coal slurry drops are much coarser than for water.

To the author's knowledge, almost no information about the aerodynamic fragmentation of emulsions can be found in the literature.

4.2 Mechanisms of induced liquid film rupture

The breakup of thin liquid films can be promoted by two methods. In the case of effervescent atomization air bubbles are injected into the liquid prior to leaving the orifice. Once the liquid is ejected from the orifice, the bubble pressure rapidly decreases to the ambient pressure and the air bubbles expand. When such an air bubble bursts, the liquid film is perturbed and eventually a hole can be generated. A comprehensive review of this technique can be found in [79]. The second possibility for inducing the rupture of liquid films is the use of specific emulsions. While the outcome of both methods is the nucleation of holes in the liquid film, the physical mechanisms are rather different. The following section provides a short overview about the mechanisms with which emulsion drops can act as hole nuclei in liquid sheets.

Let us consider an oil drop located completely inside a thin water film. The process of film rupture induced by such an oil drop can be divided into two steps [52]:

1. Entry of the oil drop into the water/air interface

2. Spreading of the oil drop on the water film

A condition for the oil drop to be able to enter the water/air interface is given by the entering coefficient E

$$E = \sigma_{w/a} + \sigma_{w/o} - \sigma_{o/a}, \tag{4.1}$$

where $\sigma_{w/a}$, $\sigma_{w/o}$ and $\sigma_{o/a}$ are the interfacial tensions between water and air, water and oil as well as oil and air, respectively. For negative entering coefficients $E < 0$ the water is able to completely wet the oil drop so that the drop is not able to penetrate the water/air interface permanently. Hence, the entering coefficient needs to be positive $E > 0$ for the drop to become surface-active.

The force balance at the triple phase point after the oil drop has entered the water/air interface is depicted in Figure 4.1. For the oil drop to be in equilibrium, the horizontal and vertical components of the three interfacial tensions need to be balanced [53], which is possible only if

$$\sigma_{w/a} - \sigma_{w/o} - \sigma_{o/a} < 0. \tag{4.2}$$

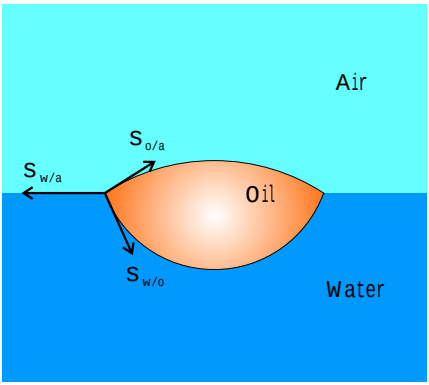

Figure 4.1: Force balance at the triple line between air, water and oil drop.

If equation (4.2) is not fulfilled, no equilibrium is possible and the drop completely spreads over the water film. Hence, the condition for spreading can be written as

$$S = \sigma_{w/a} - \sigma_{w/o} - \sigma_{o/a} > 0, \tag{4.3}$$

where S is the spreading parameter.

The spreading drop generates a fast radial flow at the water sheet surface, which is followed by the generation of a water jet in the outer direction, which can be explained simply by the continuity condition. This causes liquid from the opposite side of the film to flow towards the drop and the film is continuously thinned until it finally ruptures. The overall evolution of this process is sketched in Figure 4.2. Equation (4.3) implies that the sum of the interfacial tensions of the emulsion drops $\sigma_{w/0}$ and $\sigma_{o/a}$ have to be lower than the air/liquid interfacial tension of water to achieve an effective hole nucleation mechanism.

It should be mentioned that the discussed mechanism of hole nucleation in liquid films is widely accepted in the literature [52, 54, 55]. However, clear experimental evidence for the validity of the proposed mechanism of action has not yet been provided. Main problems in the experimental investigation of such processes are the small time scales (µs, ms) and length scales (nm, µm), as well as the three phases involved.

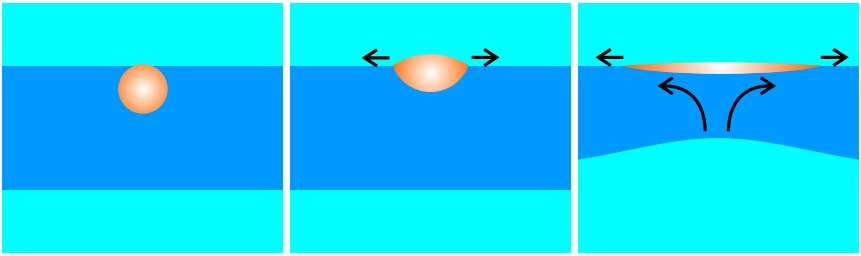

Figure 4.2: Mechanism of film thinning and hole nucleation. When an oil drop reaches the air-water interface, it spreads over the water film. This causes water under the spreading drop to be accelerated outwards. For reasons of continuity, liquid from the other side of the liquid film flows towards the oil drop. The water film is thinned until it finally ruptures.

4.3 Evaluation of additive effectivity

The phenomenon of bag breakup of pure liquids has been discussed in the previous chapter. This phenomenon is now employed as a model system for evaluating the effectivity of various additives to promote the breakup of liquid sheets. For each additive, various bag breakup events are recorded and evaluated as described in section 3.2. The effectivity of a particular additive is indicated by the non-dimensional drop length L_{burst}/D_0 and bag apex position H_{burst}/D_0 at the instant of bag bursting.

Since the liquid film is constantly thinned during the evolution of a bag breakup event, smaller values of H_{burst} and L_{burst} correspond to thicker liquid films at the instant of breakup. Additives resulting in small values of H_{burst} and L_{burst} are therefore deemed to be more effective than the additives producing rather large values of H_{burst} and L_{burst}.

This procedure has several advantages over the direct application of additives in agricultural nozzles.

- The effectivity test can be conducted with very small amounts of liquid, so that only some microliters of additive are needed.
- Except for the disposable syringes with which drops are generated, the liquid has no contact to any wall. While hoses and pumps have to

be cleaned thoroughly between applying different additives to prevent contamination of one liquid with the previous one, no system cleaning is needed in the case of bag breakup.

- Atomized liquid can easily be collected and is not delivered into the laboratory atmosphere. This would allow the evaluation of hazardous substances, although such liquids are not considered in this study.

Several dozens of additives have been tested in the course of this effectivity evaluation. The most promising results have been obtained by a self-emulsifying polyethersiloxane.

4.4 Properties of the polyethersiloxane emulsion

In the following sections and figures, the emulsion of polyethersiloxane in water is abbreviated by PES. Unless otherwise stated, the concentration of polyethersiloxane is 0.1% of the total liquid volume.

The addition of 0.1% polyethersiloxane to water has no noticeable influence on viscosity or density. However, the surface tension of the final emulsion is not the same as for water. The temporal evolution of the dynamic surface tension is measured by a *SITA science line t60* bubble pressure tensiometer. Results of this measurement are depicted in Figure 4.3(a).

It can be noted that the surface tension of interfaces older than about ten seconds is roughly half as large as for pure water. The timescale t^* relevant during the evolution of a single bag breakup event can be estimated by

$$t^* = \frac{D}{U}\sqrt{\frac{\rho_l}{\rho_a}}, \tag{4.4}$$

which corresponds to several milliseconds for the situations considered here. For such timescales, the dynamic surface tension of the polyethersiloxane emulsion is almost constant.

The particle size distribution of the emulsified polyethersiloxane drops in water is measured by a *Malvern* laser diffraction system. The volume density distribution is presented in Figure 4.3(b). The emulsion drop sizes are in the range of 1 µm and 100 µm with a volume median diameter of 9 µm.

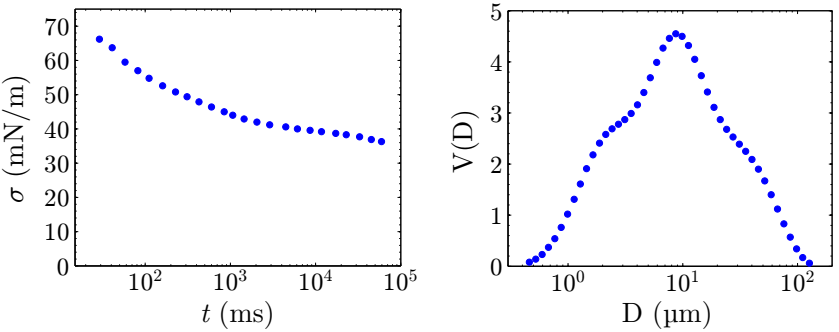

(a) Dynamic surface tension of a polyethersiloxane emulsion.

(b) Volume density distribution of emulsified polyethersiloxane drops in water

Figure 4.3: Dynamic surface tension and drop size distribution of the PES emulsion.

Microscopic images of the polyethersiloxane in water emulsion at two distinct magnifications are shown in Figure 4.4.

4.4.1 Weber numbers of polyethersiloxane emulsion drops

As shown in the previous chapter, the evolution and outcome of breakup phenomena of pure liquids is mainly determined by the Weber number. The Weber number can easily be defined when the surface tension is constant for a definite temperature. However, the situation with complex liquids, such as emulsions, is much more complicated. Here, the surface tension is a function of the surface age, so that the definition of the Weber number is no longer straightforward.

For all bag breakup experiments presented in this study, drops are generated by a syringe and detach once gravitation becomes dominant over capillary forces. While emulsion drops are pendant at the syringe, surface tension decreases with the age of the surface. Assuming a contact angle between liquid and syringe of 90°, the force balance at which the drop just detaches from the syringe can be expressed as

$$2\pi R\sigma = \frac{1}{6}\pi D^3 \rho_l g, \tag{4.5}$$

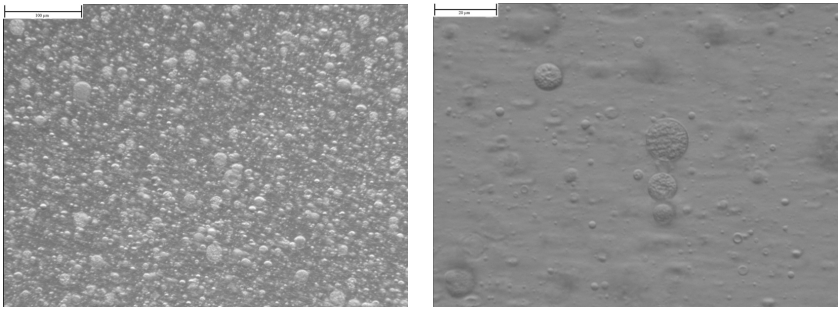

(a) Low magnification microscopic image of the PES Emulsion. The white bar in the upper left corner indicates 100 µm.

(b) High magnification microscopic image of the PES Emulsion. The white bar in the upper left corner indicates 20 µm.

Figure 4.4: Microscopic images of the polyethersiloxane emulsion

where R is the inner radius of the syringe and g is the constant of gravitation. The diameter D of the detached drop is known from the visualizations, so that the surface tension coefficient σ can theoretically by determined from equation (4.5). However, there are some problems with the direct implementation of this procedure which are described in [53], Chapter 2.

In the case of two different liquids dripping from syringes of equal diameters, equation (4.5) can be employed for both systems

$$2\pi R\sigma_1 = \frac{1}{6}\pi D_1^3 \rho_1 g, \tag{4.6}$$

$$2\pi R\sigma_2 = \frac{1}{6}\pi D_2^3 \rho_2 g. \tag{4.7}$$

Equation (4.6) is now divided by (4.7), which yields

$$\sigma_2 = \frac{D_2^3 \rho_2}{D_1^3 \rho_1}\, \sigma_1. \tag{4.8}$$

Equation (4.8) can now be used for a rough estimation of surface tension σ_2 when σ_1 is known. It has to be noted that equation (4.8) does not account for differences in the wetting characteristics of the two liquids.

The applicability of this procedure can be demonstrated by consideration of the initial drop sizes for different fluids used in our experiments, as presented in table 3.2. For ethylene glycol, (4.8) predicts $\sigma = 44$ mN/m, while the true surface tension coefficient is $\sigma = 48.3$ mN/m. This method can therefore be considered as an acceptable engineering approximation for the effective surface tension with a tolerance of 10%. It is a rather promising method, based on an accurate control of other parameters of the experiment, including drop generation process and velocity profile in the wind tunnel.

For a polyethersiloxane emulsion dripping from a syringe, the observed drop size is $2.6\,\text{mm} < D < 2.7\,\text{mm}$. The surface tension estimation using equation (4.8) yields a value of $\sigma \approx 45$ mN/m. This value corresponds to the dynamic surface tension measured by the bubble pressure method for $t = 10^3$ s, as presented in Figure 4.3(a), which matches the drop formation time at the syringe. The agreement between these two methods indicates that the surface tension of the detached drops is reliable.

However, in the context of aerodynamic fragmentation the direct application of surface tension coefficients obtained for detached drops to the determination of Weber numbers still poses some problems. After being exposed to a sufficiently fast airflow, the drops are initially deformed to the shape of a disk, as demonstrated in Figure 3.3a-c. The surface area of drops is increased during this phase. Hence, the concentration of surface-active molecules at the surface decreases which implies that surface tension becomes larger during the onset of fragmentation.

To overcome this problem, a pragmatic estimation of the surface tension coefficient σ has been used for the description of aerodynamic fragmentation of PES emulsion drops. In the course of the experimental investigation of bag breakup of pure liquids, it has been observed that the critical Weber number is always $We_{crit} \approx 10$. For PES emulsions, the air velocity in the test section of the wind-tunnel has been increased with drops present in the flow until the onset of fragmentation was observed. For drop sizes of $D = 2.6$ mm, the critical velocity was determined to be $U_{crit} = 14$ m/s. Assuming that the onset of fragmentation takes place at $We_{crit} = 10$, the effective surface tension of the emulsion can now be obtained from

$$\sigma_{eff} = \frac{\varrho_a \, D \, U_{crit}^2}{We_{crit}} \approx 62\,\text{mN/m}. \tag{4.9}$$

This value is considerably larger than the surface tension of the detached

drop, which confirms that surface tension is increased due to aerodynamic deformation and the resulting rapid enlargement of the surface area, leading to a reduction of the surfactant concentration at the drop surface.

4.5 Observations

The experimental setup used for the visualization and investigation of bag breakup of emulsion drops is identical to the one used for pure liquids and has been described in section 3.2. Images have been recorded with a spatial resolution of 1024×768 pixel @ 48 µm/pixel. A typical example for the evolution of a single bag breakup event with PES emulsion is shown in Figure 4.5, a bag breakup of pure water the same Weber number is presented in Figure 4.6. The images shown here are recorded with a temporal resolution of 7900 frames per second.

The initially spherical PES emulsion drop is first deformed and flattened by the airflow, Figure 4.5a-c. At some instant, the center part of the drop is accelerated faster than its periphery and an expanding liquid film is formed, Figure 4.5d-e. Until now, no impact of the additive can be observed and the breakup morphology can not be distinguished from water.

However, holes appear in the liquid film much earlier than it is the case for pure water. It is also interesting to note that typically several independent holes are generated in a very short period of time, Figure 4.5f-g. The retraction of the liquid film leaves a number of rather thick ligaments, which are then subject to capillary instabilities, Figure 4.5h-k. After the bag has disintegrated, the remaining rim is no longer stable and is fragmented due to capillary instabilities, too.

The comparison of Figures 3.3 and 4.5 reveals that the polyethersiloxane emulsion does not only have a significant influence on the breakup morphology but that the drop size distribution originating from bag fragmentation is also heavily influenced. A larger number of large drops is produced, whereas the overall number of child drops decreases considerably. This effect can be related to the fact that the liquid emulsion film at the instant of rupture is much thicker than it is the case for water.

A second set of drop breakup visualizations with higher magnification and higher temporal resolution of 12000 frames per second has been performed in order to obtain deeper insight into the hole nucleation mechanism. A typical example from these visualizations is shown in Figure 4.7.

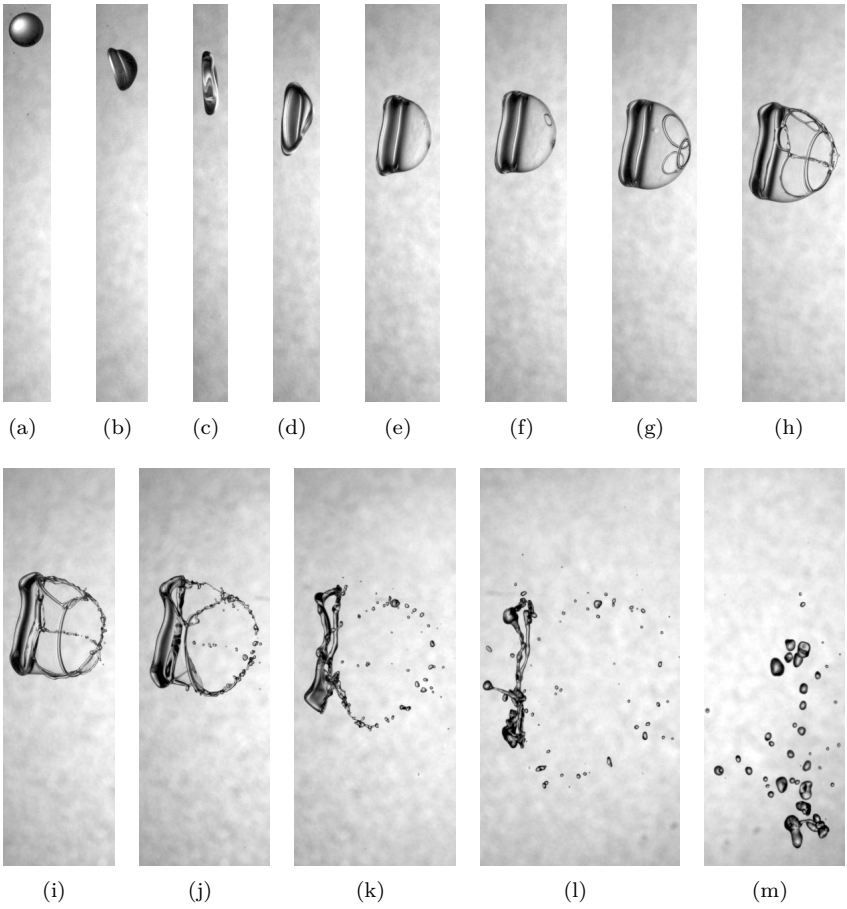

Figure 4.5: Typical evolution of a single bag breakup (PES, We $\approx$ 12). Airflow is from left to right. The images shown here correspond to times t (ms) = 0 (a), 3.9 (b), 7.2 (c), 9.6 (d), 11.0 (e), 11.2 (f), 11.6 (g), 12.2 (h), 12.5 (i), 13.0 (j), 13.9 (k), 15.7 (l) and 19.4 (m).

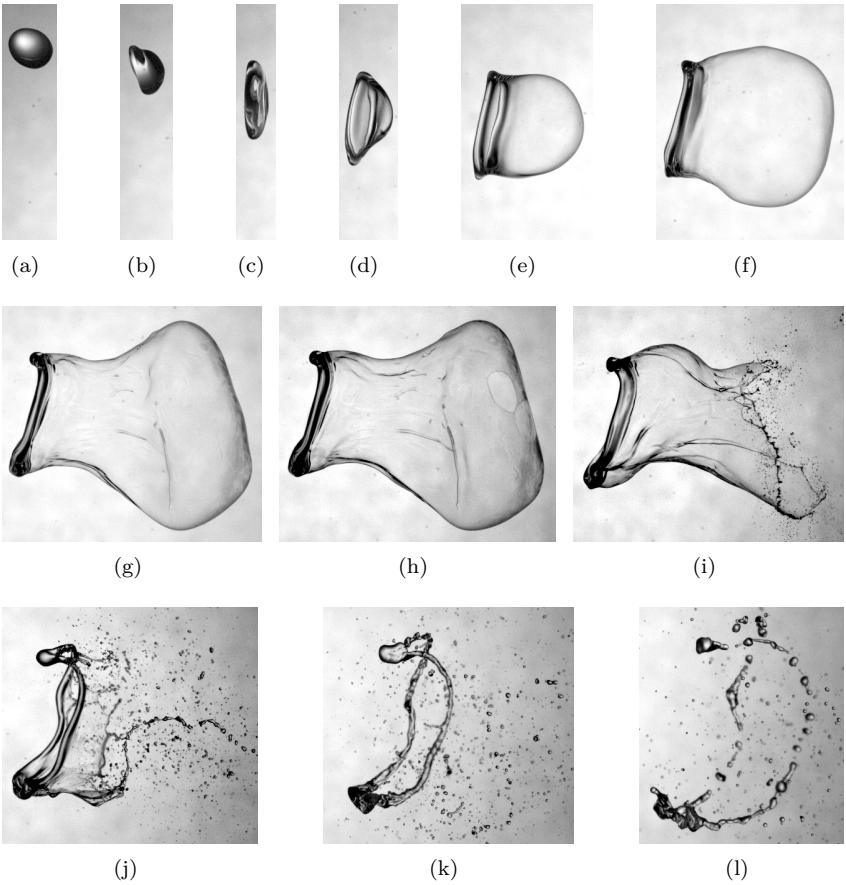

Figure 4.6: Typical evolution of a single bag breakup (Water, We $\approx$ 12). Airflow is from left to right. The images shown here correspond to times t (ms) = 0 (a), 3.3 (b), 7.3 (c), 9.6 (d), 11.1 (e), 12.2 (f), 13.0 (g), 13.2 (h), 13.7 (i), 15.0 (j), 16.0 (k) and 17.6 (l).

The initially smooth surface of the bag is perturbed by circular deformations originating from spreading oil drops, Figure 4.7a-c. While the surface perturbations can be clearly recognized from the images, single oil drops can still not be identified at such magnifications. However, this indicates that the area affected by a spreading emulsion drop is much larger than its initial diameter.

Shortly after surface perturbations become visible, the first holes in the liquid film of the bag can be observed, Figure 4.7c. In less than 200 microseconds, the bag is almost completely punctured, Figure 4.7d-f. The more or less simultaneous occurrence of several holes in the bag implies that there is a critical film thickness above which the emulsion drops are without effect.

It can be observed that most surface perturbations lead to hole nucleation and film rupture, while some of them are damped and no hole is generated. One example of such a damped surface deformation can be seen at the center of the bag (Figure 4.7e,f).

4.6 Drop length and apex position at the instant of rupture

The addition of 0.1% polyethersiloxane to water has no significant influence on density or viscosity. Hence, the temporal evolution of the bag apex position H for water and PES emulsion can be expected to be very similar when Weber numbers are kept constant. This assumption is confirmed in Figure 4.8, where the evolution of H/D_0 is presented for both liquids. The time dependent progressions of the curves are almost identical up to the moment of bag rupture, which happens rather early for the PES emulsion when compared to pure water.

The effect of the polyethersiloxane emulsion on aerodynamic breakup has been analyzed quantitatively by considering the length L_{burst} and the bag apex position H_{burst} at the instant of film rupture. Each experiment is repeated ten times; mean values and standard deviations are reported and discussed in the following section.

Figure 4.9 shows the influence of PES for various Weber numbers. The standard deviation is indicated by half of the bar height. Obviously, L_{burst} and H_{burst} are strongly decreased by the emulsion, which is in good agree-

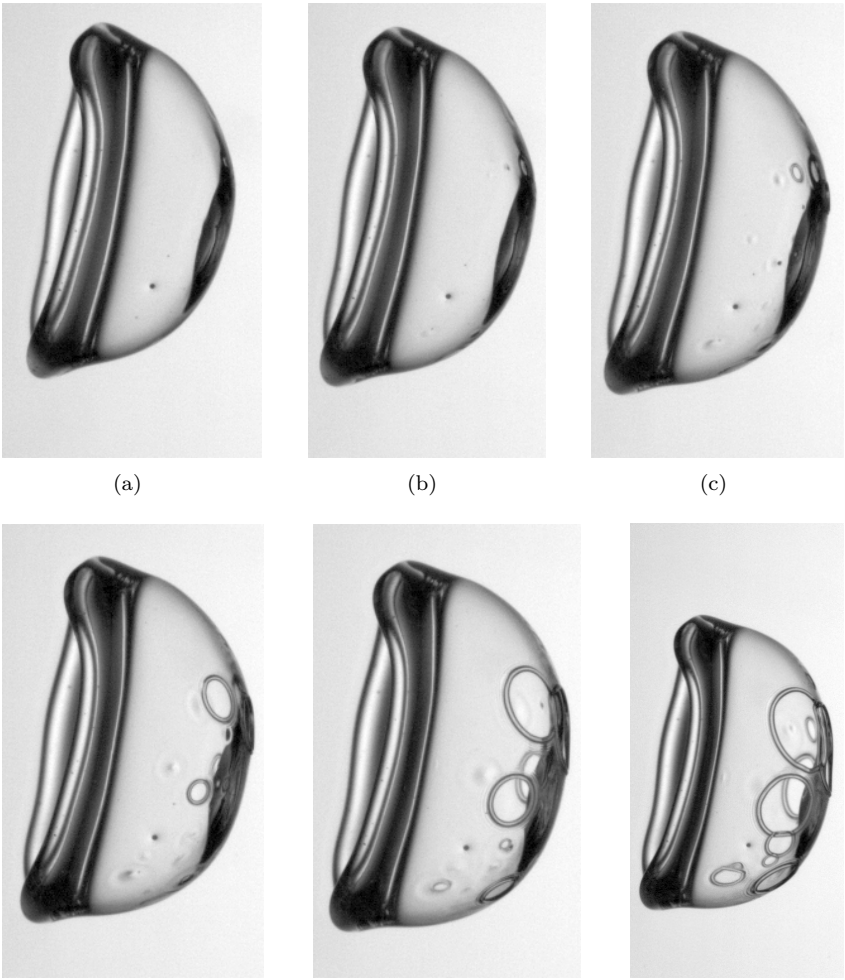

(a) (b) (c)

(d) (e) (f)

Figure 4.7: Hole evolution at times t (µs) = 0 (a), 91 (b), 182 (c), 273 (d), 364 (e) and 455 (f). The width of the images corresponds to approximately 4 mm.

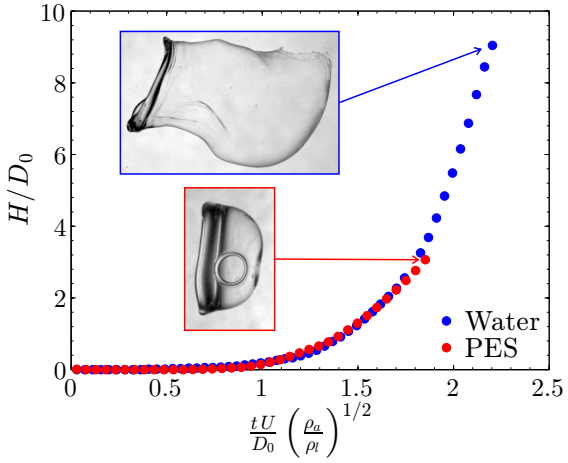

Figure 4.8: Temporal evolution of the bag apex position H/D_0 for pure water and PES emulsion at $We \approx 12$.

ment with the observations reported in section 4.5. For pure water, the mean values of H_{burst}/D_0 are in the range of eight to ten. With PES added to the water, the non-dimensional bag apex position H_{burst}/D_0 drops to about four. The non-dimensional drop length is decreased from $L_{burst}/D_0 = 4 - 6$ for pure water to $L_{burst}/D_0 \approx 2$ for PES emulsions.

For water, a dependence of L_{burst} and H_{burst} on the Weber number can be observed. However, almost no dependance on the Weber number can be observed in the case of the PES emulsion. Since H_{burst} can be related to the film thickness at the instant of rupture by equation (3.8), these results also indicate that there exists a critical film thickness below which the emulsion drops effectively generate holes.

However, the large standard deviations demonstrate the stochastic nature of emulsion bag breakup caused by the random distribution of the emulsion drops in the bulk liquid. Hence, the instant of time at which such an emulsion drop enters the liquid-air interface and spreads on the surface is also stochastic in nature.

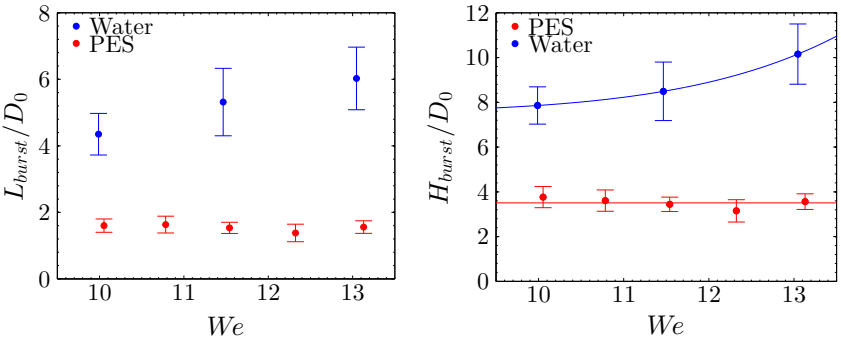

(a) Dependence of the non-dimensional burst length L_{burst}/D_0 on the Weber number.

(b) Dependence of the non-dimensional bag apex position at the instant of film rupture H_{burst}/D_0 on the Weber number.

Figure 4.9: Influence of the Weber number on the non-dimensional burst length L_{burst}/D_0 and bag apex position H_{burst}/D_0. Solid lines indicate regression curves. In the case of water, a power law model function is used. For the PES emulsion, the regression is performed using a linear model function. Vertical bars indicate two standard deviations.

4.7 Influence of polyethersiloxane concentration

To investigate the effect of emulsion drop density in the liquid film, the volume fraction c of polyethersiloxane in water has been varied between $c = 10^{-4}\%$ and $c = 1\%$. All experiments are conducted at We ≈ 12. Again, each experiment has been repeated ten times.

The effects of PES concentration on mean values and standard deviations of L_{burst} and H_{burst} are shown in Figure 4.10. It can be noted that mean values of L_{burst} and H_{burst} decrease monotonically with increasing PES concentrations. This behaviour can be explained by the larger density of emulsion drops in the film, which increases the probability that a emulsion drop enters the interface and nucleates a hole at one instant of time.

The gradient of the fitted curves also decreases with Weber number and the bag length and bag apex position at the instant of film rupture converge to limiting values. At high PES concentrations the liquid film is saturated

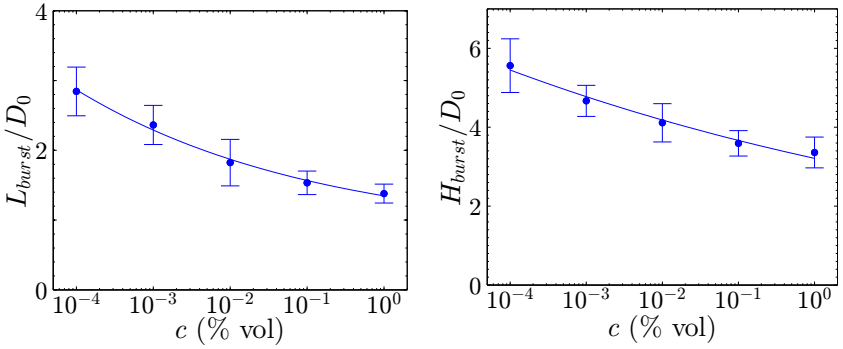

(a) Influence of the polyethersiloxane concentration on the normalized burst length L_{burst}/D_0.

(b) Influence of the polyethersiloxane concentration on the normalized burst apex position H_{burst}/D_0.

Figure 4.10: Burst length and burst apex position as a function of the PES concentration at $We \approx 12$. Solid symbols indicate mean values of ten independent experimental runs. Vertical bars represent two standard deviations. Solid lines show power law regression curves.

with emulsion drops so that an additional amount of active ingredient would have no significant effect. Here, this saturation is apparently reached between $0.1\% < c < 1\%$.

Additionally, one can observe that standard deviations tend to become smaller for increasing concentrations. Such behaviour can again be understood by considering the larger density of emulsion drops present in the liquid. Once the film thickness reaches the critical limit at which holes can be nucleated, the larger density of emulsion drops decreases the average time needed for an emulsion drop to reach the interface and spread.

In addition to the length scales at the instant of film rupture, the number of holes nucleating in the liquid sheet is influenced by the concentration of PES. Figure 4.11 shows the overall number of holes that can be observed in the liquid film during the breakup process. This number is evaluated manually from the high-speed visualizations. As before, mean values and standard deviations from ten independent runs are presented for each concentration in the range $10^{-4}\% < c < 1\%$, .

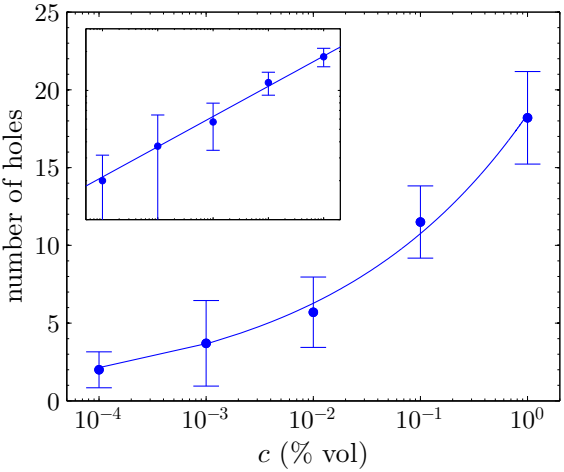

Figure 4.11: Total number of holes being observed in the lamella during the fragmentation process. A power law regression curve is shown as a solid line. The small figure shows the same data in double logarithmic scaling. The number of holes is measured manually, with an uncertainty of about ±20%, since only a side view of the drop is accessible from the visualizations.

For pure water bag breakup events, a single hole can typically be observed, as shown in Figure 3.3. When polyethersiloxane is added to the water with a concentration of $c = 10^{-4}\%$, the number of holes N varies mostly between one and three. The number of holes increases monotonically with PES concentration. For the most commonly used concentration of $c = 0.1\%$, the typical number of observed holes is in the range of 9 - 14. The experimental data can be well represented by a power law function

$$N = 18.43\, c^{0.234}. \tag{4.10}$$

It should be noted that the number of nucleated holes in the film increases much slower than the number of emulsion drops present in the liquid. Assuming that the emulsion drop size distribution is independent of the concentration, the number of emulsion drops in a certain amount of liquid is directly proportional to the concentration. Comparing concentra-

tions of $c = 10^{-4}\%$ and $c = 1\%$ yields a ratio of drop number densities of 1/10000. However, the number of nucleated holes is only increased by a factor of roughly ten. This demonstrates that the hole nucleation efficiency is not proportional to the number of emulsion drops.

It is also interesting to note that the number of generated holes is considerably increased between $c = 0.1\%$ and $c = 1\%$, while the bag length L_{burst} and apex position H_{burst} remain almost unaffected by the larger concentration.

4.8 Liquid film thickness at the instant of rupture

In section 3.5, a theoretical model for the temporal evolution of film thickness during bag breakup has been presented. For drops consisting of pure liquids, a comparison between the film thickness measured from rim velocities of holes and model predictions has been made and good agreement is shown. Since holes in the liquid film can only be observed at the end of a drop's lifetime, a model validation is performed for rather large values of H/D_0.

The addition of PES emulsion significantly decreases the bag apex position at film rupture, as demonstrated and discussed in the previous section. The film thickness at the instant of film rupture can again be measured by determining the rim velocities. However, in the case of added PES this occurs at much smaller values of H/D_0 due to the earlier breakup. Figure 4.12 depicts the comparison of film thicknesses similar to Figure 3.10, in which additional experimental results obtained with PES emulsion drops are shown.

One can recognize that the agreement between theoretical model predictions and measurements is again good. This confirms the applicability of the model over the complete range of observed bag apex positions H/D_0. The majority of PES drops burst within $2.5 < H/D_0 < 3.5$, which corresponds to normalized film thicknesses of $0.007 < h/D_0 < 0.035$. The applicability of the theoretical model for bag breakup of emulsions allows the estimation of liquid film thicknesses at the instant of burst from the bag apex positions.

Figure 4.13 shows the normalized liquid sheet thickness at the instant

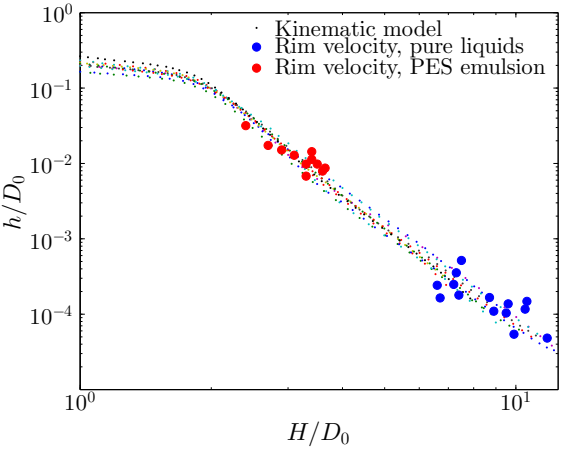

Figure 4.12: Evolution of the dimensionless film thickness h/D_0 as a function of H/D_0. Comparison of the measurements using Eqs. (3.5) and (3.7) for pure liquids and polyethersiloxane emulsions with a concentration of $c = 0.1\%$.

of burst h_{burst}/D_0 for PES emulsions in comparison with the ones of pure liquids, as previously depicted in Figure 3.11. It can be noted that the burst film thicknesses of emulsion drops are generally much larger than it is the case for pure liquids. The ratio of film thicknesses decreases from about 1/10 at low Weber numbers to about 1/100 at higher Weber numbers. For PES, the film thickness at the instant of bag rupture appears to be independent of the Weber number.

The evolution of burst film thicknesses with increasing PES concentrations at $We \approx 12$ is shown in Figure 4.14. The normalized burst film thickness is increased by around one order of magnitude when the PES concentration is changed from $c = 10^{-4}\%$ to $c = 1\%$. The values of h_{burst}/D_0 are very well represented by a power law regression curve in the range of $10^{-4}\% < c < 10^{-1}\%$. The values of the highest concentration $c = 1\%$ deviate from that trend which again indicates that the PES concentration is close to a saturation limit.

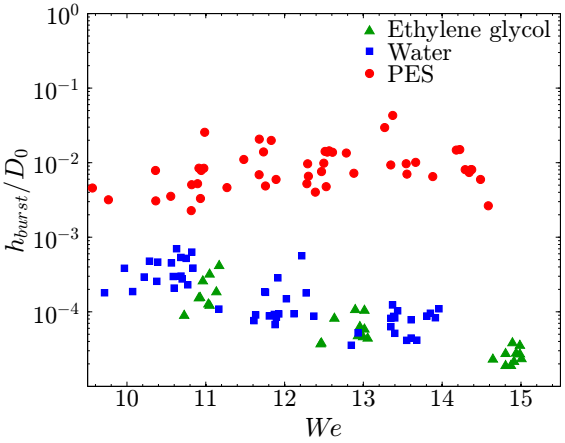

Figure 4.13: Dependence of the mean film thickness h_{burst} at the instant of film rupture on the Weber number for pure liquids and PES emulsions with a concentration of $c = 0.1\%$.

4.9 Influence of polyethersiloxane on child drop sizes

The result of the film breakup promoted by the polyethersiloxane emulsion on the final drop size distribution generated by aerodynamic fragmentation is analyzed using the image based drop sizing technique described in section 2.1. A time-resolved image sequence of each bag breakup event is recorded. From this sequence, a single frame is then extracted at the instant of complete bag disintegration. At this time, the toroidal rim is still intact. Samples of the raw images used for measuring drop sizes are shown in Figure 4.15 for water and polyethersiloxane emulsion. The rim has been excluded from the drop size measurements, since the focus of this study is placed on fragmentation of the liquid sheet that forms the bag.

The optical magnification of the high-speed video system has been adjusted to yield 27 µm per pixel. Nevertheless, very small objects cannot be reliably detected by the image processing technique. Hence, a threshold of 3×3 pixel has been chosen and drops smaller than this value are excluded from the measurement. For each case, 100 breakup events have

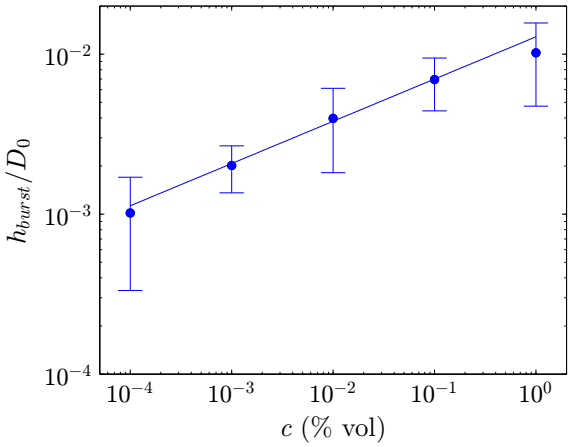

Figure 4.14: Dependence of the mean film thickness h_{burst} at the instant of film rupture on the emulsion concentration. The length of the vertical bars indicates two standard deviations. The solid line represents the best fit of the data at concentrations $10^{-4}\% < c < 10^{-1}\%$ using a power function, the obtained correlation is $h_{burst}/D_0 = 0.013\, c^{0.264}$.

been recorded, which resulted in 30000 detected drops for water and 7000 detected drops for the PES emulsion.

The outcome of the drop size measurement is presented in Figure 4.16 in the form of volume density distributions. The most apparent effect of the emulsion is the shift of the distribution towards larger drops. The peak of the distribution obtained from the atomization of water drops is at $D/D_0 = 0.085$, whereas this value is shifted to $D/D_0 = 0.135$ when the additive is added. This shift towards larger drops also reduces the volume included in drops being smaller than $D/D_0 < 0.05$ by a factor of almost five.

The results presented in this chapter demonstrate that the employed polyethersiloxane emulsion substantially accelerates the rupture of thin liquid films when compared to pure water. The liquid mass fraction contained in small drops is significantly reduced as a result of the promoted film rupture. One can expect that the emulsion shows similar effects when

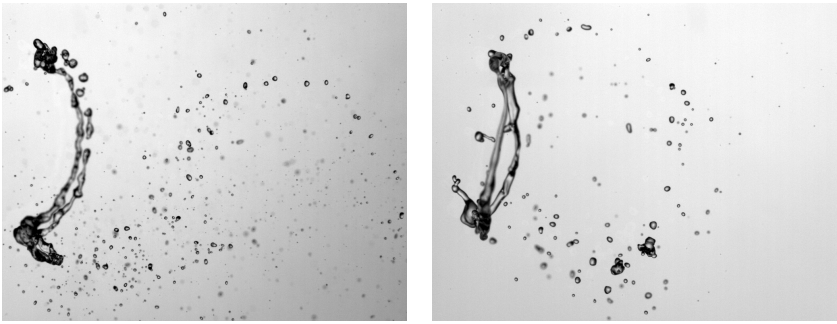

(a) (b)

Figure 4.15: Samples of the images used for measuring drop sizes being generated by atomization of the bag. The left image (a) shows the fragments originating from a water drop, the right image (b) shows fragments produced by atomization of a PES drop.

dispersed by agricultural nozzles. While time scales and length scales of aerodynamic breakup and liquid sheet fragmentation from fan spray nozzles are rather close to each other, their breakup morphologies are different. The further experimental investigation of the effects of the polyethersiloxane emulsion on agricultural sprays is thus indispensable.

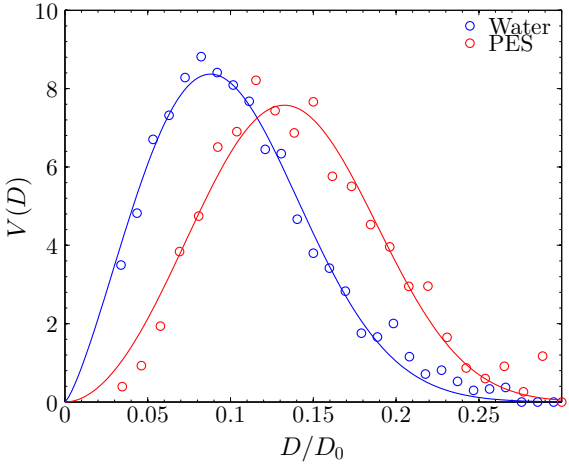

Figure 4.16: Comparison of measured volume density distributions originating from bag breakup events of water and PES emulsion. Drops being produced by the disintegration of the rim are not considered in this statistic. $We \approx 12$.

5 Breakup morphology of liquid sheets generated by flat fan nozzles

5.1 Literature Review

The dynamics of liquid sheets and their breakup behaviour have been studied since 1833, when Savart presented four studies investigating planar and bent liquid films [56–59] to characterize cohesive forces in liquids. In these studies, liquid sheets were generated by the impact of a liquid jet onto a flat disk, jet impact onto a cylinder and the collision of two opposing jets. Current reviews about liquid sheet breakup can be found in [60] and [61].

The fragmentation of liquid sheets received wide attention with the emergence of jet engines for aeronautics and astronautics. Here, liquid films are commonly used as an intermediate step in the atomization of bulk fuel into single fragments. In most cases, a high speed air stream is used to accelerate and enhance the fragmentation. This process is referred to as airblast atomization. A comprehensive review about such methods can be found in [62].

In principal, the use of air to assist the atomization process allows to enhance control over the fragmentation processes and their outcome. Twin fluid atomization has also been considered for agricultural applications [63, 64], but minor advantages and an increased system complexity have prevented a technology change. Today, the major part of crop protection agents is still atomized by pressure driven fan spray nozzles and the focus of this literature survey is placed on liquid sheet breakup without gas assistance.

The shapes of water-bells formed by liquid jets impacting onto deflection targets are observed experimentally and described theoretically by Taylor in [65]. In [66], a photographic method was employed to investigate the effect of liquid density, viscosity and surface tension on the breakup of liquid sheets.

The effect of surface tension can mainly be observed at the edges of the

liquid sheet where rims are formed. Since the growth rate of disturbances on the rims increases with surface tension [67], the edges of such sheets can be stabilized by lowering the surface tension. Viscosity reduces disturbances and hinders their growth [68] so that viscous liquid sheets have larger intact lengths.

In [69] tracers were added to the liquid sprayed through a flat fan nozzle. The pathlines of these tracers were then visualized by taking long exposure photographs of the liquid sheet. It was shown that all particles move along a straight line and are do not exhibit an angular velocity component. The motion in the liquid sheet can thus be considered as two-dimensional. Furthermore, it has been reported that the film thickness in the sheet is inversely proportional to the distance from the orifice. The film thickness distribution in liquid sheets can be revealed by interferometric methods [70, 71].

The breakup of such liquid sheets is either induced by global instabilities or by local film rupture leading to expanding holes. The growth of such global instabilities, which manifest as waves on the liquid surface, has been investigated in various studies [70, 72, 73]. The presence of symmetrical and antisymmetrical waves on liquid sheets is demonstrated in [48]. While antisymmetrical waves could easily be visualized by direct imaging, the confirmation of the existence of symmetrical waves was only possible with the help of Schlieren images. It has been demonstrated that the propagation velocity of antisymmetrical waves corresponds to the well-known velocity of a free liquid rim $V_{rim} = \sqrt{2\sigma/\rho h}$, which is derived from the balance of the inertia of the liquid entering the rim and surface tension [74]. This result was independently confirmed by Culick [75].

An experimental and theoretical investigation of liquid sheets generated by jet impact is presented in [76]. It is shown that structures resembling fluid fishbones can be produced by Rayleigh-Plateau instabilities in a given parameter range. The observed fluid fishbones exhibit a very regular breakup morphology with very little fluctuations of the sheet shape. A classification of liquid sheet breakup regimes can be found in [77].

The effect of ambient gas density on the stability of liquid sheets was investigated in [78]. It has been demonstrated that lower ambient densities decrease liquid-gas interactions and hinder the occurrence of aerodynamic flapping instabilities. In such cases the sheet is ruptured by a hole nucleation mechanism. Hole nucleation was observed in experiments with deaerated water, too. Therefore the authors concluded that dissolved gases

forming small bubbles in the liquid phase cannot be responsible for film puncturing. However, it was noticed that the nucleation of holes is always accompanied by the presence of ripples on the surface of the liquid sheet.

It has been long known that the presence of gas cavities in the near nozzle region can influence the breakup morphology and the resulting drop size distributions considerably. While the hole nucleation in homogeneous liquid films is not completely understood, two mechanisms for the generation of such cavities in the liquid phase are presently known. Gas bubbles can be injected into the liquid before it exits the nozzle. The bubbles then expand after leaving the injection system due to the pressure drop between nozzle and ambient atmosphere and promote liquid breakup. This mechanism is known as *effervescent atomization* and is mainly considered with respect to fuel injection. A review of this technique is given in [79]. A recent study about the effect of air bubbles on the fragmentation of planar liquid sheets can be found in [80]. It was noted that the ligament structure generated by the bursting of air bubbles is very similar to the pattern observed after dewetting of a thin polymer film [81].

The nucleation of holes in liquid films can also be precipitated by emulsion particles dispersed in the liquid phase, as reported in [66]. The principal mode of action of such emulsion particles has been described in 4.2. The application of this technique is rather simple and does not require any changes to the nozzle or the overall liquid supply system. However, its application is presently limited to agricultural sprays.

The effect of emulsions on the breakup morphology of agricultural fan sprays is studied in [82] and [83]. The nucleation of expanding holes in the film generates a web of connected ligaments which is further fragmented in single drops by capillary instabilities. The authors provide experimental evidence that the length of the intact liquid sheet is considerably shortened by this mechanism. At the same time, it is shown that the volume flux distribution of fan spray nozzles remains almost unchanged by the addition of adjuvants to the liquid.

5.2 Time averaged flow field of the liquid sheet

Consider a cylindrical coordinate system $\{r, z, \varphi\}$ as shown in Figure 5.1. The symmetry plane of the liquid sheet corresponds to $z = 0$.

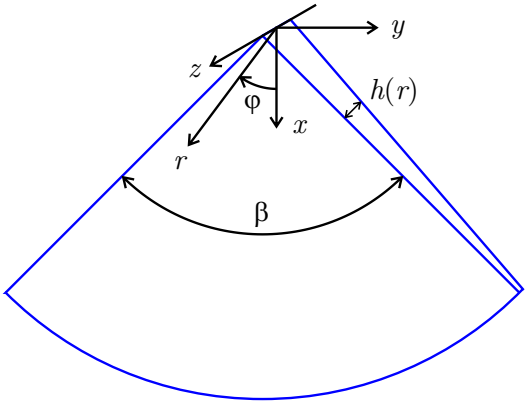

Figure 5.1: Sketch of the intact part of the lamella. The motion of the lamella is described in cylindrical coordinates $\{r, z, \varphi\}$. The opening angle of the liquid sheet is denoted by β, h is the film thickness.

The velocity field and the pressure distribution in the liquid lamella ejected from a flat fan nozzle can be obtained from the Navier-Stokes equations for incompressible flows [84],

$$\rho_l \frac{\mathrm{D}\vec{u}}{\mathrm{D}t} = \rho_l \vec{k} - \nabla p + \mu_l \, \Delta \vec{u}, \tag{5.1}$$

as well as the continuity equation for incompressible flows

$$\nabla \cdot \vec{u} = 0. \tag{5.2}$$

The flow in the intact part of the lamella is quasi-steady and almost two-dimensional. Additionally, the flow is dominated by inertia, it is therefore reasonable to neglect viscous, capillary and body forces. Equation (5.1)

can now be simplified and yields a constant radial velocity

$$u_r = C. \tag{5.3}$$

The constant C can then be estimated using the well known Bernoulli equation extended to account for pressure losses.

$$C = \sqrt{\frac{2\Delta p}{(1+\zeta)\rho_l}}, \tag{5.4}$$

where Δp is the difference between injection pressure and ambient pressure and ζ is the loss factor. The loss factors have been estimated empirically from manual velocity measurements in the liquid sheet. For air-induction nozzles, a loss factor of $\zeta = 1.7$ is obtained, while the standard fan spray nozzle exhibits much lower pressure losses with $\zeta = 0.3$. The accuracy of these measurements is in the order of $\pm 10\%$.

The evolution of the liquid film thickness h in the lamella can now be estimated from the integral form of the continuity equation for steady flows

$$\iint\limits_{(S)} \rho\, u_i\, n_i \,\mathrm{d}S = 0. \tag{5.5}$$

Together with the volume flux

$$\dot{V} = \int\limits_{-\beta/2}^{\beta/2} \int\limits_{-h/2}^{h/2} u_r\, r \,\mathrm{d}\varphi \,\mathrm{d}z, \tag{5.6}$$

equation (5.5) yields

$$h = \frac{\dot{V}}{r\,\beta\,u_r}, \tag{5.7}$$

where β is the opening angle of the lamella. Hence, the film thickness decreases with $h \sim 1/r$. The axial velocity at the air/liquid interface can now be obtained as

$$u_z\big|_{z=z_{int}} = \frac{\mathrm{d}h}{\mathrm{d}r}\,\frac{u_r}{2} = -\frac{\dot{V}}{2\,\beta\,r^2}, \tag{5.8}$$

where z_{int} is the z-position of the interface. For reasons of symmetry, the axial velocity u_z vanishes at $z = 0$.

Figure 5.2 shows the evolution of the liquid film thickness calculated from equation (5.7) for nozzles #1 - #5. The properties of these nozzles are presented in table 5.1.

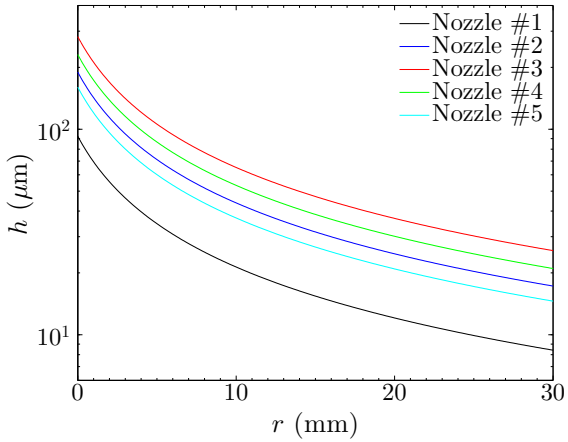

Figure 5.2: Evolution of the liquid film thickness for the fan spray nozzles considered in this study. The film thickness $h(r = 0)$ corresponds to the liquid sheet thickness at the exit of the respective nozzle.

5.3 Experimental methods

5.3.1 Test rig

A new test rig has been designed and built for the experimental investigation of agricultural flat fan nozzles. This test rig allows continuous operation of almost all kinds of commercially available agricultural nozzles under laboratory conditions. It provides optical access to the near nozzle region of the spray and to regions further downstream, where fragmentation has completely ceased. The easy optical access allows the application of various optical measurement techniques such as direct imaging and phase Doppler. The main features of this test rig are depicted in Figure 5.3.

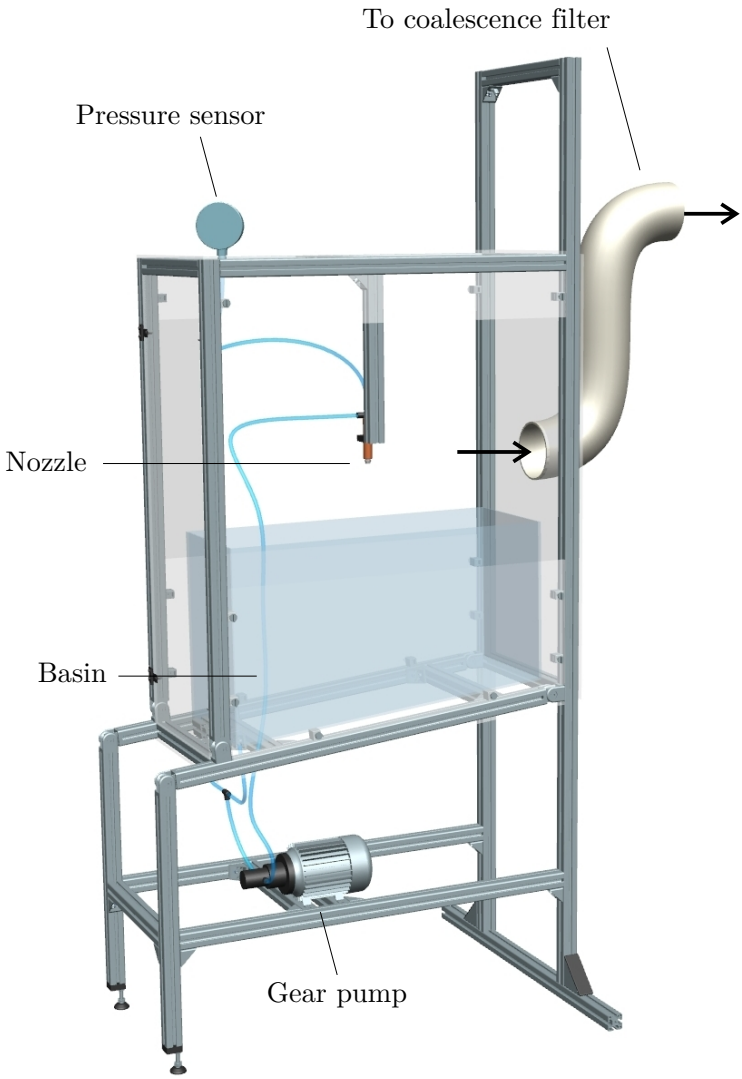

Figure 5.3: Test rig used for the experimental investigation of liquid breakup at agricultural flat fan nozzles.

A gear pump (Gather Industrie GmbH, Series 1) is used to transport the liquid to the nozzle and to provide the injection pressure needed for liquid atomization. The motor speed of the pump and thereby the injection pressure can be controlled by an electronic frequency converter. The maximum pressure difference compared to the ambient is 8 bar at a liquid volume flux of 5 liters per minute. Besides having suitable characteristics in terms of pressure and volume flux, the pump has two major advantages for the operation of agricultural nozzles. First, gear pumps are generally known to have a rather small amplitude of pressure oscillations compared to other types of pumps. Second, the pump is capable of being cleaned in place without opening the machine housing. There are no dead-water zones at the inner geometry of the pump, where chemicals could be deposited.

The injection pressure is monitored by a digital pressure gauge (WIKA Model CPG1000) with a precision of 0.05% of the terminal value. A pressure range of 0 - 20 bar can be monitored by the gauge. The motor speed of the pump is adjusted manually to set the required injection pressure.

After being atomized, the liquid is collected in an acrylic glass basin. For relatively short measurements, the inlet of the pump is connected to the bottom of this basin, so that the system is operated in a closed-loop configuration. In this case the liquid can be atomized several times. In the case of longer measurements, the additives might degrade due to multiple pump and nozzles passages. In such situations, the liquid is taken from an external basin (not shown in Figure 5.3) and is atomized only once.

The test rig can completely be encapsulated with acrylic glass windows to prevent possibly harmful substances to be discharged into the laboratory atmosphere. A coalescence filter is used to suck in and clean the air from the inside of the test rig. Additionally, the filter constantly removes the small drops from the inside of the test rig and prevents the measurements to be biased by fine particles passing the detection volume several times.

In the previous chapter (see Fig. 4.10), it has been demonstrated that even tiny amounts of additive can influence the breakup morphology considerably. While this behaviour is generally intended, it poses some problems to the experimental investigation of such liquids. Since the same test rig is used for all investigations, one has to ensure that the current liquid does not get contaminated with previously used additives. To avoid such contamination effects that could falsify the results, a strict cleaning procedure has been applied when the additive was changed, as well as at the beginning and the end of each day. This cleaning procedure consists of

Nozzle number	#1	#2	#3	#4	#5
Producer	Lechler	Lechler	Lechler	Teejet	Teejet
Series	IDK	IDK	IDK	AIXR	XR
Name	90-01	90-02	90-03	11003	11003
Type	AI	AI	AI	AI	FF
Spray angle (deg)	90	90	90	110	110
Pressure range (bar)	1.5 - 6	1.5 - 6	1.5 - 6	1 - 6	1 - 4
Vol. flux, 2 bar (l/min)	0.32	0.65	0.97	0.96	0.96

Table 5.1: Overview of the various nozzles considered in this study. Nozzle types are distinguished between air induction nozzles (AI) and standard flat fan nozzles without air induction (FF).

four ten-minute purging runs with fresh, warm water, which is completely exchanged after each run. During the second run, a surfactant is added to the fresh water to remove oil-based contamination. Additionally, all hoses are exchanged after a completed test series.

5.3.2 Nozzles & Settings

The effect of polyethersiloxane on the morphology of liquid sheet breakup and its outcome is investigated using five commercially available agricultural flat fan nozzles. The types and most important parameters of these nozzles are presented in table 5.1.

In general, five nozzles from two producers are employed for this study. Four of these nozzles have an air induction mechanism to produce larger drops, nozzle #5 is a standard flat fan nozzle without air induction. Since air induction nozzles are already designed to minimize spray drift, the further optimization of such sprays by chemical additives is a very challenging test. However, it has to be noted that the sprays produced by air induction nozzles are too coarse for some applications, so that standard flat fan nozzles without air induction are still widely used.

All nozzles are operated within the pressure range recommended by the

Nozzle	Setting 1	Setting 2	Setting 3
#1	$\Delta p = 1.5$ bar, $Re = 8.89 \times 10^3$	$\Delta p = 3.5$ bar, $Re = 1.35 \times 10^4$	$\Delta p = 5.5$ bar, $Re = 1.69 \times 10^4$
#2	$\Delta p = 1.5$ bar, $Re = 1.26 \times 10^4$	$\Delta p = 3.5$ bar, $Re = 1.93 \times 10^4$	$\Delta p = 5.5$ bar, $Re = 2.42 \times 10^4$
#3	$\Delta p = 1.5$ bar, $Re = 1.54 \times 10^4$	$\Delta p = 3.5$ bar, $Re = 2.35 \times 10^4$	$\Delta p = 5.5$ bar, $Re = 2.95 \times 10^4$
#4	$\Delta p = 1$ bar, $Re = 1.26 \times 10^4$	$\Delta p = 2.5$ bar, $Re = 1.99 \times 10^4$	$\Delta p = 4$ bar, $Re = 2.52 \times 10^4$
#5	$\Delta p = 1$ bar, $Re = 1.51 \times 10^4$	$\Delta p = 2.5$ bar, $Re = 2.39 \times 10^4$	$\Delta p = 4$ bar, $Re = 3.02 \times 10^4$

Table 5.2: Overview of the injection pressures and Reynolds numbers considered in this study.

producer. Table 5.2 presents the various injection pressures and Reynolds numbers that are used for this study. However, Reynolds numbers are not directly accessible since neither velocities at the nozzle outlet nor orifice sizes are clearly known.

The procedure for the determination of Reynolds numbers is explained in the following. First, the velocity at the nozzle outlet is estimated using the Bernoulli equation $U_0 = (2\Delta p/(1+\zeta)\rho)^{1/2}$. The cross sectional area of the orifice can then be determined from the known volume flux $A = \dot{V}/U_0$ and the equivalent diameter $D_e = (4A/\pi)^{1/2}$ is used as the characteristic dimension. The Reynolds number is now given by $Re = U_0 D_e/\nu$, where ν is the kinematic viscosity of water.

5.3.3 High-speed video system

The visualization of lamella breakup in the near orifice region of agricultural nozzles has been performed using a high-speed video system. This system consists of a Vision Research Phantom V12.1 high-speed camera with appropriate lens, a mercury vapor lamp and an optical diffusor. The camera is operated at a rate of 6200 frames per second and a resolution

of 1280×800 pixel. The field of view is $77 \times 48\,\mathrm{mm}^2$, which results in a spatial resolution of 60 µm per pixel. A sketch of the experimental setup is shown in Figure 5.4.

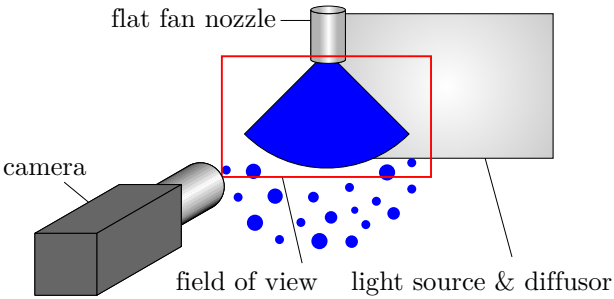

Figure 5.4: Experimental setup for the investigation of the liquid sheet fragmentation.

5.4 Observations

High-speed visualization of the lamella breakup process has been performed for all nozzles and settings presented in tables 5.1 and 5.2. In the following section, results are shown for air-induction nozzle #4 and standard fan spray nozzle #5. The visualizations, discussions and findings concerning nozzle #4 can easily be transferred to the other air-induction nozzles #1-3.

Figures 5.5 and 5.6 show the lamella breakup morphology of nozzle #4 at injection pressures of $p = 1$ bar and $p = 4$ bar, respectively.

In Figure 5.5a, the air bubbles entrained into the liquid phase can clearly be recognized below the orifice. As a result of the air-liquid mixing process, capillary waves can also be observed on the surface of the lamella. Bursting air bubbles act as hole nuclei and expand while being advected downstream with the flow. A rim is formed along the perimeter of each expanding hole which collects liquid from the lamella. At a certain point, several holes interfere with each other so that the lamella is not able to expand any further and breaks up.

(a) Water

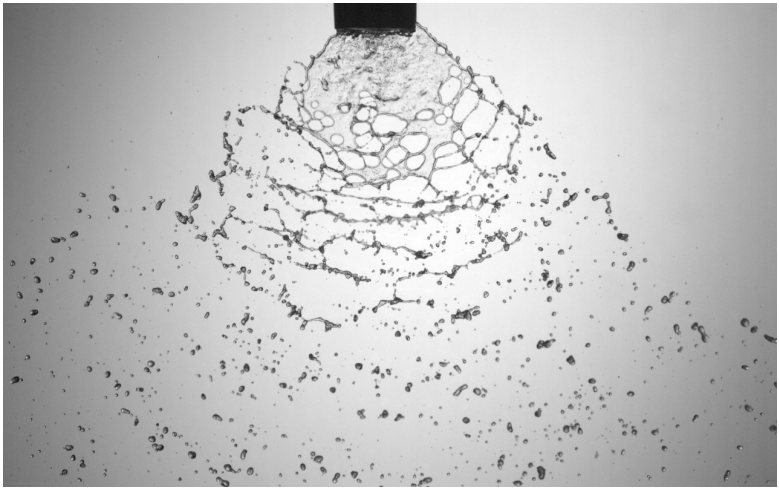

(b) PES Emulsion

Figure 5.5: Comparison of lamella breakup morphologies between water and polyethersiloxane emulsion. Nozzle #4, $p = 1$ bar.

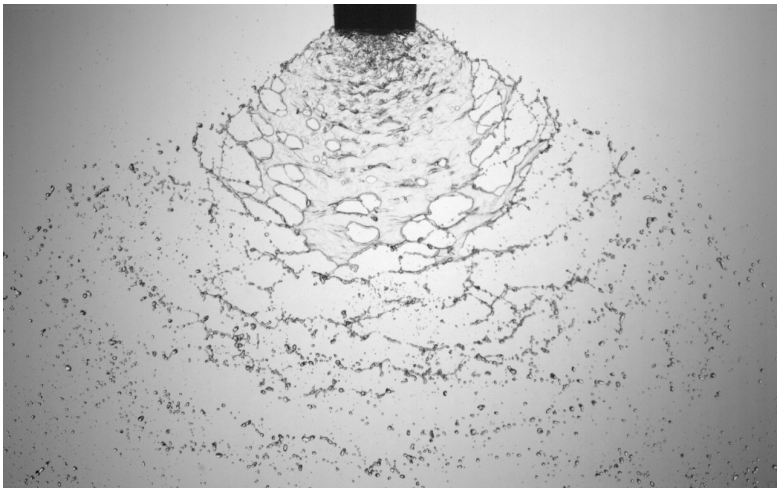

(a) Water

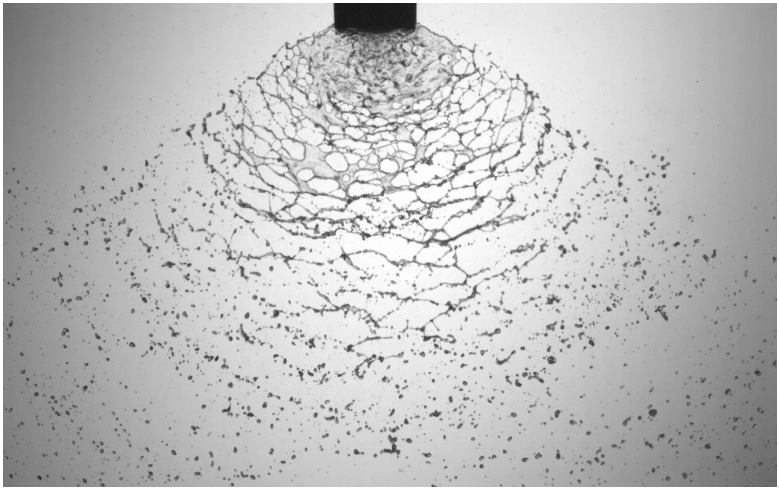

(b) PES Emulsion

Figure 5.6: Comparison of lamella breakup morphologies between water and polyethersiloxane emulsion. Nozzle #4, $p = 4$ bar.

High-speed visualization show that only a minor fraction of air bubbles present in the lamella act as hole nuclei. The major part of the bubbles is entrained by the rim of an expanding hole and can no longer generate holes in the liquid film. It can also be observed that some bubbles rupture only on one side of the lamella. In most of these cases, the liquid film is able to heal itself hereafter.

The comparison between Figures 5.5a and 5.5b shows that the hole nucleation rate is strongly increased when polyethersiloxane is added to the water. While the general breakup mechanisms are the same since holes are generated in both cases, the increased nucleation rate leads to larger number of holes which accelerates the film rupture. As a result of this mechanism, the average breakup length is shortened.

Figure 5.6 shows the atomization process at an injection pressure of $p = 4$ bar. At such injection pressures, the lamella is more jagged and the spray angle increases slightly. However, compared to smaller injection pressures, no significant change in the breakup length can be noted. Compared to pure water, the PES emulsion significantly increases the hole nucleation rate. In this case, a very fine web of connected ligaments is formed. This web is transported downstream and the single ligaments break up due to capillary instabilities. As before, the increased hole nucleation rate results in a significant reduction of the length of the intact lamella.

This shift of the breakup positions towards the nozzle leads to a larger film thickness at the instant of rupture. However, the increased hole nucleation rate limits the amount of liquid being collected by the rim of each expanding hole. Hence, the volume of ligaments being generated between colliding rims is also limited. The increased hole nucleation rate is thus responsible for two opposing effects. First, the typical thickness during film rupture is increased, which generates larger ligament structures. Second, the increased number of holes produces a finer web of ligaments and limits the liquid volume in each ligament. This could theoretically reduce the typical drop size of the final spray. The dominance of one effect over the other can not be determined from the visualizations so that drop size measurements are essential to evaluate the overall effect of the increased hole nucleation rate.

For the standard fan spray nozzle #5, which is not equipped with an air-induction mechanism, the breakup process is depicted in Figures 5.7 and 5.8. The corresponding injection pressures are $p = 1$ bar and $p = 4$ bar, respectively.

At low injection pressures, a large and rather smooth lamella can be observed when pure water is atomized, Figure 5.7a. However, some holes can still be recognized at the edges of the liquid film. The breakup of such films originating from standard fan spray nozzles is thus also affected by perforations. For expanding liquid sheets consisting of pure liquids with low opening angles β, perforations are usually observed when spraying into low pressure atmospheres [78]. For the cases considered here, the liquid sheets are rapidly expanding due to the large opening angles (see 5.1). The liquid sheet thickness is thus rapidly decreasing, which promotes the appearance of local instabilities leading to a puncturing of the liquid film.

The addition of polyethersiloxane (Figure 5.7b) increases the hole nucleation rate strongly and the breakup morphology of the liquid film completely changes. A smooth, intact lamella can only be observed in the near nozzle region. The liquid film is then rapidly transformed into a web of connected ligaments and the breakup length is greatly reduced. For an injection pressure of $p = 4$ bar, the surface of the lamella is again much more jagged. Nevertheless, the significant influence of the PES emulsion on the breakup morphology can still clearly be recognized.

5.5 Image Processing

In the previous section the lamella breakup phenomena in the near orifice region of flat fan nozzles are visualized and discussed qualitatively. From these visualizations, the shape and extent of the lamella can clearly be recognized from the images. The reader is probably able to distinguish between lamella and background with ease.

However, the lamella breakup is a highly transient and fluctuating process. The quantitative analysis of certain lamella features, such as the extent in the flow direction, requires a rather large number of samples to obtain sufficiently reliable statistics. The manual evaluation of such large data sets is barely feasible and an automated image processing algorithm is thus required. The first major step of such an algorithm is the image segmentation to extract regions covered by the liquid lamella from the raw images.

The most commonly used method for image segmentation is intensity thresholding. This class of methods uses either global or local intensity boundary values to distinguish between background pixels and object pix-

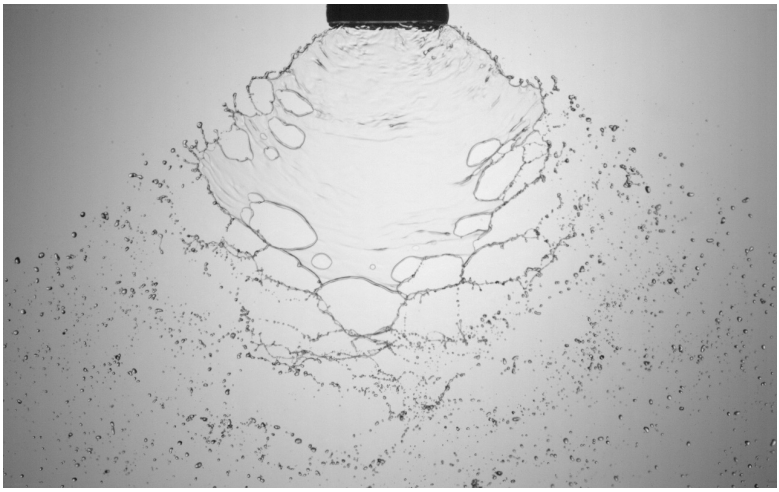

(a) Water

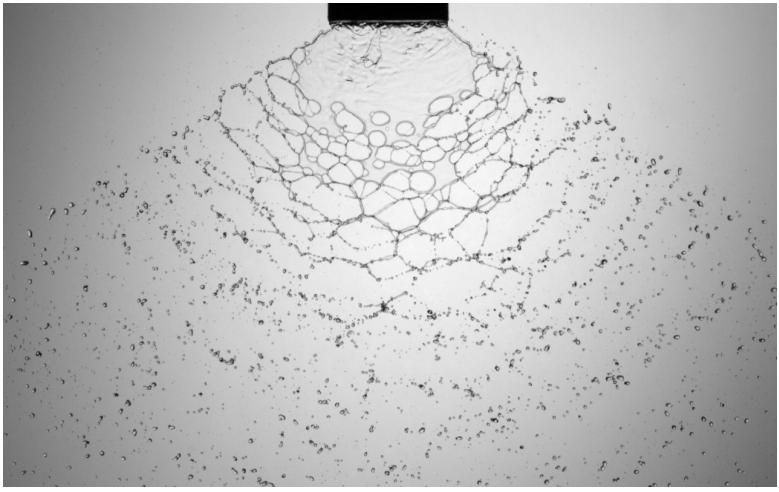

(b) PES Emulsion

Figure 5.7: Comparison of lamella breakup morphologies between water and polyethersiloxane emulsion. Nozzle #5, $p = 1$ bar.

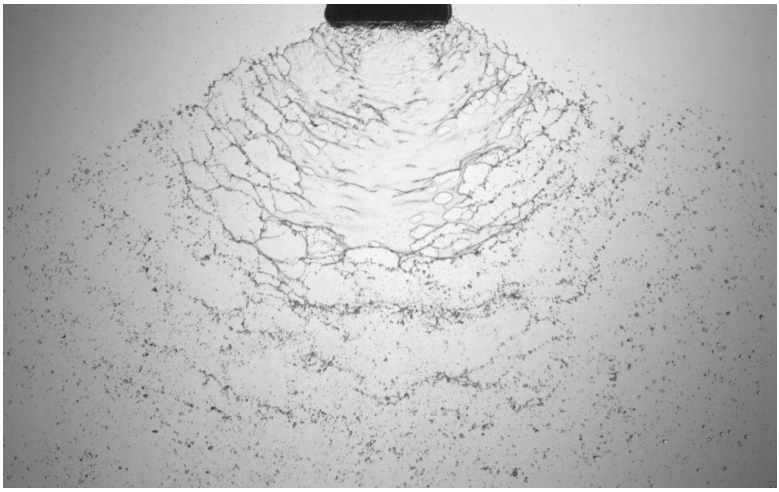

(a) Water

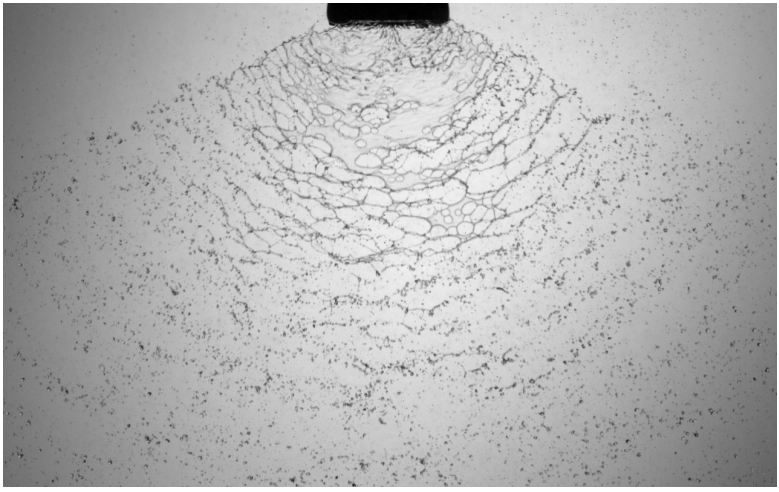

(b) PES Emulsion

Figure 5.8: Comparison of lamella breakup morphologies between water and polyethersiloxane emulsion. Nozzle #5, $p = 4$ bar.

els. This mechanism works very well in the case of single drops with a strongly curved surface. The incident light is refracted or reflected when passing the edge of a drop, so that only a small amount of incident light falls on the camera sensor. The drops' outline is thus much darker than the background (for backlit images) and can reliably be detected by such thresholding methods.

Considering a perfectly planar liquid sheet, the incident light is attenuated only by extinction. The relative amount of light being transmitted through the sheet is given by the Beer-Lambert law [13]

$$T = \frac{I_T}{I_0} = \mathrm{e}^{-\alpha h} \tag{5.9}$$

where T is the transmissivity, I_0 is the incident intensity, I_T is the transmitted intensity, α is the attenuation coefficient and h is the thickness of the absorbing material. The attenuation coefficient of water is $\alpha(\lambda = 500\,\mathrm{nm}) \approx 25 \times 10^{-3}$ [85]. For a typical water sheet ejected from a flat fan nozzle, $h \approx 100$ µm. The transmissivity is thus

$$T \approx 0.999998, \tag{5.10}$$

which is much too close to unity for the camera to resolve intensity variations caused by light extinction. For this reason, direct thresholding techniques are not appropriate for image segmentation in this case.

To overcome this problem, a texture sensitive entropy filter [86] is used for the distinction between liquid lamella and background. This filter considers the 5×5 pixel neighbourhood of each pixel and sets the center pixel intensity to

$$e = -\sum_{j=1}^{N_I} P(I_j) \log_2 \left(P(I_j) \right), \tag{5.11}$$

where e is the entropy, I is the pixel intensity value, N_I is the number of possible intensity values and $P(I_j)$ is the histogram count for intensity I_j. The obtained entropy e is a measure for the randomness in the observed neighbourhood.

This behaviour is exploited by using a very homogeneous diffusor for the background illumination. The homogeneous background intensity distribution yields rather small entropy values of e. When light is transmitted through the liquid lamella, the intensity distribution is slightly disturbed

by small capillary waves and liquid edges which are always present in the flow. The heterogeneity in intensity values is thus increased, which significantly enlarges the local entropy. The obtained entropy filtered image can then be segmented by a simple thresholding method. A binary image is then obtained, where pixels set to one are occupied by part of the liquid sheet. Finally, all binary images are added and normalized by the number of frames. Probability maps that describe the statistical distribution of liquid and gas phase are now obtained.

Examples of the images obtained by this technique are presented in Figure 5.9.

When pure water is atomized at low injection pressures, the liquid film exhibits some very smooth regions that lead to rather low entropy values. Such regions can falsely be considered as holes by the image segmentation algorithm. These falsely detected holes can be identified by their perimeter. Surface tension forms a rim at the edge of each real hole, which is not the case for falsely detected ones. The rims cause variations in the detected light intensity which then results in a rather large entropy values. A real hole can thus be identified by a large mean value of the perimeter intensity in the entropy image

$$\mathfrak{P} = \frac{1}{S} \oint_{(S)} e \, dS, \tag{5.12}$$

where e is the entropy and S is the perimeter of the respective hole. An empirically determined threshold value of $\mathfrak{P} = 0.6$ is used to distinguish between real and falsely detected holes. The hole verification is visualized in Figure 5.10.

5.6 Breakup-length: Results & discussion

The image processing algorithm presented in the previous section is now used to compare the breakup behaviour of liquid sheets consisting of pure water and polyethersiloxane emulsion. The camera has been operated at a framerate of only 100 Hz, so that all fluid elements being observed in a particular frame leave the field of view before the next frame is recorded. This ensures that each recorded frame is independent of the previous ones. For each measurement, a set of 1500 independent frames is recorded and evaluated.

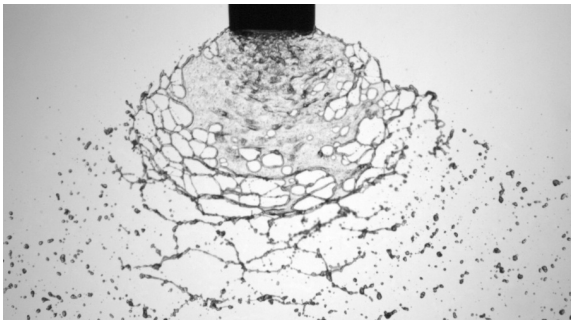

(a) Raw image

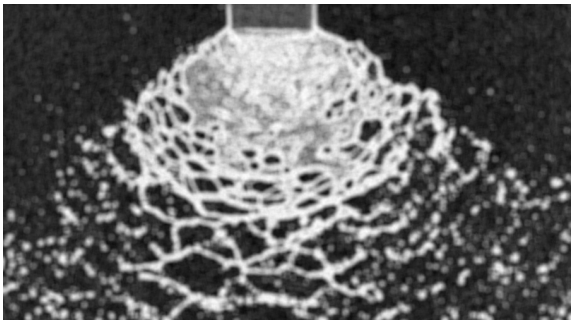

(b) Entropy filtered image

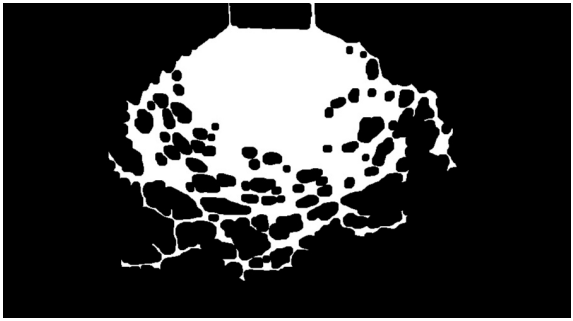

(c) Binary image of the lamella

Figure 5.9: Sample images for the entropy filtering process.

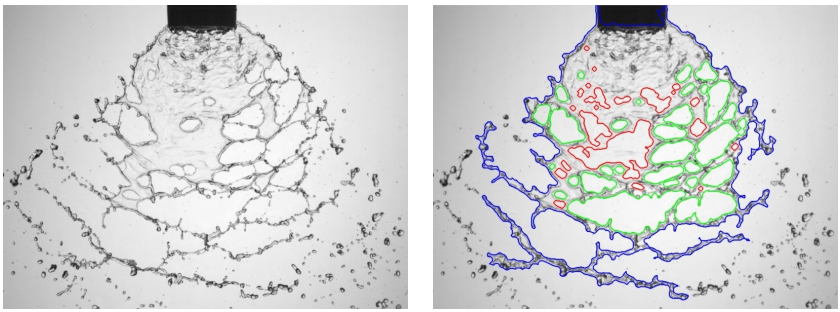

(a) (b)

Figure 5.10: Example of the hole verification mechanism. The outer contour of the lamella is depicted in blue, real holes are marked green and holes that are not verified are outlined in red.

A typical distribution of the probability Φ for one point to be occupied by liquid is presented in Figure 5.11. Close to the nozzle, a region with $\Phi = 1$ can be identified, in which the lamella is always intact. Further downstream, the probability Φ slightly decreases to values smaller than unity. This indicates the occurrence of first holes in the liquid film.

The contour line corresponding to $\Phi = 0.5$ is taken as the mean breakup line around which the lamella is fluctuating. Along the center-line of the spray, the mean breakup length R_b is now defined as

$$\Phi(r = R_b) = 0.5. \tag{5.13}$$

Figure 5.11 demonstrates that the extent of the intact lamella is significantly decreased by the polyethersiloxane emulsion when compared to water. For $(0.25 < \Phi < 0.5)$ a region with a rather heterogeneous distribution of Φ can be identified in both cases. This effect is caused by ligament structures connected to the liquid film being transported downstream.

The probability distributions Φ along the centerline of the spray are shown in Figures 5.12 and 5.13 for air induction nozzles #3 and #4, respectively.

Regarding nozzle #3, the breakup length is reduced from $R_b \approx 19$ mm for pure water to $R_b \approx 14$ mm for the PES emulsion. For nozzle #4 the

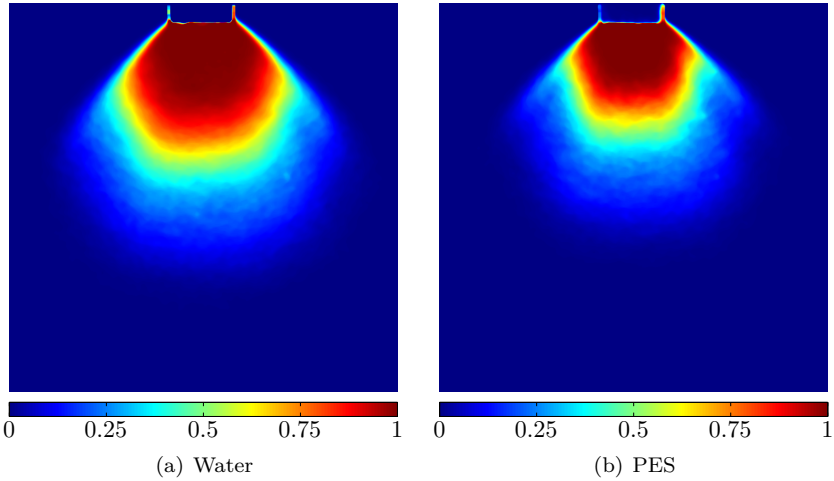

(a) Water (b) PES

Figure 5.11: Two dimensional distribution of the probability Φ to have liquid at one instant of time. Results are obtained using nozzle #4 at an injection pressure of $p = 1$ bar.

breakup length is decreased from $R_b \approx 18$ mm to $R_b \approx 13$ mm. In both cases, the mean breakup length R_b is reduced by about 25%.

The breakup lengths of nozzle #4 are slightly smaller compared to nozzle #3 which can be explained by the larger spray angle of nozzle #4 and the increased thinning rate of the liquid film. The distribution of probabilities Φ is rather insensitive to variations of the injection pressure and thereby the radial velocity in the lamella. However a slight increase of the breakup length with injection pressure can be observed. This effect can be related to the increased hole advection velocity at larger injection pressures which decreases the time for the holes to expand. The extreme case of this scenario is a resting lamella, which would completely be consumed by the expanding rim of a single hole.

In the case of nozzle #5, which is a standard fan spray nozzle without an air induction mechanism, the liquid lamella ejected from the orifice is much smoother than the ones originating from air induction nozzles. This is due to the absence of bubbles and capillary waves generated by the gas-

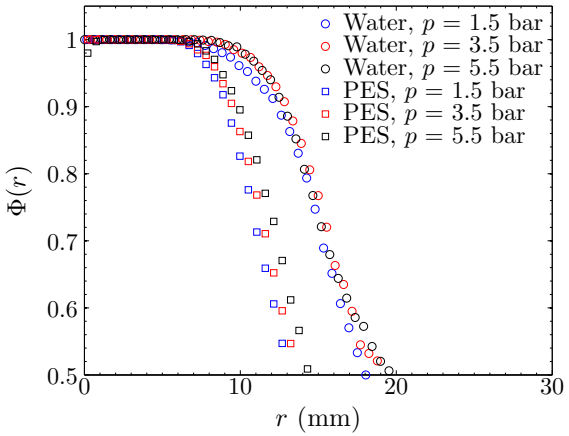

Figure 5.12: Evolution of the probability Φ for a point to be occupied by liquid along the centerline of the spray. Nozzle #3.

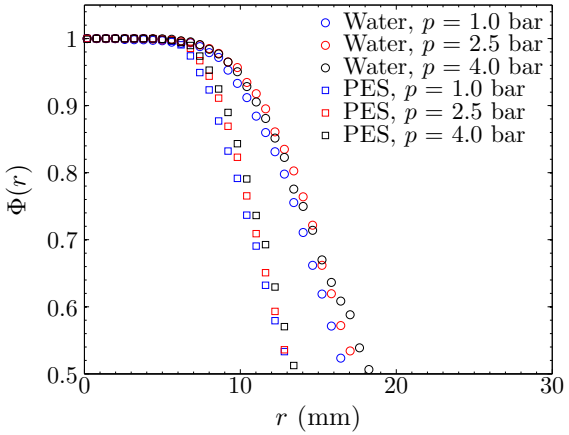

Figure 5.13: Evolution of the probability Φ for a point to be occupied by liquid along the centerline of the spray. Nozzle #4

liquid mixing process. In such situations, the entropy based structure filter used before is no longer able to detect the presence of a liquid film reliably. For this reason, the breakup lengths R of the lamella have been measured manually. For each case, a set of 50 frames is evaluated. Mean values of this measurement and standard deviations are presented in Figure 5.14.

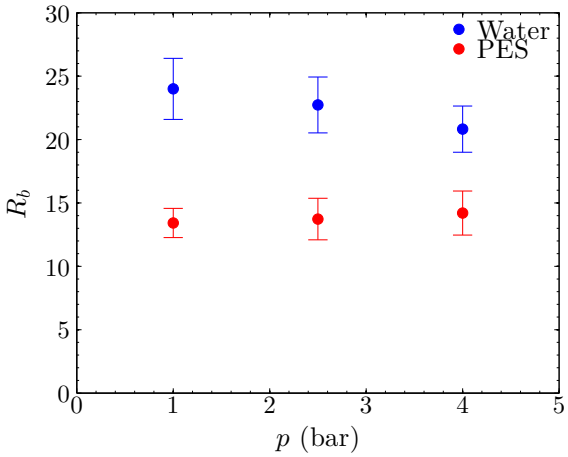

Figure 5.14: Breakup length along the centerline of the spray. Nozzle #5. Symbols indicate mean values and the length of the vertical bars represents two standard deviations.

In contrast to the results obtained at air induction nozzles, the mean breakup length decreases at larger injection pressures when pure water is atomized. This is qualitative agreement with the findings presented in [83]. Comparing the breakup lengths of water and polyethersiloxane emulsion, a reduction of 45% is observed at $p = 1$ bar. The breakup lengths approach each other when the injection pressure is increased. At $p = 4$ bar, the reduction of the breakup length is 32%.

5.7 Statistical description of liquid sheet breakup

An experimental investigation of lamella breakup has been presented in the previous section. From this analysis, the two dimensional probability

distribution for having liquid at one particular point and instant of time is obtained. The mean breakup length along the centerline R_b has been defined as $\Phi(r = R_b) = 0.5$. Let us now consider the instantaneous length of the lamella R, as shown in Figure 5.15.

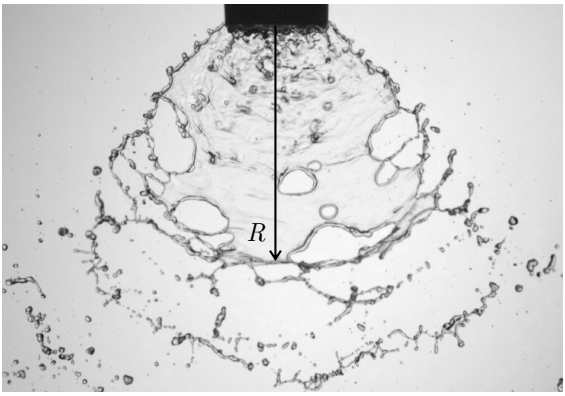

Figure 5.15: Definition of the instantaneous sheet length R.

The lamella length R fluctuates around the mean breakup length R_b. We assume that the distribution of R can be described by a lognormal distribution in the form

$$Q(r = R) = \frac{1}{r\sqrt{2\pi}\sigma} \exp\left(-\frac{(\ln(r/e^{\mu}))^2}{2\sigma^2}\right). \tag{5.14}$$

The condition to find a liquid at one particular position r is simply $R > r$. Hence, the probability for this position to be occupied by liquid is

$$\Phi(r) = \int_r^{\infty} Q(r)\,\mathrm{d}r. \tag{5.15}$$

Considering that the probability to obtain any breakup length at one instant of time equals unity

$$\int_0^{\infty} Q(r)\,\mathrm{d}r = 1, \tag{5.16}$$

equation (5.15) can now be expressed as

$$\Phi(r) = 1 - \mathfrak{Q}(r), \tag{5.17}$$

where $\mathfrak{Q}$ is the cumulative normal distribution

$$\mathfrak{Q}(r) = \int_0^r Q(r)\,\mathrm{d}r = \frac{1}{2}\left[1 + \mathrm{erf}\left(\frac{\ln(r/e^{\mu})}{\sqrt{2}\sigma}\right)\right]. \tag{5.18}$$

Combining equations (5.17) and (5.18) yields

$$\Phi(r) = \frac{1}{2}\left[1 - \mathrm{erf}\left(\frac{\ln(r/e^{\mu})}{\sqrt{2}\sigma}\right)\right] = \frac{1}{2}\,\mathrm{erfc}\left(\frac{\ln(r/e^{\mu})}{\sqrt{2}\sigma}\right). \tag{5.19}$$

Equation (5.19) can now be employed as a model for the distribution of probabilities Φ and the parameters μ and σ can be obtained by a nonlinear regression analysis of the experimental data. It can be shown that the median of the lognormal distribution e^{μ} corresponds to the mean breakup length R_b,

$$\Phi(r = e^{\mu}) = \mathrm{erfc}(0) = 0.5 = \Phi(R_b). \tag{5.20}$$

The standard deviation of the distribution $\sqrt{e^{2\mu+\sigma^2}(e^{\sigma^2}-1)}$ can be understood as a characteristic length scale for the lamella fluctuations. This characteristic fluctuation length is denoted as R'.

The mean breakup length R_b can directly be related to typical film thickness at the instant of lamella rupture. The correlation between the distance from the nozzle r and the film thickness h of the lamella is presented in 5.2. The standard deviation can now be used to define the film thickness variations during breakup. Hence, larger values of R' result in larger film thickness variations. Considering that variations in the liquid film thickness at the instant of rupture also lead to variations in the typical diameters of the generated drops, the parameter R' is an indicator for the polydispersity of the final spray.

This claim is also supported by Dombrowski and Fraser [66]: “We believe that the life history of the holes has an important bearing on the resultant drop size, and it would appear that if the perforation in the sheet could be made to occur at the same distance from the orifice, then the thread diameters and resulting drops could be made to be more uniform.”

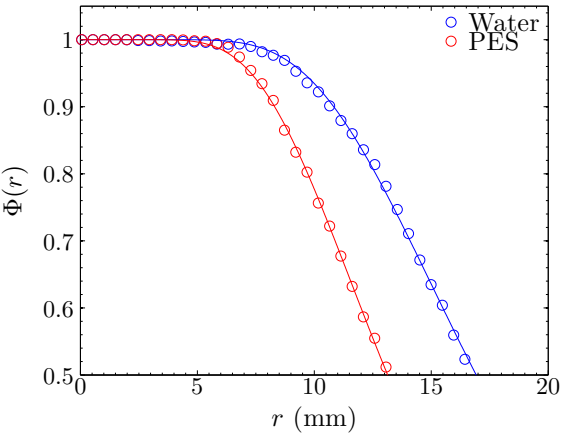

Figure 5.16: Comparison between experimental data (symbols) and the derived model functions (lines) obtained by a regression analysis. Nozzle #4, $p = 1$ bar, $Re = 1.26 \times 10^4$.

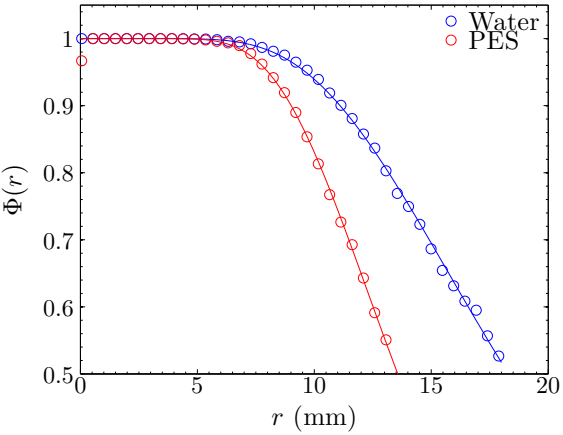

Figure 5.17: Comparison between experimental data (symbols) and the derived model functions (lines) obtained by a regression analysis. Nozzle #4, $p = 4$ bar, $Re = 2.52 \times 10^4$.

Figures 5.16 and 5.17 present typical experimental results obtained with nozzle #4 at $p = 1$ bar and $p = 4$ bar, as well as the corresponding regression curves obtained using the model function described in equation (5.19). One can observe that the proposed model is able to describe the evolution of the experimental results with very good precision. The root-mean-square error ($RMSE$) of the regression curves is between $RMSE = 0.002$ and $RMSE = 0.005$. The excellent overall agreement between experimental results and regression curves, as well as the very low deviations confirm the assumption that the distribution of lamella lengths R can be described by a lognormal distribution.

The mean breakup lengths and characteristic fluctuation length scales obtained for nozzle #4 are presented in table 5.3. The mean breakup lengths are decreased by the polyethersiloxane emulsion. Interestingly, the characteristic fluctuation length scales also decrease from $R' \approx 6.5$ mm to $R' \approx 5$ mm. These results show that the addition of PES does not only shift the mean breakup lengths to smaller values, it also limits the lamella length fluctuations. As a consequence of this limitation, one could expect that the polydispersity of the spray is decreased.

	Water		PES	
p (bar)	R_b (mm)	R' (mm)	R_b (mm)	R' (mm)
1.0	16.9	6.4	13.1	5.2
2.5	17.6	6.3	13.2	4.5
4.0	18.3	7.9	13.6	4.7

Table 5.3: Overview of the mean breakup lengths R_b and characteristic fluctuation lengths R' obtained for nozzle #4.

6 Effect of dilute emulsions on drop sizes in agricultural sprays

The previous chapter is dedicated to the description of the breakup mechanisms taking place in the near-nozzle region of agricultural flat fan sprays. The focus of the current chapter is placed on the outcome of the atomization process, drop sizes generated by fan spray nozzles, and their distributions.

6.1 Literature Review

The outcome of liquid sheet fragmentation has been addressed in numerous studies due to its significance for a variety of applications. Dimensional analysis has been used to develop a scaling law for the typical drop diameters originating from fan spray nozzles [87]. The effects of liquid properties on mean drop sizes produced by pressure-swirl nozzles are discussed in [88]. It is found that mean drop sizes become larger for increasing surface tension and viscosity. The authors further report that finer drops are obtained when the injection pressure, spray cone angle or ambient gas density is increased. An empiric correlation for the Sauter mean diameter with respect to considered parameters is often presented.

Water-sucrose-alcohol mixtures have been used to vary surface tension and viscosity almost independently [89]. The mixtures were dispersed by a pressure swirl nozzle and resulting drop size distributions were measured by a phase Doppler instrument. It is concluded that increasing surface tension shifts the overall size distribution towards larger diameters. Mean drop sizes are reported to be increased by viscosity. It is noticed that this effect especially affects the right hand side of drop size distributions, which is of particular importance when volumetric distributions are considered.

A correlation for drop size distributions being produced by ligament breakup can be found in [90]. This correlation has been used to derive an expression for drop size spectra of pressure swirl nozzles [91].

However, liquid properties cannot easily be altered in most applications and other means for controlling drop sizes have been studied. Recently, it has been demonstrated that liquid sheets can be generated by exposing dielectric liquid jets to strong electric fields [92]. The the liquid sheet width is increased for larger electric fields. This effect reduces the mean diameter of the spray and results in more uniform size distributions.

The polydispersity of sprays originating from fan spray and pressure swirl nozzles can also effectively be controlled by vibrational excitation of the nozzle [93]. The sinusoidal oscillations produce waves on the liquid sheets which lead to the generation of regular ligaments. These are subject to capillary instabilities and are further fragmented in single drops. The final diameter distributions are shown to be much narrower when the vibrational mechanism is active.

The above mentioned methods for controlling drop sizes are successful in considerably reducing the polydispersity of a spray and thereby its quality. However, for agricultural applications there is a necessity for very robust and cheap liquid dispersing systems. The rather complex apparatus needed for such spray control methods prevents such techniques to be widely used for pesticide deposition. Presently, crop protection agents are almost exclusively delivered through pressure driven standard fan-spray or air induction nozzles. For the latter, drops sizes are controlled by the injection of air bubbles into the liquid phase, as described in section 5.1 while adjuvants can be used to influence diameter distributions for both nozzle types.

A comprehensive experimental and theoretical study about the effect of air bubbles on the outcome of liquid sheet fragmentation is given in [80]. The authors use Voronoi statistics to describe the length and diameter distribution of ligaments being generated by bursting bubbles. Here too, the ligament breakup model from [90] is then used to derive a correlation of the final drop size distributions being generated by the effervescent liquid sheet atomization. It is shown that the obtained correlation is in good agreement with experimental data.

In [4], the diameter distributions of standard fan-spray and air-induction nozzles are compared by a large variety of experiments. The phase-Doppler technique has been employed to measure drop sizes. It is shown that air-induction nozzles generally lead to much larger mean diameters. However, the presented size distributions from air-induction nozzles exhibit a very atypical saw-tooth shape and the reliability of the measurements can be questioned.

The effects of some adjuvants on volume median diameters are described in various studies, including [3, 82, 94]. The authors show that mean diameters can be increased and that the amount of small drops can be reduced when oil based emulsions are added to the liquid. These studies are mainly focused on the outcome of the atomization process, a detailed description of the mechanisms leading to hole nucleation and the related effects on the fragmentation processes cannot be found in the literature.

6.2 Experimental setup

The experimental setup employed for the drop size measurements is very similar to the one that is used for the lamella visualizations (see section 5.3.1). In the following, only the most important features of the setup and deviations from the one presented before are discussed.

Spray images are recorded by a *Vision Research Phantom V12.1* camera. The camera is operated at its maximum resolution of 1280×800 pixel at a rather low frame rate of 100 Hz to obtain statistically independent images. The field of view is approximately 30 mm $\times$ 19 mm. A *Nikon* lens with a focal length of 85 mm and a maximum f-number of $N = 1.4$ is equipped to the camera. The lens is adjusted to a f-number of $N = 16$ which is a good compromise between contrast and depth of field. A sketch of the experimental setup is depicted in Figure 6.1. For each case, 1800 images are recorded and evaluated.

The camera sensor is illuminated by a mercury vapor lamp with a light output of 33000 lumen that is located on the optical axis, so that backlit images are obtained. A sample image is shown in Figure 6.2

6.3 Data processing

Raw spray images are evaluated by the drop sizing algorithm described in section 2.1, which provides a list of all detected drops and their respective diameters. Drops with similar diameters are then collected in classes with widths of $\Delta D = 40$ µm, which results in number density distributions as exemplarily shown in Figure 6.3a. The resulting drop size distributions are rather smooth for drop diameters larger than 100 µm. However, the left side of the number distribution is cropped. This is due to the fact that

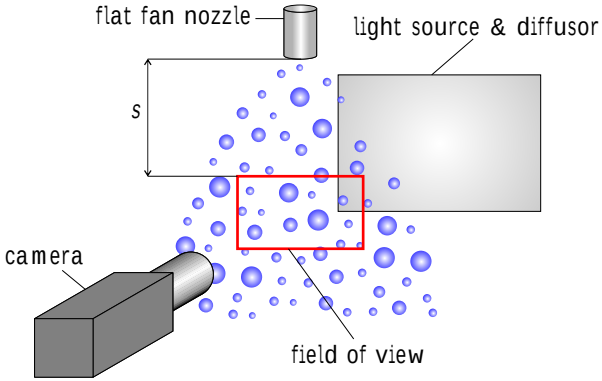

Figure 6.1: Experimental setup for image based spray characterization.

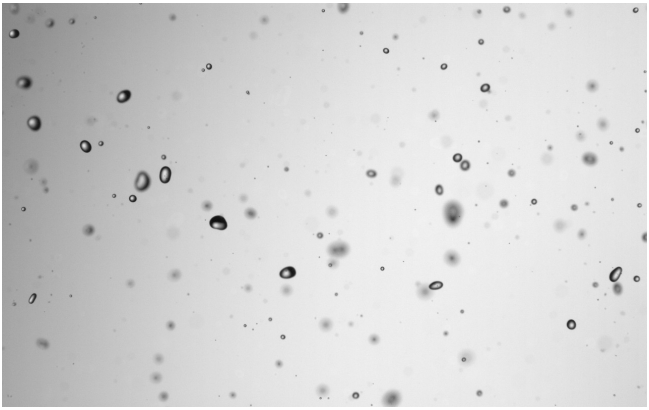

Figure 6.2: Typical raw image recorded for spray characterization.

smaller drops cannot reliably be detected any more and are removed from the result. It becomes obvious that a rather large number of small drops is not considered and that the distribution is incompletely resolved.

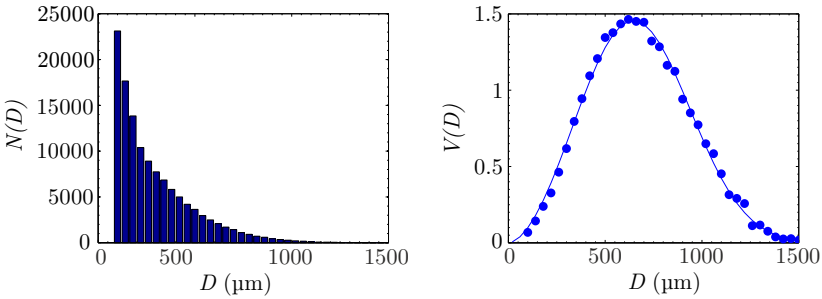

(a) Number density distribution

(b) Volume density distribution

Figure 6.3: Exemplary comparison of number density distributions and corresponding volume density distributions obtained from the image based particle sizing algorithm.

However, the number density distribution is of less interest for the applications considered here; more important is the distribution of liquid mass or volume among drop size classes. From a volume weighted distribution the amount of liquid contained in small drops that are prone to drift or large drops that result in a bad coverage of the plants can easily be assessed. The volume distribution corresponding to the number density distribution shown in Figure 6.3a is depicted in Figure 6.3b. While a large number of small drops cannot be detected, the overall volume of these drops is apparently rather small, so that volume density distributions can be resolved almost completely.

The volume fraction $\mathfrak{V}_m$ of a certain drop size class can be obtained as [95]

$$\mathfrak{V}_m = \frac{\sum_{i=1}^{N_m} \frac{1}{6}\pi D_{i,m}^3}{\sum_{m=1}^{M}\sum_{i=1}^{N_m} \frac{1}{6}\pi D_{i,m}^3} \tag{6.1}$$

where m denotes the drop size class, M the number of size classes and N

the number of drops contained in the m-th class. Here, the denominator is the absolute amount of liquid volume in the m-th size class and the denominator is the complete volume of all size classes that cover the entire drop size range.

While the absolute amount of liquid volume of a certain size can easily be computed, the entire volume is not known since data for small drops is not available. In order to normalize the obtained distributions, a regression analysis is applied. The volume distribution is approximated by the density function of a Rosin-Rammler distribution [96–98], that is defined as

$$\tilde{V}(D) = c \left(\frac{D}{a}\right)^{b-1} \exp\left(-\left(\frac{D}{a}\right)^{b}\right), \tag{6.2}$$

where a, b and c are the model constants. The entire volume is then obtained from integrating the non-normalized volume density function $\tilde{V}(D)$,

$$\sum_{m=1}^{M} \mathfrak{V}_m \approx \int_0^{\infty} c \left(\frac{D}{a}\right)^{b-1} \exp\left(-\left(\frac{D}{a}\right)^{b}\right) \mathrm{d}D = \frac{ac}{b} \tag{6.3}$$

and is used to normalize the volume density distributions, which can then be expressed as

$$V(D) = \frac{b}{a} \left(\frac{D}{a}\right)^{b-1} \exp\left(-\left(\frac{D}{a}\right)^{b}\right). \tag{6.4}$$

Equation (6.4) now satisfies the condition

$$\int_0^{\infty} V(D)\, \mathrm{d}D = 1. \tag{6.5}$$

The correct dimension is $[V(D)] = \mathrm{m}^{-1}$. However, this dimension is omitted in the graphical representations of volume distributions since the focus is placed on relative comparisons.

The Rosin-Rammler distribution is able to describe the overall experimental volume density distribution data well for all cases considered in this investigation. However, a slight deviation between the Rosin-Rammler distribution and experimental data can be observed in some cases, when only small drops are considered. The direct estimation of the drift-prone volume

that is contained in drops being smaller than 100 µm might thus lead to biased results. For this reason, the drift-prone volume fraction is estimated by considering only the left hand side of the volume density distributions, that corresponds to drops with $D < 200$ µm. A regression analysis is applied to this part of the normalized experimental data and a power law model is used

$$V(D < 200\,\mu\text{m}) = p\,D^q, \tag{6.6}$$

where p and q are model coefficients. The power law model function corresponds to the part of the Rosin-Rammler distribution that dominates for small drops. The volume fraction $\mathfrak{V}_{100}$ contained in drops being smaller than 100 µm is now estimated from

$$\mathfrak{V}_{100} \approx \int_{D=0\,\mu m}^{D=100\,\mu m} V(D < 200\,\mu\text{m})\,\mathrm{d}D \tag{6.7}$$

A graphical representation of this method is shown in Figure 6.4.

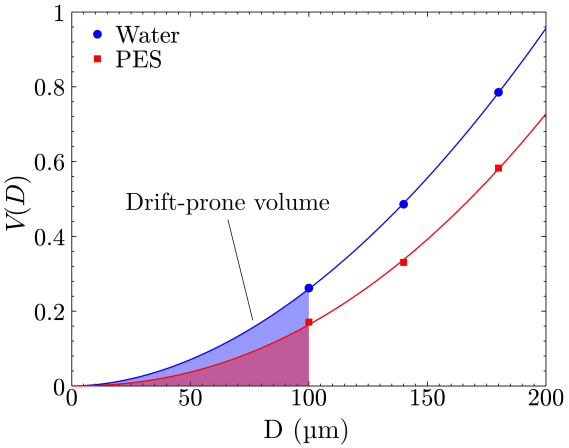

Figure 6.4: Estimation of the drift-prone volume. Nozzle #4, $p = 2.5$ bar. The ordinate is scaled by mm^{-1}.

Furthermore, several representative diameters are used to characterize and compare the drop size distributions. These are

$D_{0.1}$: drop diameter for which 10% of the total volume is contained in drops of smaller diameters

$D_{0.5}$: drop diameter for which 50% of the total volume is contained in drops of smaller diameters

$D_{0.9}$: drop diameter for which 90% of the total volume is contained in drops of smaller diameters

The diameter $D_{0.5}$ is also referred to as volume median diameter (VMD) and should not be confused with the volume mean diameter D_{30} that is defined as

$$D_{30} = \left(\frac{\int_0^\infty D^3 (\mathrm{d}N/\mathrm{d}D)\mathrm{d}D}{\int_0^\infty (\mathrm{d}N/\mathrm{d}D)\mathrm{d}D} \right)^{1/3}. \tag{6.8}$$

The difference between the representative diameters $D_{0.9}$ and $D_{0.1}$ can be used as a measure for the width of the volume distribution. Dividing this difference by the volume median diameter yields the relative span factor

$$\Delta = \frac{D_{0.9} - D_{0.1}}{D_{0.5}}, \tag{6.9}$$

which is a non-dimensional value for the dispersion of drop sizes. Sprays with very low relative span factors $\Delta \ll 1$ can be designated as monodisperse.

6.4 Measurement accuracy

The accuracy of a measurement can be described by its expectation and precision. The expectation reflects the closeness of the mean measurement values to the true value. Precision refers to the closeness of results from independent experimental runs to each other. The expectation is affected by systematic errors that cause a bias towards smaller or larger values. On the other hand, the sensitivity of a technique to stochastic errors influences the precision and, for consistent estimations, stochastic errors become smaller when the sample size increases.

The effect of systematic errors on the image based drop sizing technique has been discussed in section 2.1. In the present section the influence and the dimensions of stochastic errors are discussed. This is of particular

importance for quantitative comparisons of the results obtained for varying experimental parameters, such as nozzles types, injection pressures and atomized liquids.

A repeatability study is conducted for nozzle #4 operated at an injection pressure of 2.5 bars. Ten independent, subsequent measurements are recorded and analyzed to assess stochastic variations and to characterize the precision of the employed measurement technique. Mean values and standard deviations obtained from all runs are presented in Figure 6.5. Vertical length scales of the error bars indicate two standard deviations, which corresponds to a confidence level of 68.3%.

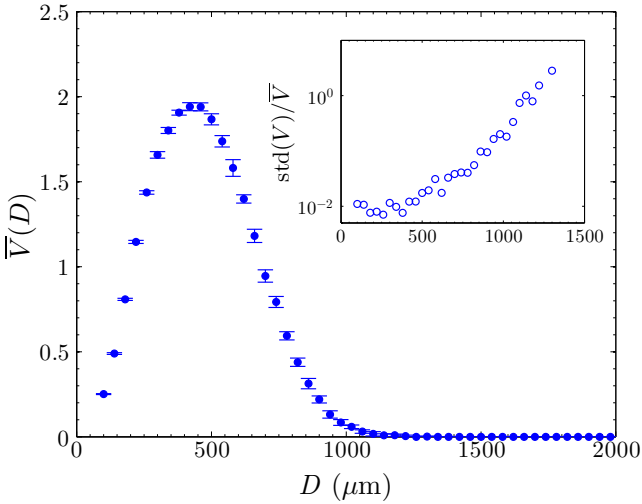

Figure 6.5: Mean values and standard deviations of ten independent experimental runs with nozzle #4 at $p = 2.5$ bar. Standard deviations are indicated by half of the error bar height. The small plot shows the relative standard deviations with respect to the drop size classes. The ordinate is scaled by mm^{-1}.

One can observe that the repeatability of the results obtained by the drop size measurements is very good. Relative standard deviations of small and medium drops are of the order of 1%.

Absolute values of the standard deviation (as indicated by the error bars)

first increase with drop size and become smaller shortly after the maximum of the size distribution is reached. This behaviour can be explained by the combination of two effects. First, the number of detected drops decreases with increasing drop size class which leads to poorer statistics and increasing standard deviations for larger drops. Second, the volume fraction decreases to $V(D) = 0$ after the maximum value is reached. For such drop sizes with $V(D) = 0$, the standard deviation also vanishes. Since a smooth evolution can be assumed, the standard deviation decreases for drop sizes located on the right hand side of the maximum value of $V(D)$.

The smaller plot in Figure 6.5 depicts the relative standard deviations $std(V)/\overline{V}$, where $\overline{V}$ is the mean volume density. The relative standard deviations are rather constant in the range of 100 µm $< D <$ 500 µm and increase for size classes $D >$ 500 µm.

The standard deviation of the volume median diameter is 1.3 µm with a mean value of 457 µm. An additional measurement conducted about two weeks later resulted in a volume mean diameter of 461 µm.

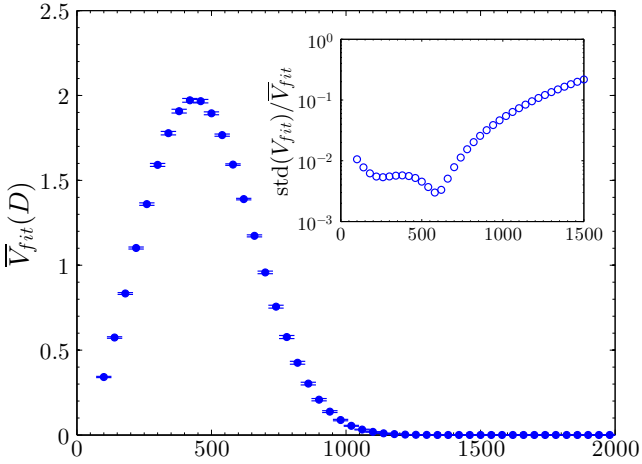

Figure 6.6: Mean values and standard deviations of Rosin-Rammler fitting functions obtained by ten independent experimental runs with nozzle #4 at $p = 2.5$ bar. Standard deviations are indicated by half of the error bar height. The small plot shows the relative standard deviations with respect to the drop size classes.

The robustness of the selected Rosin-Rammler distributions against variations in the experimental results is demonstrated in Figure 6.6. Here, mean values and standard deviations obtained from the Rosin-Rammler distributions fitted to each of the experimental runs are depicted. Particularly for medium sized drops, absolute and relative standard deviations are even lower than the values obtained directly from the experimental results. The Rosin-Rammler model functions are employed to normalize the experimental data, so that the robustness of the selected model functions is of particular importance for quantitative comparisons.

6.5 Results

In the following section, the measured drop size distributions are presented and discussed for various nozzle types and Reynolds numbers. Accounting for the differences in the breakup mechanisms involved in the atomization process, a distinction is made between air induction nozzles and standard flat fan nozzles. An overview of experimental parameters is given in Table 5.2.

6.5.1 Air induction nozzles

Nozzles #1, #2 and #3 are geometrically very similar since they originate from a single series of nozzles. In the following, only the results obtained with nozzle two are shown, as results obtained with nozzles one and three are very similar. The impact of the Reynolds number on the outcome of the fragmentation process is depicted in Figure 6.7. Mean diameters decrease for larger Reynolds numbers. This effect can be related to higher liquid velocities and stronger interactions between liquid and air. As the number of larger drops and the size of the largest drops decreases for higher pressures, absolute widths of the distributions become smaller.

The effects of the polyethersiloxane emulsion on the spray characteristics are shown in Figures 6.8 - 6.10. Considering the volume median diameter, almost no influence of the emulsion can be observed, which implies that the positions of the distribution peaks are not altered. However, the distributions become narrower in all cases. The relative span, which does not depend on the Reynolds number, decreases from $\Delta = 1.06$ for water to $\Delta = 0.95$ for polyethersiloxane emulsions, which corresponds to decline of

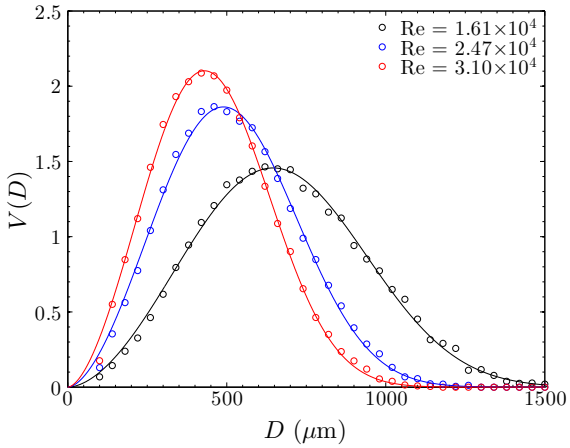

Figure 6.7: Nozzle #2, dependency of drop size distributions on Reynolds numbers, water. The ordinate is scaled by mm^{-1}.

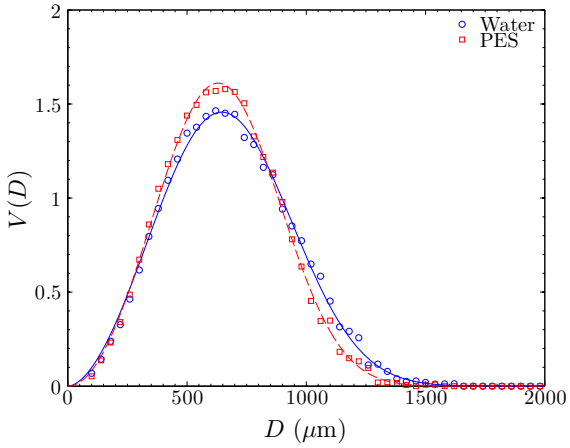

Figure 6.8: Comparison of volume density distributions obtained for water and PES emulsion. Nozzle #2, $p = 1.5$ bar, $Re = 1.26 \times 10^4$. The ordinate is scaled by mm^{-1}.

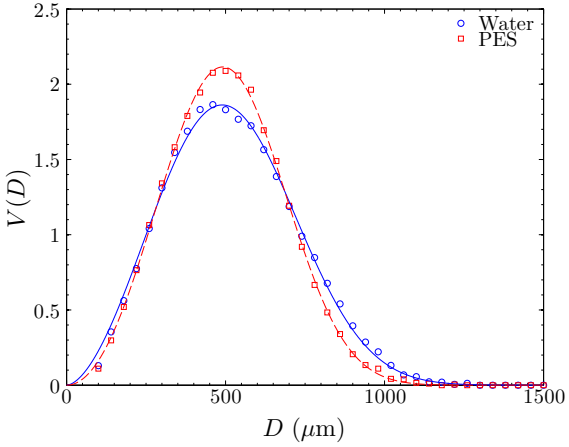

Figure 6.9: Comparison of volume density distributions obtained for water and PES emulsion. Nozzle #2, $p = 3.5$ bar, $Re = 1.93 \times 10^4$. The ordinate is scaled by mm^{-1}.

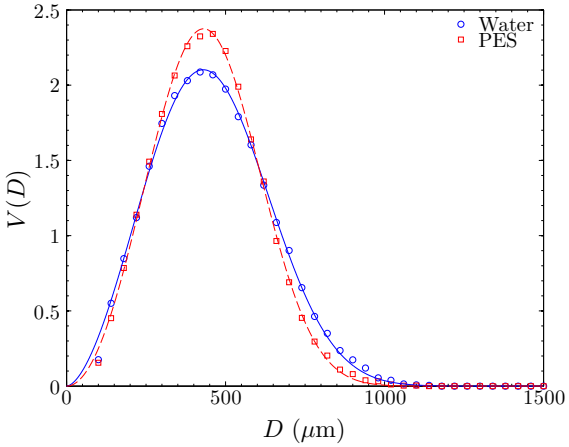

Figure 6.10: Comparison of volume density distributions obtained for water and PES emulsion. Nozzle #2, $p = 5.5$ bar, $Re = 2.42 \times 10^4$. The ordinate is scaled by mm^{-1}.

ten percent. The drift prone volume fractions of drops smaller than 100 µm in the sprays are reduced by about 10 - 20 percent, depending on the injection pressure.

Results of the drop size measurements for nozzle #4 are depicted in Figures 6.11 - 6.14. The sensitivity of drop sizes to the injection pressure is shown in Figure 6.11. Again, mean drop sizes decrease with increasing injection pressure, as expected. The volume median diameter drops from 613 µm at $p = 1$ bar to 403 µm at $p = 4$ bar.

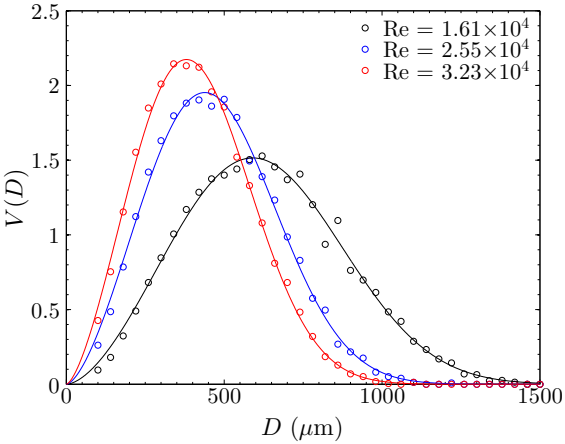

Figure 6.11: Nozzle #4, dependency of drop size distributions on the injection pressure for water. The ordinate is scaled by mm^{-1}.

For nozzle #4, the impact of the polyethersiloxane emulsion on the spray characteristics for various Reynolds numbers is shown in Figures 6.12 - 6.14. Similar to nozzle two, the volume median diameter remains almost unaffected by the emulsion, while the relative width Δ is decreased by twelve percent. The reduction of drift prone drops ranges from 18% at $\mathrm{Re} = 1.26 \times 10^4$ to 35% at $\mathrm{Re} = 2.52 \times 10^4$.

6.5.2 Standard flat fan nozzles

Figure 6.15 presents the dependance of drop sizes on Reynolds numbers. The volume median diameter ranges from 274 µm at $\mathrm{Re} = 1.51 \times 10^4$ to

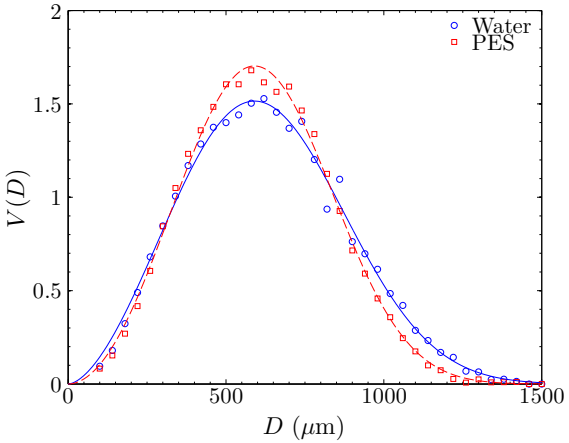

Figure 6.12: Comparison of volume density distributions obtained for water and PES emulsion. Nozzle #4, $p = 1.0$ bar, $Re = 1.26 \times 10^4$. The ordinate is scaled by mm^{-1}.

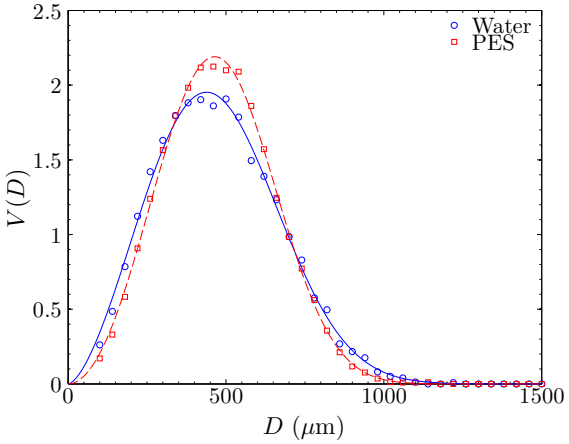

Figure 6.13: Comparison of volume density distributions obtained for water and PES emulsion. Nozzle #4, $p = 2.5$ bar, $Re = 1.99 \times 10^4$. The ordinate is scaled by mm^{-1}.

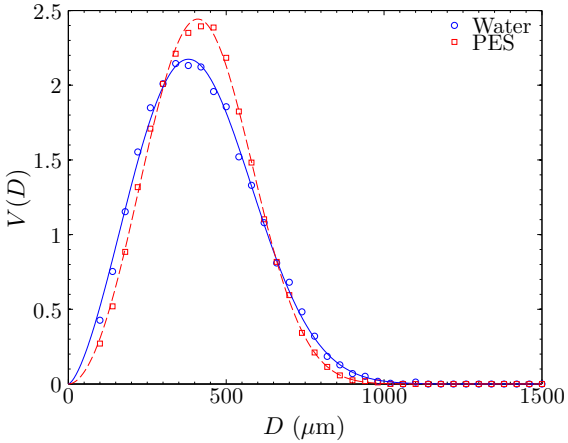

Figure 6.14: Comparison of volume density distributions obtained for water and PES emulsion. Nozzle #4, $p = 4.0$ bar, $Re = 2.52 \times 10^4$. The ordinate is scaled by mm^{-1}.

207 µm at Re $= 3.02 \times 10^4$. It is interesting to note that mean drop sizes originating from the standard flat fan nozzle are generally much smaller than the ones generated by an air induction nozzle with comparable volume fluxes and spray angles.

A comparison between drop sizes obtained with pure water and drop sizes obtained with polyethersiloxane emulsion is shown in Figures 6.16 - 6.18. In contrast to the air induction nozzles, a significant shift of the volume median diameters towards larger diameters can be observed. For the intermediate Reynolds number Re $= 2.39 \times 10^4$ the volume median diameter is shifted from 226 µm for pure water to 278 µm for the polyethersiloxane emulsion. At the same time, the relative width is reduced from $\Delta = 1.28$ for pure water to $\Delta = 0.93$ for the emulsion. This drop corresponds to a relative change of 27%.

The combination of increased volume median diameters and reduced relative widths results in a decrease of drift prone drops that ranges from about 55% to 65%, depending on the Reynolds number.

For nozzle #5, the shift of the drop size distribution towards larger diameters when polyethersiloxane emulsion is added can even be recognized

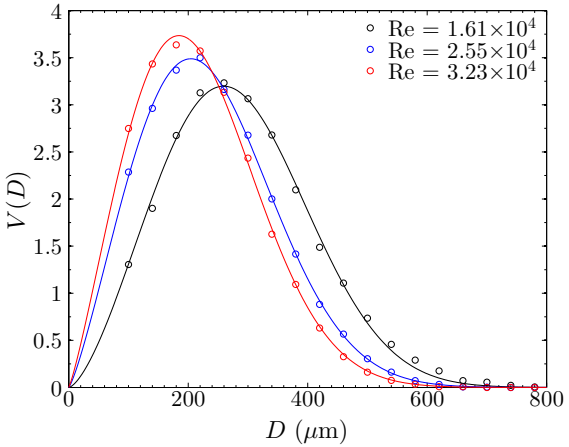

Figure 6.15: Nozzle #5, dependancy of drop size distributions on Reynolds numbers, water. The ordinate is scaled by mm^{-1}.

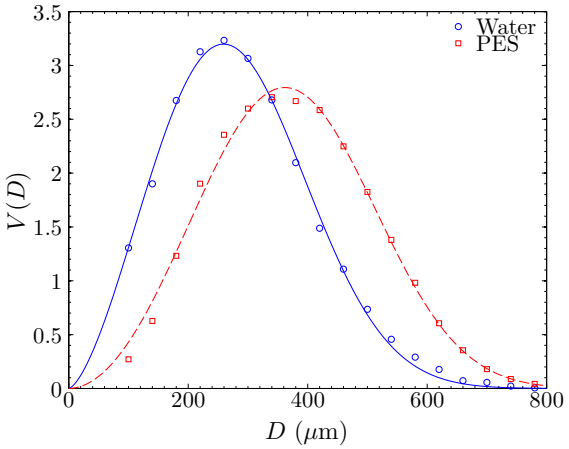

Figure 6.16: Comparison of volume density distributions obtained for water and PES emulsion. Nozzle #5, $p = 1.0$ bar, $Re = 1.51 \times 10^4$. The ordinate is scaled by mm^{-1}.

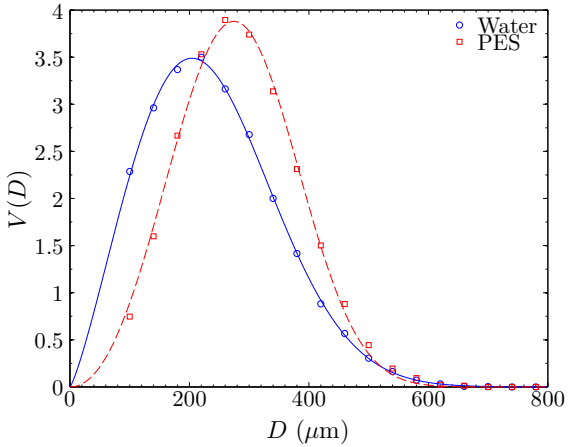

Figure 6.17: Comparison of volume density distributions obtained for water and PES emulsion. Nozzle #5, $p = 2.5$ bar, $Re = 2.39 \times 10^4$. The ordinate is scaled by mm^{-1}.

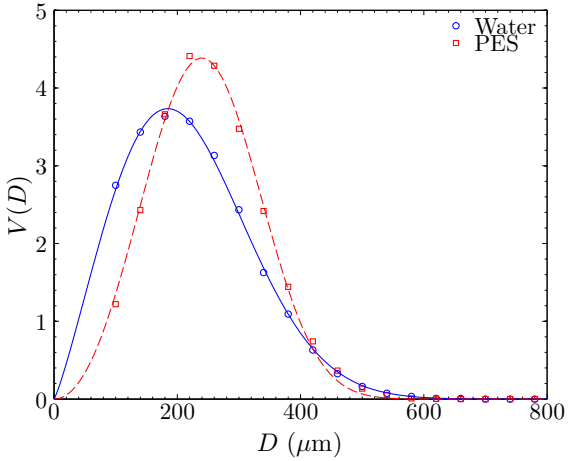

Figure 6.18: Comparison of volume density distributions obtained for water and PES emulsion. Nozzle #5, $p = 4.0$ bar, $Re = 3.02 \times 10^4$. The ordinate is scaled by mm^{-1}.

from the raw images, as shown in Figure 6.19.

6.5.3 Effect of polyethersiloxane concentration

The influence of the polyethersiloxane concentration on volume density distributions of the dispersed emulsion is assessed using nozzle #5 at an injection pressure of $p = 1$ bar. In this case, a significant shift of the volume median diameter can be observed when PES is added to the water. The amount by which the volume median diameter is shifted towards larger diameters depends on the PES concentration, as depicted in Figure 6.20.

One can observe that even small amounts of polyethersiloxane have a considerable influence on the fragmentation mechanism, so that volume median diameters increase when compared to water. A further increase of PES concentrations intensifies that effect. For concentrations of $c = 0.1\%$ vol. and higher, the emulsion is saturated and an additional increase in $VMDs$ cannot be achieved. This observation is in good agreement with the results obtained from bag breakup of single drops, as presented in section 4.7.

6.5.4 Qualitative discussion of the effect of polyethersiloxane

In the case of air-induction nozzles, two general trends can be observed when drop size distributions generated from pure water and polyethersiloxane emulsions are compared. First, the amount of liquid contained in small drops is reduced by up to about 35% when PES is added. This effect can be related to the accelerated breakup, so that ligaments are generated from relatively thick liquid films, as described in detail in Chapter 5.

The second effect is the reduction of liquid contained in the largest drops. The reason for this behaviour is exemplarily shown in Figures 6.21 and 6.22. In the case of water sprayed by an air-injection nozzle, the rather low hole nucleation rate can cause large areas of the liquid lamella being separated from the rest of the liquid film. This is demonstrated in Figure 6.21(a-b). The separated part of the lamella contracts under the influence of capillary forces acting on the peripheral region where the rim is formed. This contraction continues until a single ligament is formed, as shown in Figure

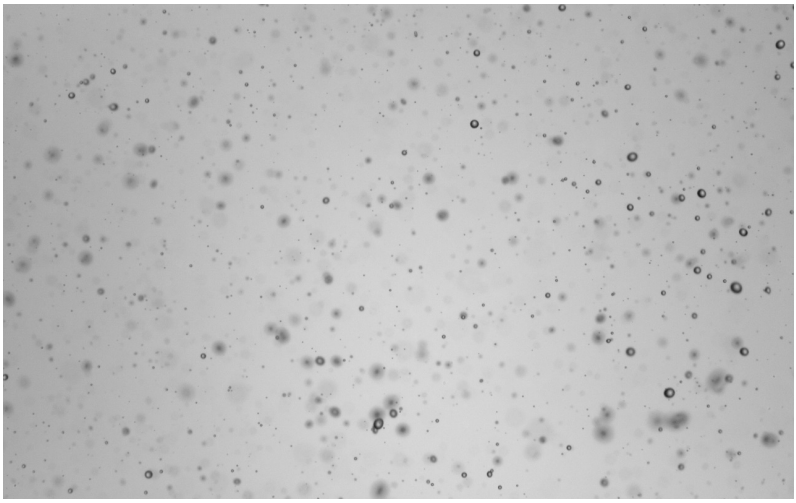

(a) Water

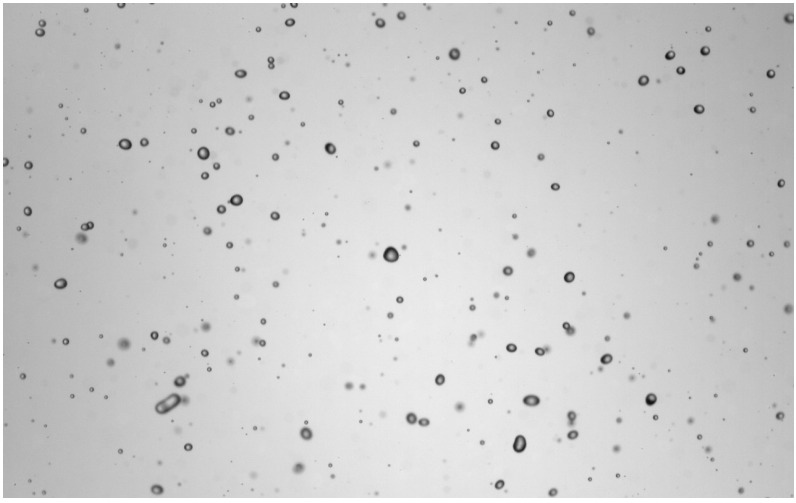

(b) Polyethersiloxane emulsion

Figure 6.19: Typical examples of the raw images obtained for nozzle #5 using an injection pressure of $p = 1$ bar.

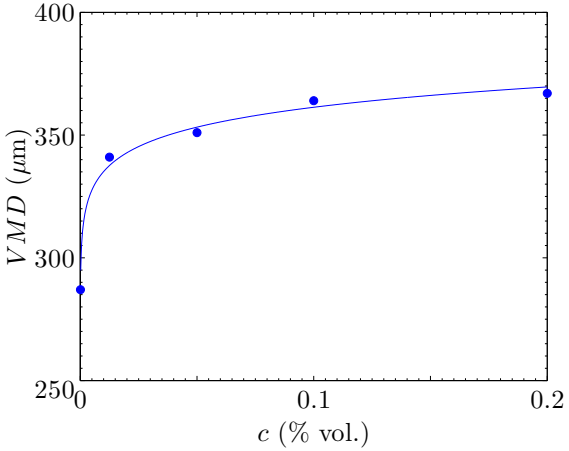

Figure 6.20: Effect of polyethersiloxane concentration on volume mean diameters. Nozzle #5, $p = 1$ bar.

6.21(c-d). The mean diameter $\overline{D}_l$ of such a ligament can be estimated from

$$\overline{D}_l = \left(\frac{4}{\pi\, l} \iint_S h \,\mathrm{d}S \right)^{1/2}, \tag{6.10}$$

where l is the length of the ligament, h is the film thickness and S is the initial surface area of the detached part of the lamella. It becomes evident from equation (6.10) that the mean ligament diameter increases for larger initial surface areas of the detached region. The formed ligament is then subject to capillary instabilities and breaks up into a certain number of single drops with a mean diameter proportional to the diameter of the ligament, Figure 6.22(f). A commonly employed correlation for the drop size distribution originating from such a ligament breakup is given as [90]:

$$\mathfrak{p}(x = D/\overline{D}) = \frac{n^n}{\Gamma(n)} x^{n-1}\, e^{-nx}, \tag{6.11}$$

where $\overline{D}$ is the mean diameter of the generated drops, n is a constant that determines the width of the distribution and $\Gamma(x)$ is the value of the

Gamma function. The ratio of mean drop size and mean ligament size is $\overline{D}/\overline{D}_l \approx 0.4$ [90].

In the case of polyethersiloxane added to the water, the hole nucleation rate is much higher, as shown in Figure 6.22. This results in a more uniform distribution of hole nuclei and the detachment of large fractions of the liquid film is inhibited. In that way, less liquid is contained in very large drops and a more uniform drop size distribution is produced.

The effect of the polyethersiloxane emulsion is slightly different when the liquid is atomized by a standard flat fan nozzle. The reduction of small drops is more significant and reaches up to 65%, which can again be related to ligaments being produced by liquid films with a larger thickness when compared to pure water. In contrast to the atomization by air-injection nozzles, this effect also leads to a shift of the volume median diameters towards larger drops. However, the regular nucleation of holes again produces more uniform drop size distributions with relative span factors being about 30% smaller than the relative span factors produced by pure water.

6.5.5 Scaled drop size distributions

In the previous sections, the influence of the polyethersiloxane emulsion on the drop size distributions has been studied. Now, a closer look is given to the shape of the volume density distributions. By regarding Figures 6.7-6.18 it becomes obvious that the Rosin-Rammler distribution provides a good fit of the experimental data. For a given liquid and nozzle type, the relative span factors Δ remain almost constant over the complete range of Reynolds numbers and orifice sizes investigated in this study. This indicates that volume density distributions could be self-similar when scaled correctly.

The assumption of self-similarity can indeed be confirmed when the volume median diameter is used as a scaling factor, as shown in Figure 6.23. Volume density distributions of nozzles #1-#3 and various injection pressures are in excellent agreement with each other and a master distribution can clearly be identified.

Although the absolute volume fraction distributions depend on Reynolds numbers and orifice sizes, the existence of such a master distribution implies that the underlying mechanisms of liquid atomization are the same. Together with a correlation for the volume median diameter as a function

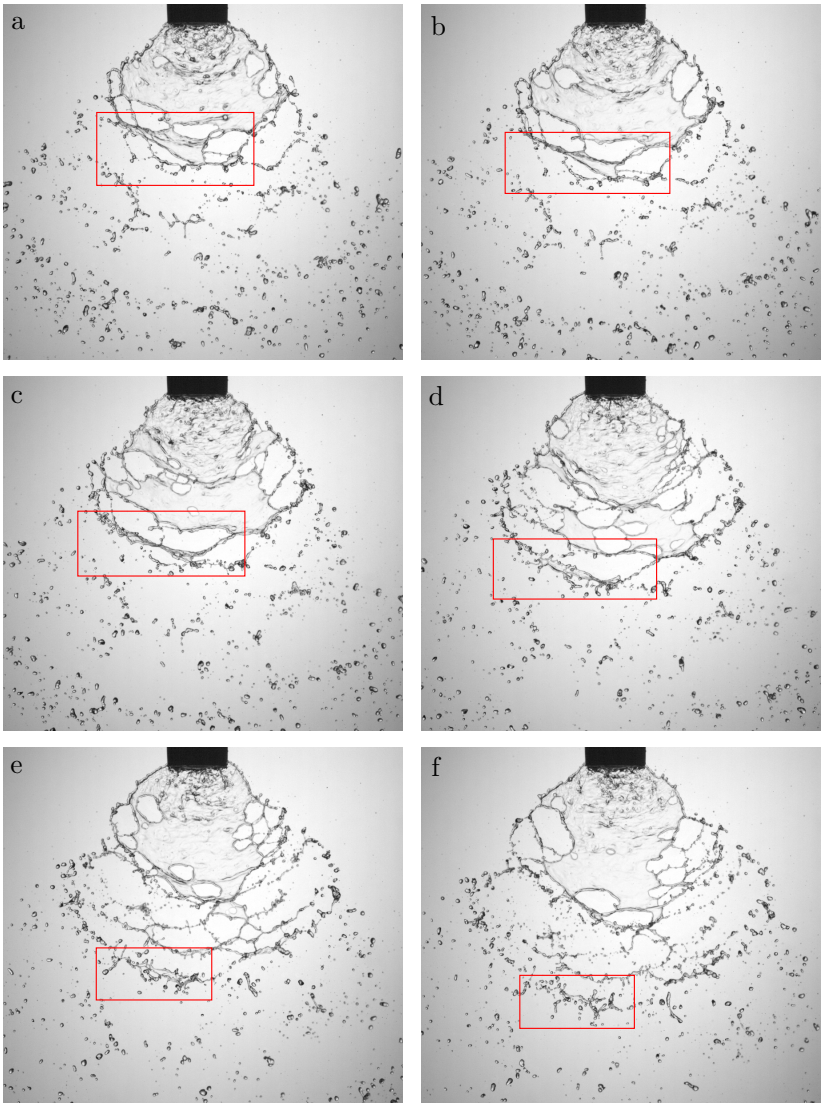

Figure 6.21: Temporal evolution of ligament formation from liquid sheet rupture for water.

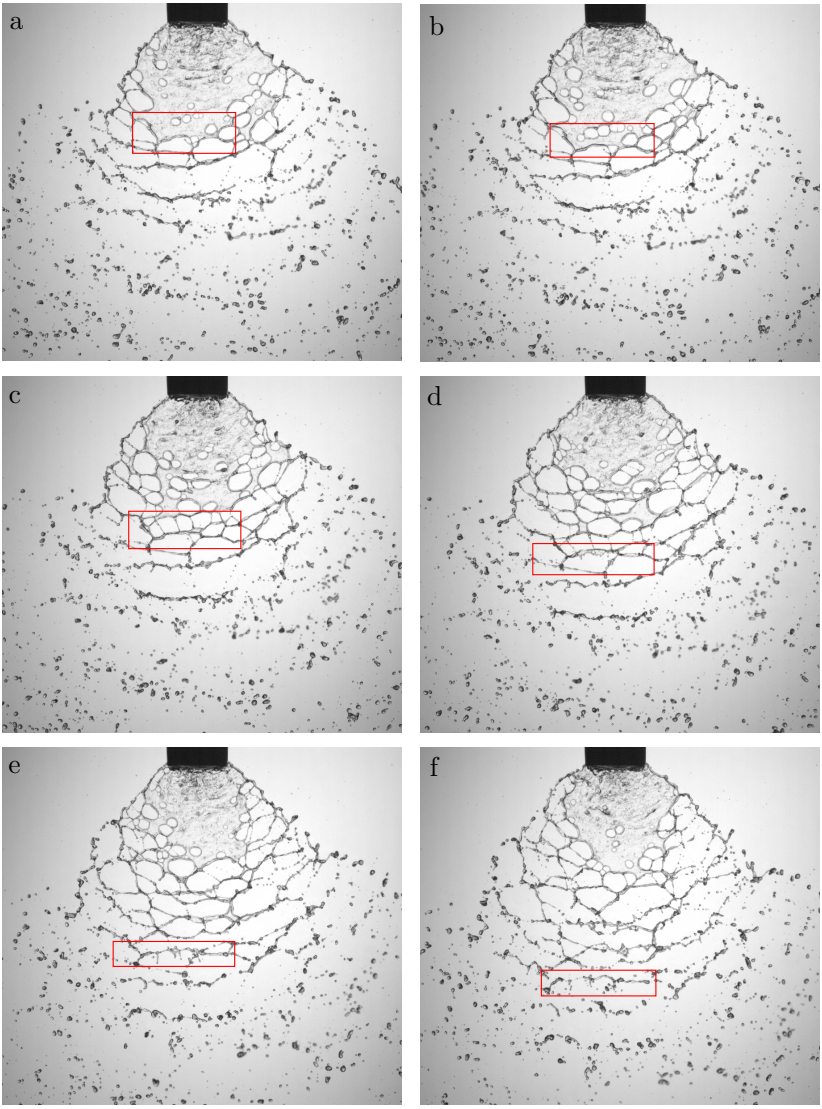

Figure 6.22: Temporal evolution of ligament formation from liquid sheet rupture for PES emulsion.

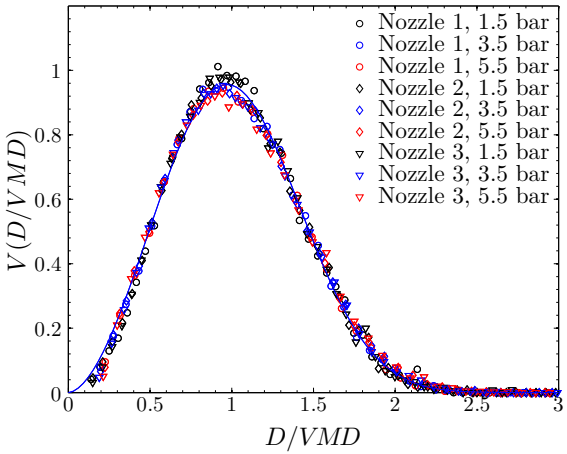

Figure 6.23: Scaled representation of volume density distributions for water, nozzles #1-#3.

of the Reynolds number or injection pressure, such a master distribution allows a very simple and accurate description of drop sizes originating from a series of nozzles. In Figure 6.24 this is exemplarily shown for nozzle #4.

The master distribution is obtained by a regression analysis of the complete data set. Considering nozzle #4, the distribution can be expressed as

$$V\left(x = \frac{D}{VMD}\right) = 2.27\left(\frac{x}{1.15}\right)^{1.61} \exp\left(-\left(\frac{x}{1.15}\right)^{2.61}\right), \tag{6.12}$$

while a good correlation for the volume median diameter is found as

$$VMD = 630\, p^{-0.27}, \tag{6.13}$$

which yields the volume median diameter in µm when the injection pressure p is given in bar. The complete volume density distribution at any injection pressure that is within the operational range of the nozzle can now be obtained by using equation (6.13) to find the volume median diameter, which can then be employed to scale the distribution given in equation (6.12).

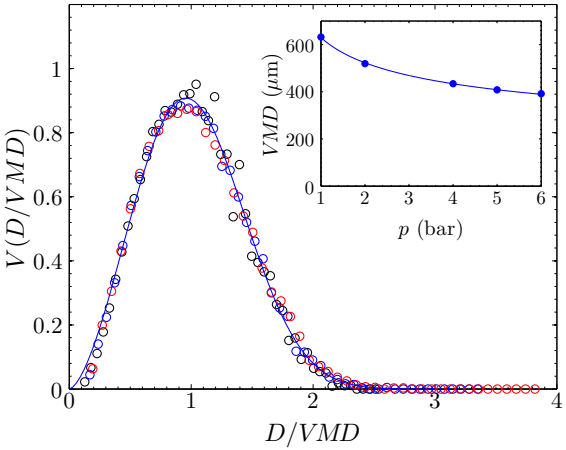

Figure 6.24: Non-dimensional representation of volume density distributions for nozzle #4, water. The small figure depicts the influence of injection pressure on volume median diameters.

6.6 Phase Doppler Measurements

In addition to the image based spray characterization, phase Doppler measurements have been conducted to further investigate the effect of polyethersiloxane. As described in section 2.2, the phase Doppler technique is very sensitive to nonspherical drops. Figure 6.2 clearly demonstrates that a large amount of mass is contained in such deformed drops when air-induction nozzles are used to atomize the liquid. It is obvious that the phase Doppler technique is not suitable for the characterization of such sprays. Additionally, small air bubbles are entrained in the drops produced by air-induction nozzles, which further hinders the light propagation inside the particle. For this reason, phase Doppler measurements are only conducted for the standard flat fan nozzle #5, which produces much smaller drops without air-inclusions.

A *Dantec DualPDA* system has been used for the spray characterization. The system has been adjusted to the settings presented in table 6.1. The detection volume has been placed on the center-line of the nozzle at a distance of 100 mm from the orifice so that the measurement location is

the same as for the image based drop sizing. At each position, 10^5 samples are recorded. The validation rate is 92% and the spherical validation rate is 90%, which indicates a good overall data quality. The data rate is in the order of 1000 samples per second.

Parameter	Setting
Laser Power	150 mW
Wavelength 1	488 nm
Wavelength 2	514 nm
Transmitter focal length	600 mm
Receiver focal length	500 mm
Scattering angle	32°
Aperture mask	Mask C
Probe volume diameter	300 µm
Signal gain	18 dB
Sensitivity	800 V
Maximum particle diameter	640 µm
Phase validation ratio	20%

Table 6.1: Settings used for the phase Doppler measurements.

The volume density distributions of nozzle #5 at $p = 2.5$ bar obtained from the phase Doppler measurements are presented in Figure 6.25. One can observe that the distributions can be resolved almost completely up to diameters of around 400 µm. For larger drops a certain amount of noise can be noticed. This noise originates from large, nonspherical drops which cannot reliably be detected by the phase Doppler system. Although a dual mode phase Doppler system is used, some of the deformed drops are randomly accepted and contribute to the noise. It should be mentioned that the noise in the volume density distribution is generated by only some tens of drops while altogether 10^5 particles have been detected. It is also interesting to note that the amount of noise increases for the PES emulsion,

since a greater number of large drops is produced.

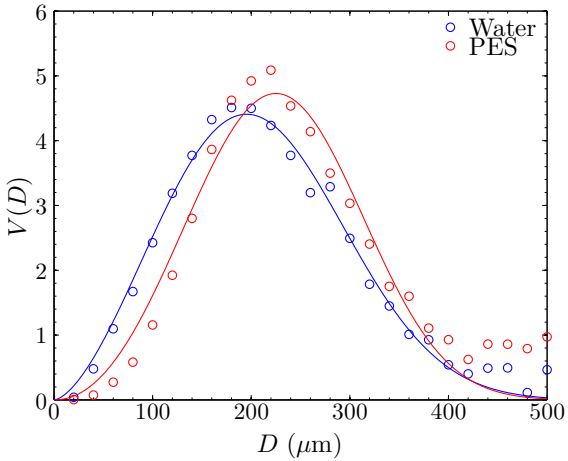

Figure 6.25: Volume density distributions measured by the phase Doppler technique. Nozzle #5, $p = 2.5$ bar.

A qualitative comparison with the results obtained by image based sizing, as depicted in Figure 6.17, shows good agreement between both methods when the effect of PES is considered. Both techniques show that the addition of the additive reduces the amount of small drops and shifts the peak of the distribution towards larger diameters. The reduction of drops smaller than 100 µm is 65% when phase Doppler results are considered and about 60% according to image based results. For large drops, the volume density distributions of pure water and PES emulsion merge. Absolute and quantitative comparison of the results obtained by phase Doppler and image based drop sizing cannot easily be made for two reasons.

First, the techniques do not measure the same quantities. The phase Doppler technique detects drops that move through the probe volume at a certain velocity and flux distributions are thus measured. In contrast to that, the image based drop sizing technique freezes the motion of drops in the field of view so that local volume distributions are obtained. A method for transforming flux density distributions into local volume distributions and vice versa is proposed in [99].

Second, in the case of the phase Doppler results, the noise originating from nonspherical drops indicates that a certain amount of mass that is contained in large drops cannot be reliably detected. Hence, the volume density distributions are biased towards smaller drops so that absolute comparisons are not possible.

Nevertheless, the relative deviation between the volume median diameters obtained from image based drop sizing and the phase Doppler technique is 9%. This indicates that the bias effects described above clearly have to be taken into account, but at the same time it is shown that the absolute deviations between both techniques are within reasonable limits.

The effects of drop deformation on phase Doppler results can be studied in more detail by considering the Weber number, which defines the ratio between deforming aerodynamic forces and restoring capillary forces for each drop. Drops with $\mathrm{We} < 1$ are dominated by surface tension and remain close to a spherical shape. For drops with $\mathrm{We} > 1$ the aerodynamic forces overcome capillary effects and such drops are prone to deformations. Since particle velocities are available from the combined laser and phase Doppler measurements, the Weber number can readily be calculated for each detected drop,

$$\mathrm{We} = \frac{\varrho_g \, D \, (u_l - u_g)^2}{\sigma}. \tag{6.14}$$

The gas velocity u_g is estimated by the mean velocity of the smallest drops with diameters around 10 micrometers. A scatter plot showing the dependance of Weber numbers on drop diameters is depicted in Figure 6.26.

The scatter plot shows that Weber number strongly correlates with drop sizes. Such behaviour is not surprising since the Weber number is proportional to the drop diameter and increases quadratically with the relative velocity between drop and surrounding air. In the case of pressure driven atomization the correlation between relative velocity and drop diameter is also positive, so that such a strong correlation between D and We can be expected.

Weber numbers of drops with $D < 200$ µm are generally below unity which indicates that their shape is very close to spherical. Such drops can reliably be detected by the phase Doppler technique. The Weber number of larger drops increases well above unity and drop deformation by aerodynamic forces should be taken into account. This is demonstrated in Figure 6.27, where various shapes of a single drop being exposed to an airflow at

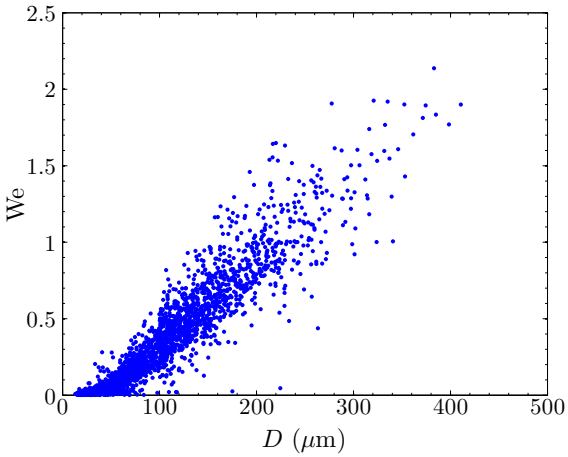

Figure 6.26: Dependence of the Weber number on drop diameters. Data is shown for nozzle #5 and an injection pressure of $p = 2.5$ bar. Only 5% of the detected samples are shown to increase clarity.

We = 2.5 are shown.

It is obvious that the deviations from a spherical shape are rather large. This manifests in aspect ratios ranging up to 1.4. Even in cases with aspect ratios close to unity, strong variations in the local surface curvature can be observed. The reliable detection of such drops by the phase Doppler technique is no longer possible, as discussed in [20]. This behaviour can also explain the discrepancy between results obtained by the phase Doppler technique and image based drop sizing.

The temporal evolution of drop aspect ratios for various Weber numbers is shown in Figure 6.28. Drops are exposed to the airflow at $t = 0$. It can be observed that maximum aspect ratios increase with Weber numbers, which decreases the detectability of drops by the phase Doppler technique.

While frequency distributions and mean diameters as D_{10} are barely affected by a small number of large drops not being detected reliably, volume density distributions and diameters such as the volume mean diameter D_{30} and the volume median diameter *VMD* can significantly be biased towards

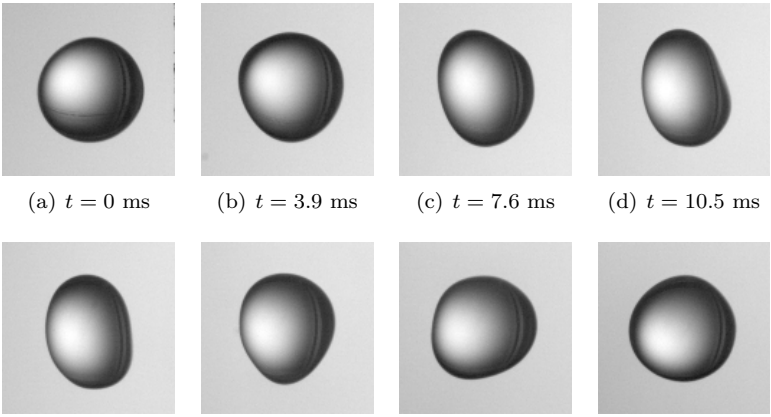

(a) $t = 0$ ms (b) $t = 3.9$ ms (c) $t = 7.6$ ms (d) $t = 10.5$ ms

(e) $t = 12.3$ ms (f) $t = 15.5$ ms (g) $t = 19.4$ ms (h) $t = 23.1$ ms

Figure 6.27: Observed shapes of a single water drop being exposed to an airflow at We = 2.5. The drop enters the flow field at $t = 0$, its initial diameter is $d = 3.1$ mm, the air velocity is $U = 7$ m/s.

smaller drop diameters. Additionally, some of these nonspherical drops can be randomly accepted by a dual mode phase Doppler system and add a certain level of noise to the volume density distributions (see Figure 6.25).

6.7 Summary

In this chapter the effects of polyethersiloxane emulsion on the characteristics of sprays, generated by agricultural fan spray nozzles, have been quantified using an image based sizing technique. It has been shown that the addition of PES results in drop size distributions with smaller relative span factors Δ. This leads to a reduction of the smallest as well as the largest drops in the distribution. The resistance to drift and the coverage characteristics of the sprays are thereby improved.

The results have then been compared to data obtained using the phase Doppler technique and good qualitative agreement has been demonstrated. However, the largest drops in the distribution exhibit noticeable deviations from spherical shapes and cannot be detected reliably by the phase Doppler

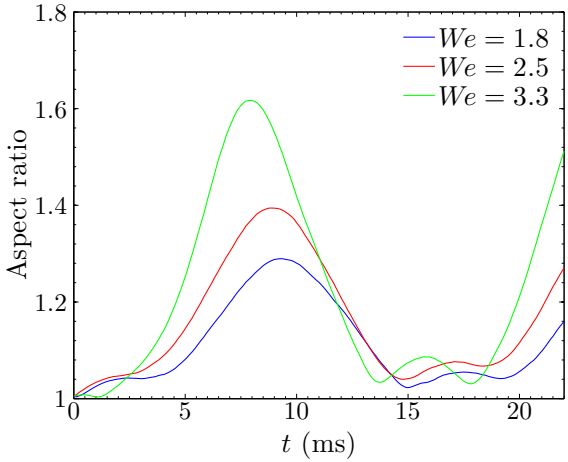

Figure 6.28: Evolution of aspect ratios for various Weber nubers.

instrument. While this effect affects only a minor number of drops, it causes a considerable noise level at the right side of the volume density distributions. On the other hand, the phase Doppler technique is able to resolve number density distributions for drops smaller than about 100 µm, where the image based algorithm fails to provide reliable results.

7 Conclusions & Outlook

Misdirected herbicides and pesticides cause severe damage to surrounding ecosystems. The development and widespread use of highly effective and nonselective crop protection agents, such as glyphosate, has aggravated this problem. Serious efforts are therefore taken to mitigate the generation of small, drift-prone drops in agricultural sprays. At the same time, larger drops result in a more incomplete coverage on the plant surface. The latter effect can considerably limit the efficiency of crop protection agents. Hence, agricultural sprays should be as monodisperse as possible.

The present thesis is focused on controlling mean diameters and polydispersity of agricultural sprays by means of adjuvants. It aims towards sprays with given mean diameters and narrow distributions, so that the amount of liquid in small, drift-prone drops, as well as in large drops with poor coverage characteristics, is minimized. First, the question has been addressed whether aerodynamic fragmentation at low Weber numbers can be used as a model system to evaluate the effects of adjuvants on agricultural sprays. Second, the influence of a selected adjuvant on the breakup morphology and the characteristics of various agricultural sprays has been investigated.

Detailed measurements of drop deformation and bag evolution during the drop-air collision process are presented. The similarity of the phenomena of aerodynamic drop deformation in the bag breakup regime with the corresponding phenomena of drop wall impact and of drops binary collision is shown. During the initial stage of drop deformation, the phenomena scales well using the velocity (3.2). Moreover, a novel kinematic model that describes the thickness evolution of a free axisymmetric liquid sheet is developed. The model predictions are then compared with accurate film thickness measurements employing the Taylor rim velocity and good agreement between both methods is demonstrated.

The aerodynamic fragmentation of liquid in the bag breakup regime is then used to evaluate the ability of various adjuvants to promote hole nucleation in liquid sheets. It is found that polyethersiloxane emulsion is very

effective in inducing liquid film rupture. Compared to water, the maximum extent of the liquid sheet forming the bag is heavily reduced for PES drops. It is further demonstrated that the developed model for the evolution of the film thickness during bag breakup processes can also be applied in the case of emulsions. The number of holes increases with the emulsion concentration, whereas the maximum bag length decreases for larger volume fractions of polyethersiloxane. The promoted film breakup due to emulsion particles leads to considerably larger typical fragment diameters originating from liquid sheet breakup.

It is found that the phenomenon of bag breakup can be used as a single drop model system for the investigation of liquid sheet breakup. Film thicknesses at the instant of rupture and saturation concentrations for bag breakup and liquid sheets produced by agricultural nozzles are in good agreement with each other.

The effect of polyethersiloxane on the breakup morphology of liquid sheets being produced by commercially available agricultural fan spray nozzles is then considered. The selected nozzles include air-induction and standard fan spray nozzles. High-speed visualizations of the lamella fragmentation process are recorded for a qualitative evaluation of liquid fragmentation processes. It is found that the hole nucleation mechanism which has been observed in the case of aerodynamic fragmentation also becomes apparent during the evolution of fan sprays. The additives influence the breakup of a single drop and the atomization in agricultural sprays in the same manner.

A distinct modification of the breakup morphology is achieved by the addition of polyethersiloxane for standard fan-spray and air-induction nozzles. In both cases, the extent of the liquid film is decreased by the emulsion and the position at which the lamella begins to fragment is shifted towards the orifice. An image processing algorithm has been developed, that is able to isolate the liquid film from the background. Two-dimensional probability distributions for a point to be occupied by part of the intact lamella are obtained and presented, mean breakup lengths are extracted from the probability distributions. It is shown that mean breakup lengths are reduced by up to 25% for air injection nozzles and up to 40% for standard fan spray nozzles.

It is further demonstrated that the temporal distribution of breakup lengths follows a lognormal distribution. The measured probability distributions can be precisely described by complimentary error functions. Using

this information, the lamella breakup is characterized by a mean breakup length R_b and a typical fluctuation length scale R'. In the case of PES emulsions, typical fluctuation length scales R' are reduced by 22% - 37% when compared to water.

An image based algorithm for drop size characterization is developed and applied to the sprays considered in this study. The results obtained using this algorithm reveal that volume median diameters are almost unaffected by polyethersiloxane emulsions when dispersed by air-induction nozzles. At the same, the relative width of drop size distributions is reduced by 10 - 15% when PES is added, which confirms the assumption that smaller characteristic fluctuation lengths R' lead to more homogeneous sprays. This leads to a reduction of drift prone volume of up to 35%. For standard fan spray nozzles, the effect induced by the emulsion is more severe. In this case, volume median diameters are shifted towards larger diameters and the relative span is reduced by about 25%. The drift prone fraction of the spray is decreased by up to 65%. For larger injection pressures, this reduction decreases. Furthermore, the volume median diameter can be used to normalize volume density distributions and master distributions are obtained for sprays consisting of the same liquid and being dispersed by the same series of nozzles.

Finally, the applicability of the phase Doppler technique to agricultural sprays is analyzed. Volume median diameters obtained by image processing and the phase Doppler instrument show reasonable agreement. The largest drops of such sprays exhibit Weber numbers of well above unity and surface tension is no longer able to retain a spherical shape. For such drops, diameter measurements obtained by the phase Doppler technique are thus error-prone. While arithmetic mean diameters and number distributions are only weakly influenced by such effects, volume median diameters and volume density distributions can be considerably biased.

In conclusion, it is demonstrated that the addition of polyethersiloxane emulsion substantially improves the quality of all sprays considered in this investigation. In almost all cases, it reduces the amount of small, drift-prone drops as well as the liquid fraction of large drops, so that the liquid coverage on plants is also improved.

The present study has raised a number of open questions. In the author's opinion, the following issues deserve to be the subject of further research.

The emulsion drop spreading mechanism described in section 4.2 provides an intuitive explanation for liquid film rupture, which is widely ac-

cepted in the context of foam destabilization. Nevertheless, a clear verification of that model cannot yet be found in the literature. While small lengthscales (µm - nm) and timescales (µs), as well as the three phases involved, hinder the experimental and numerical investigation of such processes, serious efforts should be made to elucidate the phenomena.

It has been demonstrated that the employed polyethersiloxane emulsion is very effective in inducing liquid film rupture. In the present investigation, the effect of emulsion drop size on the ability to puncture liquid films is not considered. It can be speculated that larger emulsion drops might be able to rupture thicker films than smaller drops. It would be important to understand the correlation between emulsion drop size and critical film thickness, above which the emulsion has no effect. Having such information, the emulsion formulation can further be optimized.

In agricultural applications, spreading additives are used to improve the coverage characteristics of crop protection agents. Preliminary results have shown that some spreading and wetting additives substantially reduce the effect of the anti-drift agents whereas no influence could be found for other spreading additives. For efficient drop size control and optimized coverage of pesticide on the plant, the interaction of spreading agents and anti-drift agents should be better understood.

Bibliography

[1] C. E. Brennen. *Fundamentals of Multiphase Flows*. Cambridge University Press, Cambridge, 2005.

[2] R. Clift, J. R. Grace, and M. E. Weber. *Bubbles, Drops, and Particles*. Academic Press, New York, 1978.

[3] P. C. H. Miller and M. C. Butler Ellis. Effects of formulation on spray nozzle performance for applications from ground-based boom sprayers. *Crop Protection*, 19(8-10):609–615, 2000.

[4] D. Nuyttens, K. Baetens, M. De Schampheleire, and B. Sonck. Effect of nozzle type, size and pressure on spray droplet characteristics. *Biosystems Engineering*, 97(3):333–345, 2007.

[5] E. Hilz, A. W. P. Vermeer, F. A. M. Leermakers, and M. A. C. Stuart. Spray drift: how emulsions influence the performance of agricultural sprays produced through a conventional flat fan nozzle. *Aspects of Applied Biology*, (114):71–78, 2011.

[6] ASTM Standard E2798-11. *Standard Test Method for Characterization of Performance of Pesticide Spray Drift Reduction Adjuvants*. ASTM International, West Conshohocken, PA, 2011.

[7] H. E. Ozkan, A. Miralles, C. Sinfort, H. Zhu, and R. D. Fox. Shields to reduce spray drift. *Journal of Agricultural Engineering Research*, 67(4):311–322, 1997.

[8] S. Edward Law. Agricultural electrostatic spray application: a review of significant research and development during the 20th century. *Journal of Electrostatics*, 51:25–42, 2001.

[9] J Cornillault. Particle size analyzer. *Applied Optics*, 11(2):265–268, 1972.

[10] R. A. Dobbins, L. Crocco, and I. Glassman. Measurement of mean particle sizes of sprays from diffractively scattered light. *AIAA Journal*, 1(8):1882–1886, 1963.

[11] L. G. Dodge, D. J. Rhodes, and R. D. Reitz. Drop-size measurement techniques for sprays: comparison of Malvern laser-diffraction and Aerometrics phase/Doppler. *Applied Optics*, 26(11):2144–54, 1987.

[12] F. Pedrotti, L. Pedrotti, W. Bausch, and H. Schmidt. *Optik für Ingenieure*. Springer-Verlag Berlin Heidelberg, 4th edition, 2008.

[13] Eugene Hecht. *Optics*. Addison Wesley, San Francisco, USA, 4th edition, 2002.

[14] B. Jähne. *Digitale Bildverarbeitung und Bildgewinnung*. Springer Vieweg, Berlin Heidelberg, 7th edition, 2012.

[15] K. J. Hay, Z.-C. Liu, and T. J. Hanratty. A backlighted imaging technique for particle size measurements in two-phase flows. *Experiments in Fluids*, 25(3):226–232, 1998.

[16] G. Castanet, P. Dunand, O. Caballina, and F. Lemoine. High-speed shadow imagery to characterize the size and velocity of the secondary droplets produced by drop impacts onto a heated surface. *Experiments in Fluids*, 54(3):1489, 2013.

[17] H.-E. Albrecht, M. Borys, N. Damaschke, and C. Tropea. *Laser Doppler and Phase Doppler Measurement Techniqes*. Springer, Berlin Heidelberg New York, 1st edition, 2003.

[18] C. Tropea. Optical particle characterization in flows. *Annual Review of Fluid Mechanics*, 43:399–426, 2011.

[19] H. C. van de Hulst. *Light Scattering by Small Particles*. Dover Publications, Inc., New York, 1st edition, 1981.

[20] N. Damaschke, G. Gouesbet, G. Gréhan, H. Mignon, and C. Tropea. Response of phase Doppler anemometer systems to nonspherical droplets. *Applied Optics*, 37(10):1752–61, 1998.

[21] J. O. Hinze. Fundamentals of the hydrodynamic mechanism of splitting in dispersion processes. *AIChE Journal*, 1(3):289–295, 1955.

[22] W. R. Lane. Shatter of drops in streams of air. *Industrial & Engineering Chemistry*, 43(6):1312–1317, 1951.

[23] L. P. Hsiang and G. M. Faeth. Near-limit drop deformation and secondary breakup. *International Journal of Multiphase Flow*, 18(5):635–652, 1992.

[24] M. Pilch and C. A. Erdman. Use of breakup time data and velocity history data to predict the maximum size of stable fragments for acceleration-induced breakup of a liquid drop. *International Journal of Multiphase Flow*, 13(6):741–757, 1987.

[25] D. R. Guildenbecher, C. López-Rivera, and P. E. Sojka. Secondary atomization. *Experiments in Fluids*, 46(3):371–402, 2009.

[26] T. G. Theofanous. Aerobreakup of newtonian and viscoelastic liquids. *Annual Review of Fluid Mechanics*, 43(1):661–690, 2011.

[27] P. Sojka and D. R. Guildenbecher. Experimental investigation of aerodynamic fragmentation of liquid drops modified by electrostatic surface charge. *Atomization and Sprays*, 21(2):139–147, 2011.

[28] Z. Liu and R. D. Reitz. An analysis of the distortion and breakup mechanisms of high speed liquid drops. *International Journal of Multiphase Flow*, 23(4):631–650, 1997.

[29] D. D. Joseph, J. Belanger, and G. S. Beavers. Breakup of a liquid drop suddenly exposed to a high-speed airstream. *International Journal of Multiphase Flow*, 25(6-7):1263–1303, 1999.

[30] A. R. Hanson, E. G. Domich, and H. S. Adams. Shock tube investigation of the breakup of drops by air blasts. *Physics of Fluids*, 6(8):1070, 1963.

[31] L.-P. Hsiang and G. M. Faeth. Drop deformation and breakup due to shock wave and steady disturbances. *International Journal of Multiphase Flow*, 21(4):545–560, 1995.

[32] H. Zhao, H.-F. Liu, W.-F. Li, and J.-L. Xu. Morphological classification of low viscosity drop bag breakup in a continuous air jet stream. *Physics of Fluids*, 22(11):114103, 2010.

[33] T. G. Theofanous and G. J. Li. On the physics of aerobreakup. *Physics of Fluids*, 20(5):052103, 2008.

[34] A. K. Flock, D. R. Guildenbecher, J. Chen, P. E. Sojka, and H.-J. Bauer. Experimental statistics of droplet trajectory and air flow during aerodynamic fragmentation of liquid drops. *International Journal of Multiphase Flow*, 47:37–49, 2012.

[35] N. Rimbert, and G. Castanet. Crossover between Rayleigh-Taylor instability and turbulent cascading atomization mechanism in the bag-breakup regime. *Physical Review E*, 84(1):1–10, 2011.

[36] E. Villermaux and B. Bossa. Single-drop fragmentation determines size distribution of raindrops. *Nature Physics*, 5(9):697–702, 2009.

[37] C.-L. Ng, R. Sankarakrishnan, and K. A. Sallam. Bag breakup of non-turbulent liquid jets in crossflow. *International Journal of Multiphase Flow*, 34(3):241–259, 2008.

[38] S. T. Thoroddsen, M.-J. Thoraval, K. Takehara, and T. G. Etoh. Micro-bubble morphologies following drop impacts onto a pool surface. *Journal of Fluid Mechanics*, 708:469–479, 2012.

[39] S. A. Krzeczkowski. Measurement of liquid droplet disintegration mechanisms. *International Journal of Multiphase Flow*, 6(3):227–239, 1980.

[40] M. Jalaal and K Mehravaran. Fragmentation of falling liquid droplets in bag breakup mode. *International Journal of Multiphase Flow*, 47:115–132, 2012.

[41] I. V. Roisman. Inertia dominated drop collisions. II. An analytical solution of the Navier-Stokes equations for a spreading viscous film. *Physics of Fluids*, 21(5):052104, 2009.

[42] J. Eggers, M. A. Fontelos, C. Josserand, and S. Zaleski. Drop dynamics after impact on a solid wall: Theory and simulations. *Physics of Fluids*, 22(6):062101, 2010.

[43] M. Marengo, C. Antonini, I. V. Roisman, and C. Tropea. Drop collisions with simple and complex surfaces. *Current Opinion in Colloid & Interface Science*, 16:292–302, 2011.

[44] A. Bisighini, G. E. Cossali, C. Tropea, and I. V. Roisman. Crater evolution after the impact of a drop onto a semi-infinite liquid target. *Physical Review E*, 82(3):036319, 2010.

[45] I. V. Roisman, E. Berberovic, and C. Tropea. Inertia dominated drop collisions. I. On the universal flow in the lamella. *Physics of Fluids*, 21(5):052103, 2009.

[46] C. Focke and D. Bothe. Direct numerical simulation of binary off-center collisions of shear thinning droplets at high weber numbers. *Physics of Fluids*, 24(7):073105, 2012.

[47] A. L. Yarin and D. A. Weiss. Impact of drops on solid surfaces: self-similar capillary waves, and splashing as a new type of kinematic discontinuity. *Journal of Fluid Mechanics*, 283:141–173, 1995.

[48] G. Taylor. The dynamics of thin sheets of fluid. II. Waves on fluid sheets. *Proceedings of the Royal Society A: Mathematical, Physical and Engineering Sciences*, 253(1274):296–312, 1959.

[49] T. G. Theofanous, V. V. Mitkin, C. L. Ng, C-H. Chang, X. Deng, and S. Sushchikh. The physics of aerobreakup. II. Viscous liquids. *Physics of Fluids*, 24(2):022104, 2012.

[50] T. G. Theofanous, V. V. Mitkin, and C. L. Ng. The physics of aerobreakup. III. Viscoelastic liquids. *Physics of Fluids*, 25(3):032101, 2013.

[51] H. Zhao, H.-F. Liu, J.-L. Xu, and W.-F. Li. Secondary breakup of coal water slurry drops. *Physics of Fluids*, 23(11):113101, 2011.

[52] R. Pugh. Foaming, foam films, antifoaming and defoaming. *Advances in Colloid and Interface Science*, 64(95):67–142, 1996.

[53] P.-G. de Gennes, F. Brochard-Wyart, and D. Quere. *Capillarity and Wetting Phenomena*. Springer Science+Business Media, Inc., 1st edition, 2004.

[54] J. Venzmer. Alltägliche Phänomene. Grenzflächenchemische Spezialitäten. *Chemie in unserer Zeit*, 42(2):72–79, 2008.

[55] N. D. Denkov. Mechanisms of foam destruction by oil-based antifoams. *Langmuir*, 20(22):9463–9505, 2004.

[56] F. Savart. Mémoire sur la constitution des veines liquides lancees par des orifices circulaires en mince paroi. *Annales de Chemie et Physique*, 53:337–86, 1833.

[57] F. Savart. Mémoire sur le choc d'une veine liquide lancée contre un plan circulaire. *Annales de Chemie et Physique*, 54:56-87, 1833.

[58] F. Savart. Suite du Memoire sur le choc d'une veine liquide lancée contre un plan circulaire. *Annales de Chemie et Physique*, 54:113–45, 1833.

[59] F. Savart. Mémoire sur le choc de deux veines liquides animées de mouvements directement opposes. *Annales de Chemie et Physique*, 55:257–310, 1833.

[60] C. Clanet. Waterbells and Liquid Sheets. *Annual Review of Fluid Mechanics*, 39:469–496, 2007.

[61] E. Villermaux. Fragmentation. *Annual Review of Fluid Mechanics*, 39:419–446, 2007.

[62] A. H. Lefebvre. Airblast atomization. *Progress in Energy and Combustion Science*, 6(3):233–261, 1980.

[63] J. H. Combellack, N. M. Westen, and R. G. Richardson. A comparison of the drift potential of a novel twin fluid nozzle with conventional low volume flat fan nozzles when using a range of adjuvants. *Crop Protection*, 15(2):147–152, 1996.

[64] P. Kryger Jensen, L. N. Jorgensen, and E. Kirknel. Biological efficacy of herbicides and fungicides applied with low-drift and twin-fluid nozzles. *Crop Protection*, 20(1):57–64, 2001.

[65] G. Taylor and L. Howarth. The dynamics of thin sheets of fluid. I. Water bells. *Proceedings of the Royal Society A: Mathematical, Physical and Engineering Sciences*, 253(1274):289–295, 1959.

[66] N. Dombrowski and R. P. Fraser. A photographic investigation into the disintegration of liquid sheets. *Philosophical Transactions of the Royal Society A: Mathematical, Physical and Engineering Sciences*, 247(924):101–130, 1954.

[67] L. Rayleigh. On the capillary phenomena of jets. *Proceedings of the Royal Society of London*, 29(196-199):71–97, 1879.

[68] C. Weber. Zum Zerfall eines Flüssigkeitsstrahles. *ZAMM - Zeitschrift für Angewandte Mathematik und Mechanik*, 11(2):136–154, 1931.

[69] N. Dombrowski, D. Hasson, and D. E. Ward. Some aspects of liquid flow through fan spray nozzles. *Chemical Engineering Science*, 12(1):35–50, 1960.

[70] N. Bremond, C. Clanet, and E. Villermaux. Atomization of undulating liquid sheets. *Journal of Fluid Mechanics*, 585:421, 2007.

[71] Y. J. Choo and B. S. Kang. The effect of jet velocity profile on the characteristics of thickness and velocity of the liquid sheet formed by two impinging jets. *Physics of Fluids*, 19(11):112101, 2007.

[72] H. B. Squire. Investigation of the instability of a moving liquid film. *British Journal of Applied Physics*, 4(6):167–169, 1953.

[73] C. J. Clark and N. Dombrowski. Aerodynamic instability and disintegration of inviscid liquid sheets. *Proceedings of the Royal Society A: Mathematical, Physical and Engineering Sciences*, 329(1579):467–478, 1972.

[74] G. Taylor. The dynamics of thin sheets of fluid. III. Disintegration of fluid sheets. *Proceedings of the Royal Society A: Mathematical, Physical and Engineering Sciences*, 253(1274):313–321, 1959.

[75] F. E. C. Culick. Comments on a ruptured soap film. *Journal of Applied Physics*, 31(6):1128–1129, 1960.

[76] J. W. M. Bush and A. E. Hasha. On the collision of laminar jets: fluid chains and fishbones. *Journal of Fluid Mechanics*, 511:285–310, 2004.

[77] R. Li and N. Ashgriz. Characteristics of liquid sheets formed by two impinging jets. *Physics of Fluids*, 18(8):087104, 2006.

[78] R. P. Fraser, P. Eisenklam, N. Dombrowski, and D. Hasson. Drop formation from rapidly moving liquid sheets. *AIChE Journal*, 8(5):672–680, 1962.

[79] S. D. Sovani, P. E. Sojka, and A. H. Lefebvre. Effervescent atomization. *Progress in Energy and Combustion Science*, 27(4):483–521, 2001.

[80] H. Lhuissier and E. Villermaux. Effervescent atomization in two dimensions. *Journal of Fluid Mechanics*, 714:361–392, 2013.

[81] G. Reiter. Dewetting of thin polymer films. *Physical Review Letters*, 68(1):75–78, 1992.

[82] M. C. Butler Ellis and C. R. Tuck. How adjuvants influence spray formation with different hydraulic nozzles. *Crop Protection*, 18(2):101–109, 1999.

[83] M. C. Butler Ellis, C. R. Tuck, and P. C. H. Miller. Dilute emulsions and their effect on the breakup of the liquid sheet produced by flat-fan spray nozzles. *Atomization and Sprays*, 9(4):385–397, 1999.

[84] J. H. Spurk and N. Aksel. *Strömungslehre*. Springer, Berlin Heidelberg, 6th edition, 2006.

[85] G. M. Hale and M. R. Querry. Optical constants of water in the 200-nm to 200-microm wavelength region. *Applied Optics*, 12(3):555–63, 1973.

[86] R. C. Gonzales, R. E. Woods, and S. L. Eddins. *Digital Image Processing using Matlab*. Pearson Prentice Hall, Upper Saddle River, 1st edition, 2004.

[87] R. G. Dorman. The atomization of liquid in a flat spray. *British Journal of Applied Physics*, 3(6):189–192, 1952.

[88] A. H. Lefebvre and X. F. Wang. Mean drop sizes from pressure-swirl nozzles. *Journal of Propulsion and Power*, 3(1):11–18, 1987.

[89] V. Dorfner, J. Domnick, F. Durst, and R. Kohler. Viscosity and surface tension effects in pressure swirl atomization. *Atomization and Sprays*, 5(3):261–285, 1995.

[90] E. Villermaux, P. Marmottant, and J. Duplat. Ligament-Mediated Spray Formation. *Physical Review Letters*, 92(7):1–4, 2004.

[91] A. Tratnig and G. Brenn. Drop size spectra in sprays from pressure-swirl atomizers. *International Journal of Multiphase Flow*, 36(5):349–363, 2010.

[92] A. Khoshnevis, S. S. H. Tsai, and E. Esmaeilzadeh. Electric field induced sheeting and breakup of dielectric liquid jets. *Physics of Fluids*, 26(1):012103, 2014.

[93] G. Brenn, Z. Prebeg, D. Rensink, and A. L. Yarin. Control of spray formation by vibrational excitation of flat-fan and conical liquid sheets. *Atomization and Sprays*, 15(6):661–685, 2005.

[94] M. C. Butler Ellis, C. R. Tuck, and P. C. H. Miller. The effect of some adjuvants on sprays produced by agricultural flat fan nozzles. *Crop Protection*, 16(1):41–50, 1997.

[95] A. H. Lefebvre. *Atomization and Sprays*. CRC Press, Taylor & Francis Group, Boca Raton, 1st edition, 1989.

[96] P. Rosin and E. Rammler. Die Kornzusammensetzung des Mahlgutes im Lichte der Wahrscheinlichkeitslehre. *Kolloid-Zeitschrift*, 67(1):16–26, 1934.

[97] R. A. Mugele and H. D. Evans. Droplet size distribution in sprays. *Industrial & Engineering Chemistry*, 43(6):1317–1324, 1951.

[98] W. K. Brown and K. H. Wohletz. Derivation of the Weibull distribution based on physical principles and its connection to the Rosin-Rammler and lognormal distributions. *Journal of Applied Physics*, 78(4):2758, 1995.

[99] I. V. Roisman and C. Tropea. Flux measurements in sprays using phase Doppler techniques. *Atomization and Sprays*, 11:673–705, 2001.

Nomenclature

Latin letters

Symbol	SI unit	Description
A	m^2	Area
C	-	Constant
D	m	Diameter
DOF	m	Depth of field
E	kg/s^2	Entering coefficient
F_Φ	m/deg	Phase conversion factor
H	m	Bag apex position
I	-	Intensity
J_1	-	Bessel function of the first kind
K	-	Number of pixels
L	m	Drop length
M	-	Magnification
M	-	Number of size classes
N	-	Number
N	-	f-Number
P	-	Histogram count
Q	1/m	Density function
R	m	Drop radius
R	m	Length of the intact liquid sheet
R_b	m	Mean breakup length
R'	m	Characteristic fluctuation length
S	kg/s^2	Spreading coefficient
T	-	Transmissivity
U	m/s	Characteristic velocity
V	m/s	Characteristic velocity
$V(D)$	1/m	Volume density distribution
$\overline{V}(D)$	1/m	Mean volume density distribution

Symbol	SI unit	Description
$\dot{V}$	m^3/s	Volume flux
VMD	m	Volume median diameter
X	m	Radial position of material point
Z	m	Axial position of material point
a	-	Model constant
b	-	Model constant
c	-	Model constant
c	-	Concentration (vol.)
c	-	Contour level
d	m	Distance
e	-	Entropy
$\vec{e}$	-	Unit vector
f	1/s	Frequency
f	m	Focal length
g	m/s^2	Gravitational acceleration
h	m	Liquid film thickness
$\vec{k}$	m/s^2	Body force
k	1/m	Wave number
k_p	-	Calibration factor
l	m	Length
m	-	Refractive index ratio
n	-	Refractive index
n	-	Model constant
p	$kg/(m\,s^2)$	Pressure
r	m	Cylindrical coordinate
s	m	Distance
t	s	Time
t_r^*	s	Drop velocity relaxation time
Δt_e	s	Exposure time
$\bar{t}$	-	Scaled time
u	m/s	Velocity
v	m/s	Velocity
x	m	Cartesian coordinate
y	m	Cartesian coordinate
z	m	Cartesian coordinate
z	m	Cylindrical coordinate

Greek letters

Symbol	SI unit	Description
$\Gamma(x)$	-	Gamma function
Δ	-	Relative span
$\Delta\Phi_{12}$	deg	Phase angle
Φ	-	Probability
Θ	deg	Beam intersection angle
α	1/m	Attenuation coefficient
α	deg	Angle
β	deg	Spray angle
ϵ	m	Diameter of circle of confusion
ζ	-	loss factor
η	-	Model constant
κ	1/m	Curvature
λ	m	Wavelength
μ	kg/(m s)	Dynamic viscosity
μ	-	Parameter
ν	m^2/s	Kinematic viscosity
ξ	m	Initial position
ρ	kg/m^3	Density
σ	-	Parameter
σ	kg/s^2	Surface tension coefficient
τ	-	Model constant
φ	deg	Cylindrical coordinate
ϕ	deg	Scattering angle
ψ	deg	Elevation angle

Fraktur letters

Symbol	SI unit	Description
$\mathfrak{P}$	-	Mean entropy of hole perimeter
$\mathfrak{Q}$	-	Distribution function
$\mathfrak{S}$	-	Solidity
$\mathfrak{V}$	-	Volume fraction
$\mathfrak{p}$	-	Number density

Dimensionless numbers

Symbol	Definition	Description
We	$\rho D U^2/\sigma$	Weber number
Re	UD/ν	Reynolds number
Oh	$\eta/(D\rho\sigma)^{1/2}$	Ohnesorge number